2012

Magnetic compensation in the bimetallic oxalates and the cerium volume collapse

Peter Leo Reis
Louisiana State University and Agricultural and Mechanical College

MAGNETIC COMPENSATION IN THE BIMETALLIC OXALATES AND THE CERIUM VOLUME COLLAPSE

A Dissertation

Submitted to the Graduate Faculty of the
Louisiana State University and
Agricultural and Mechanical College
in partial fulfillment of the
requirements for the degree of
Doctor of Philosophy

in

The Department of Physics and Astronomy

by
Peter Leo Reis
B.S., University of North Dakota, 2005
December 2012

I would like to dedicate this thesis to a number of people. First, I would like to dedicate this thesis to my mother and father. Also to my sister Margaret, with your inspiration and many hours of talking on the phone together, you invited me back to reality. To my grandmother Helen and late grandfather Raymond, I would have never made it without your influence as a youngster. Also to my father for inspiring me mechanically when I was young. You certainly planted the first seeds of physics in my mind. And last I would like to dedicate this thesis to my uncle Bill!

Acknowledgments

First I would like to thank my advisors for their valuable guidance over the course of the last six complete years we have spent together. In particular I would like to thank my primary advisor Dr. Juana Moreno for her invaluable thoughtfulness, understanding and guidance that she provided me during our many discussions we had over the course of the last seven years. And to my co-advisors Dr. Mark Jarrell, Dr. Randy Fishman and Dr. Fakher Assaad for allowing me the opportunity to work and learn a new aspect of physics from you which greatly broadened my understanding of physics as I know it today.

Without the assistance of my immediate collaborators Peng Zang, Dr. Ka Ming Tam, Dr. Juana Moreno and Dr. Mark Jarrell, I believe the extent and content to which we understand the physics of our current project would be nonexistent.

Second I would like to thank all the group members that I worked with over the years for the thoughtful discussion we had in assisting each other in sometimes intractable problems that we were faced with. Without being able to talk to all of you constantly, the progress reported in this thesis would not have been possible.

Additionally I would like to thank all the members of my thesis committee, Dr. Juana Moreno, Dr. Mark Jarrell, Dr. Daniel Sheehy, Dr. Blaise Bourdin, Dr. Stephen Shipman and Dr. Von Braun Nascimento for participating on my committee.

Also I would like to thank Mrs. Carol A Duran for assisting me in proof reading my thesis and most of all I would like to once again thank Dr. Ka Ming Tam for his fruitful suggestions while I wrote my thesis.

And last but not least, I want to thank my family for their support, understanding, and advice they provided to me over the last seven years; for this I am in debt to you!

Table of Contents

Abstract

In this thesis the author reports his collaborative efforts on two distinct areas of research that has been conducted. The first part of the thesis pertains to the author and his collaborators research on a particular class of organic magnets called the bimetallic oxalates. The main theme of this research was to predict magnetic compensation (magnetization reversal) in unsynthesized bimetallic oxalate structures, motivated by experiments which showed that Fe(II)Fe(III) exhibited magnetic compensation. In addition it was known that a large amount of anisotropy was present in the bimetallic oxalate structure which resulted from the intermediate oxalate molecules between the transition metal ions which would drastically change the angular momentum of the transition metals. Consequently, because of the large anisotropy, we predicted that, if neutron diffraction measurements were performed on these materials, a spin-wave gap would exist of the order of 7.8 meV. The contribution to the research that I did on the bimetallic oxalates was calculating numerically the regions of magnetic compensation in chapter 3; where a large part of the theoretical calculation was performed by R.S. Fishman. In chapter 4 I contributed equally to the thoeretical and computational calculation of the spin wave gap in regions of magnetic compensation with the assistance of my advisor R.S. Fishman.

The second half of this thesis is devoted to the author's and his collaborators' research on the cerium volume collapse. Until 2004 the collapse was largely believed to be understood as the result of Kondo screening of the local moment in cerium. However in 2004 it was realized that, in addition to a large Kondo effect driving the cerium volume collapse, the phonon frequency was very different between the large and small volume phases, and consequently the change in phonon frequency was the direct result of large electron-phonon correlations. This upset the apple cart of Kondo correlation being solely responsible for the volume collapse in cerium, and the change in phonon frequency must be accounted for to accurately describe the cerium volume collapse. To this end the author and his collaborators' developed a model which would include both of the correlations (Kondo and phononic) in the volume collapse. To analyze this model we used Dynamical Mean Field Theory in conjunction with Continuous

Time Quantum Monte Carlo. What we found in our simulations was that the small volume Kondo phase was drastically influenced by the presence of the electron-phonon correlations. My contribution to this research relating to the cerium volume collapse consisted of locating the Kondo to local moment transition in the parameter space of the periodic Anderson model with Holstein phonons coupled to the conduction electrons; this work is illustrated in section 5.7 of this thesis. Also I calculated the quasi particle renormalization fraction outlined in sections 6.3 to 6.5 where the results and analysis are displayed in section 7.6. Additionally I calculated the internal energy and high frequency behavior of this model which is outlined in the appendix. This work was done with my collaborators Peng Zang, Dr. Ka Ming Tam, Dr. Juana Moreno, Dr. Mark Jarrall and Dr. Fakher Assaad.

Chapter 1

Introduction

1.1 Condensed Matter Physics

Condensed matter physics is a branch of physics which investigates the properties of materials in their solid or liquid form at the atomic and molecular level. Condensed matter physics is an attempt to explain the electric, magnetic, thermodynamic, and the emergent phenomena which arises as many atoms are assembled to form a macroscopic structure. A successful understanding of condensed matter systems is achieved through experiments on the material and theoretical investigations. Condensed matter covers a wide spectrum of different phenomena and has influenced other branches of science and mathematics such as chemistry, materials science, high-energy physics, cosmology, nanotechnology and computer science. Some of the most active areas of research in condensed matter physics are in strongly correlated materials, semiconductors and Bose-Einstein condensation. In this thesis the author and his colleagues have attempted to further our knowledge of strongly correlated and magnetic materials and increase their interconnection with other areas of condensed matter physics, in an effort to ultimately increase the impact of condensed matter physics on other closely related fields.

1.2 Strongly Correlated Materials

Strongly correlated materials are interesting and challenging materials that exhibit many unusual properties that would not be expected given the materials band-structure and geometry. Many materials which exhibit strongly correlated properties are high-temperature superconductors, heavy fermion compounds, magnetic materials, Mott insulators and low dimensional spin chains. Why are these materials are so different from conventional materials? They are often insulating when band theory calculations demonstrate that they are metallic. Why are these materials insulators at half filling? This is primarily the result of the elec-

trons strong repulsion with adjacent electrons in the lattice which decreases their mobility and serves to localize the electron at the ionic core, which prevents the electrons from conducting, which results in an insulating state. If one were to perform a simple Hartree-Fock or single electron calculation on these materials they would find that these materials should be metallic; however, if one performs a more complicated calculation on these materials which includes the strong Coulomb correlations between electrons then one would discover that the material is in fact an insulator since a Mott band gap opens at the Fermi-level in the density of states. The properties of the materials mentioned at the beginning of this section are the result of strong electron-electron Coulomb interactions in the material, consequently these materials have posed many challenges for experimentalists and theoretical physicists working with these materials, since in most cases there is no general approach to analyzing these materials. Strongly correlated materials are currently at the forefront of research. In the next section we describe three areas of strongly correlated materials in more detail, which are high-temperature superconductors, magnetic materials and heavy fermion compounds.

1.2.1   High-Temperature Superconductivity

The discovery of high-temperature superconductivity (HTC) in 1986 by Karl Müller and Johannes Bednorz was found in the ceramic compound LaBaCuO below the transition temperature of 30K [1]. The discovery of superconductivity in LaBaCuO marked the beginning of a new era of non-conventional superconductivity in which the superconducting state resulted from large electron-electron correlations in the copper-oxide layer of this material. The mechanism driving the superconductivity in LaBaCuO was thought to be very different from the traditional driving mechanism in standard superconductors in which the pairing binding two electrons resulted from lattice vibrations. Soon after the discovery of superconductivity in the compound LaBaCuO it was found a higher transition temperature occured in the ceramic compounds yttrium barium copper oxygen $Yba_2Cu_3O_7$ (YBCO) with $T_c = 90K$ [2], with the highest transition temperature reported in the compound mercury barium calcium copper oxide $HgBa_2Ca2Cu_3O_x$ with $T_c = 133K$ [3].

Changing the electron concentration in the copper oxide planes of the cuprate superconductors resulted in a rich phase diagram which displayed anti-ferromagnetism to metallic and superconducting properties Fig. 1.1. The undoped phase of the parent compound of these materials exhibits long range anti-ferromagnetic Mott ordering for temperatures below the Néel temperature T_N; upon hole doping the anti-ferromagnetism of the parent compound is destroyed and the cuprates transition into two different phases which depends on the the doping density ρ, the pseudogap temperature T^* and the superconducting temperature T_c.

For the temperature $T^* > T > T_c$ the parent compound transitions from Mott insulator characteristics to pseudogap behavior. The pseudogap occurs in these materials mainly due to a small but finite density of states at the Fermi level which reemerges as the parent compound is doped. As a result of the finite density of states at the Fermi level the system is not in a metallic phase because of the large Coulomb correlations between electrons. In fact the physics of the pseudogap phase remains a mystery. A couple of scenarios have been proposed. The first scenario suggests that the electrons in the pseudogap phase form preformed superconducting pairs which are unable to superconduct because of large phase fluctuations of the phase field at temperatures $T > T_c$; this approach has been supported by an attractive pairing model approach. The second scenario of the physics of the pseudogap phase is that the doped cuprate is in a state which has insulating behavior reminiscent of the undoped parent compound.

The superconducting state occurs when $T < T_c$. The physics of the superconducting state has been a major challenge to theorists since the discovery of HTC in 1986. One theory that was put forward to explain HTC was the resonating valence bond (RVB) by Anderson, which describes the ground state of the parent compound as an arrangement of disordered spin states and was an attempt to explain the superconducting state by doping the RVB state [5]. The RVB state was successful in describing the ground state of the parent compound and the superconducting state within a mean-field approximation using a Gutzwiller projection, however it is known that the true ground-state must include quantum fluctuations inherent to the quantum ground-state, which are removed using the Gutzwiller projection. For these reasons it is reasonable to believe that a more thorough understanding of the superconducting phase of the HTC compounds will be achieved with the use of non-perturbative methods such as Quantum Monte Carlo (QMC) and other methods in which mean-field approximations are not employed.

1.2.2 Magnetism

Magnetism in materials is a direct consequence of strong electron-electron correlations. More specifically magnetic phenomena in solid state arises from an exchange interaction J which occurs between electrons due to Coulomb correlations between two electrons and the Pauli principle requirement on the total electronic wave function. Different types of magnetic exchange can occur in materials; in general direct exchange occurs when the electronic wave functions between two electrons directly overlap, and indirect magnetic exchange occurs between two electrons where their electronic wave functions do not overlap, therefore the magnetic exchange is mediated by itinerant conduction electrons as in double-exchange or by
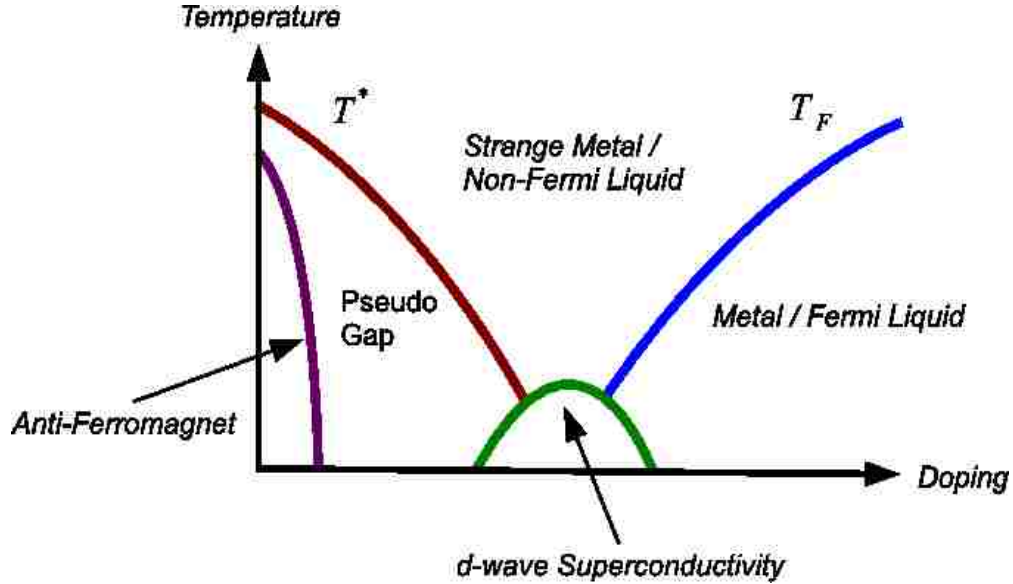
Figure 1.1: Cuprate phase diagram as a function of temperature T vs. hole doping n. For small values of n and $T < T_N$ the parent compound of the cuprates is an anti-ferromagnetic Mott insulator. As the cuprates are doped the pseudogap phase occurs for temperatures in the range $T^\star > T > T_c$ where T_c is the ordering temperature of the superconducting state. When $T < T_c$ the cuprates transition into the superconducting phase. The cuprates also display other phases which include a Fermi-Liquid regime and a strange metal regime that has properties dissimilar to the metallic Fermi-Liquid regime. At $T = 0$ a quantum critical point is thought to exist under the superconducting dome. [After C. Varma 2010] [4].

intermediate orbitals (superexchange). From this analysis magnetism may arise in insulating and conducting materials, where the macroscopic magnetic field which results from the exchange can be either ferromagnetic ($J > 0$) or anti-ferromagnetic ($J < 0$), when the temperature of the material is below the transition temperature T_c. In the ferromagnetic case all the spins at each lattice site are oriented in the same direction and in the anti-ferromagnetic case the spin orientation alternates in direction at adjacent lattice sites of a bipartite lattice. Theoretically to solve for the properties of the magnetic phase of materials is complicated, requiring the diagonalization of a matrix with Avogadro's number of entries in order to calculate the magnetic ground-state, which is thus far an intractable problem. To make the problem tractable requires a self-consistent mean-field calculation, or non-perturbative methods such as quantum Monte Carlo are used in an attempt to allow theorists to better understand the magnetic properties of materials. A more technical overview of magnetism will be introduced in chapter 2 of this thesis.

1.2.3 Kondo Phenomenon

Another strongly correlated system which results from the magnetic exchange between itinerant and localized electrons occurs in the Kondo effect. A non-magnetic material, such as gold, is doped with a small amount of iron ions. As the temperature of the material is reduced and as a result the spin degree of freedom of the conduction electrons, they scatter off the iron atoms resulting in an increase in the resistivity of these materials. This phenomenon was discovered experimentally in the 1930's where the resistivity of the nonmagnetic material was expected to linearly drop to zero. This did not happen but instead the resistivity at low temperatures exhibited a minimum, and as the temperature decreased below this minimum the resistivity increased. The increase in the resistivity was the result of a direct magnetic interaction between the magnetic impurities and conduction electrons. This phenomenon was explained theoretically by Jun Kondo in 1964 where he showed that perturbation theory diverged at low temperatures as a result of the magnetic interaction between the magnetic impurities and conduction electrons, and was able to link this divergence to a resistance minimum [6]. The Kondo effect is a central theme used to explain the cerium volume collapse portion of this thesis and therefore we will elaborate on it extensively in Chapter 5.

1.3 Magnetic Materials

Magnetism in condensed matter physics occurs in two distinct contexts which have been classified as in-organic and organic magnetism. The distinction between inorganic and organic based magnets is that organic based magnets contain organic molecules in their unit cell, whereas inorganic materials do not contain organic molecules. The most common type of inorganic magnetic material is the transition metal iron (Fe), in which a unpaired electron spin residing in the $3d^6$ shell interacts directly with adjacent Fe ions, which results in ferromagnetism in these materials. Magnetism can also occur in doped semi-conductors; the best known case of this is gallium arsenide (GaAs) doped with small concentrations of manganese (Mn) to form (Ga,Mn)As. This material becomes ferromagnetic at temperatures below the transition temperature of $T_c = 173$K [7]. Theoretical calculations based on the Zener and double exchange models show that (Ga,Mn)As could be magnetic at room temperature with a T_c as high as 300K. In addition to ferromagnetism, (Ga,Mn)As still possesses p-type semiconducting properties, and the magnetic phase displays a spin polarized current. The duality of (Ga,Mn)As with regards to its magnetism and semiconducting properties, is regarded as a smart material and is also a candidate for spintronic devices. (Ga,Mn)As is

not a material which occurs naturally. Instead it is grown using a method called molecular beam epitaxy in which layers of the structure are grown . Growing magnetic semiconductors in this way has proved to be very time consuming and cost inefficient since it requires lots of material resources to develop these magnetic materials, where one of the primary goals of molecular beam epitaxy is to increase T_c of (Ga,Mn)As. In contrast to inorganic magnetic materials, organic magnets do not require molecular beam epitaxy and the samples can be grown chemically. Organic magnets have been proven to display a wide range of new magnetic functionality that inorganic magnets do not possess; these properties will be reviewed in chapter 2. In the next section we describe briefly one type of organic magnet that the author extensively researched.

1.3.1 Magnetic 0rganic Materials: Bimetallic Oxalates

The magnetic properties of a class of organic magnets called the bimetallic oxalates were a central theme of the author's research and are discussed extensively in chapters 2 through 4. The bimetallic oxalates structure shown in Fig. 1.2 consists of a two dimensional hexagonal network of transition metal ions M(II)M(III) situated at the vertices of the hexagon. The oxalate molecule separates the M(II) and M(III) ions and mediates the anti-ferromagnetic exchange between the two ions and it is responsible for the heavily induced crystal-field environment surrounding the ions and serves to change the orbital angular momentum of the transition ions. The two dimensional hexagonal structure are separated by an organic cation completing the three dimensional structure. As shown in chapter 2, the direction of the magnetization of the bimetallic oxalate Fe(II)F(III) changed sign at a temperature $T \approx 35K$ below the anti-ferromagnetic ordering temperature $T \approx 45K$. The reversal in the magnetization is called magnetic compensation. The author explored how other combinations of transition ions in the chemical formula M(II)M(III) would produce magnetic compensation using static self-consistent mean-field theory. We predicted that a number of ions would exhibit magnetic compensation, and this phenomenon depended critically on the crystal-field induced environment surrounding the ions which changed the orbital angular momentum of each ion. Additionally the mean-field calculations were also confirmed by quantum Monte Carlo methods which included quantum and temporal fluctuations not included within our mean-field calculations[8]. This method showned that the bimetallic oxalate compounds we predicted would exhibit magnetic compensation were also found to exhibit magnetic compensation in the presence of thermal and quantum fluctuations. Chapters 2 through 4 of this thesis pertain to the authors research on the bimetallic oxalates.
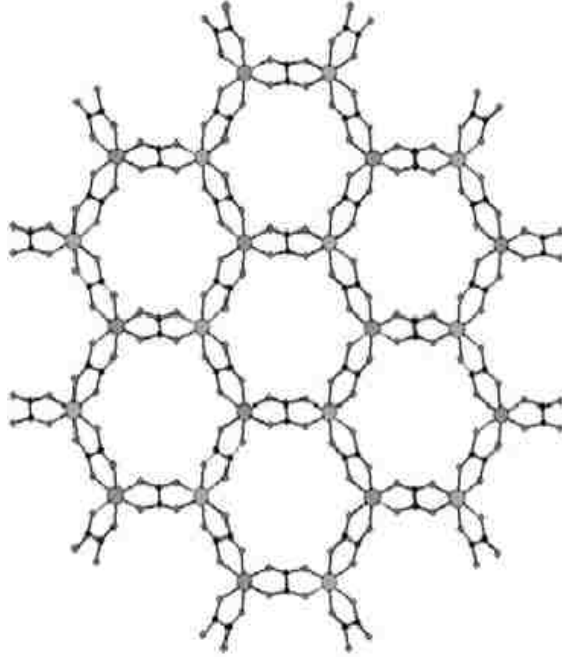
Figure 1.2: Bimetallic Oxalate honeycomb structure. Situated at the vertices in an alternating fashion are M(II) and M(III) transition metal ions, which interact via an oxalate molecule. [After Coronado 2006] [9].

1.4 Heavy Fermions

In condensed matter physics heavy fermions are another example of strongly correlated electronic materials in which large Coulomb correlations account for many of their properties. Heavy fermions are elements in which an electron resides in the partially filled inner f shell. Most atoms which fulfill this criteria on the periodic table are rare earth and actinide elements. Examples of compounds that exhibit heavy fermion properties are $CeCu_6$, $CeAl_3$ and UPt_3. Heavy fermions material possess this name since the effective mass $m^\star$ of the electrons in the conduction band of these materials is up to $m^\star = 1000m$ times larger than the mass of a free electron in a normal metal m [10, 11]. The increase in $m^\star$ is a result of the Kondo phenomenon which is a spin interaction which occurs between electrons in the broad s conduction band and impurity band formed by the f electrons residing in Ce, as a result a narrow band appears at the Fermi level which is commonly referred to as an Abrikosov-Suhl resonance which accounts for the increase in $m^\star$ [13, 12]. The Abrikosov-Suhl resonance at the Fermi level accounts for the increased resistivity and heat capacity of these materials at
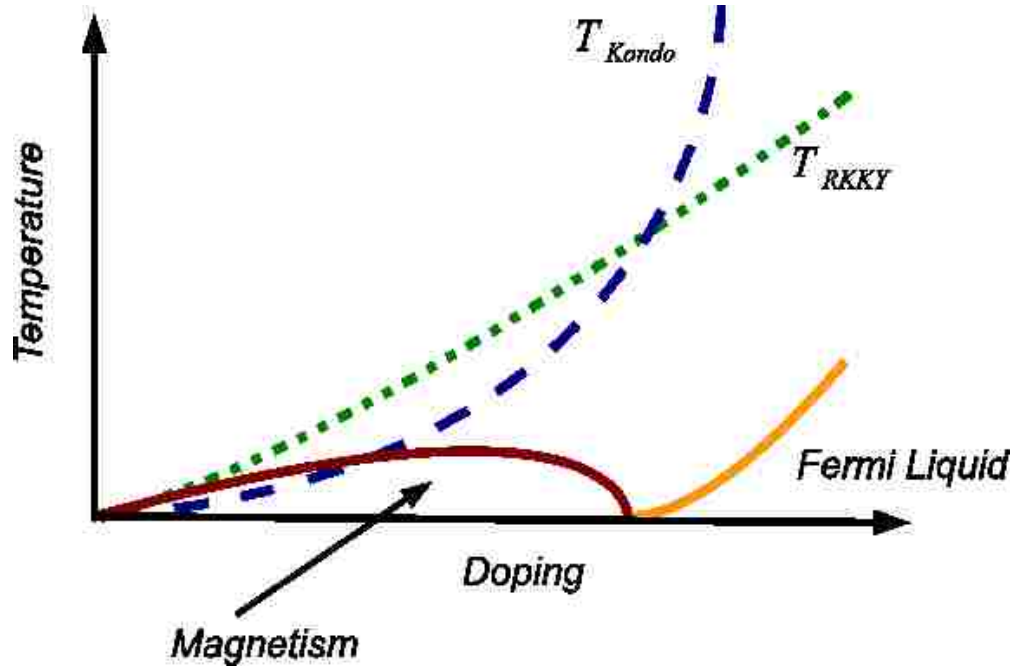
Figure 1.3: Doniach phase diagram as a function of temperature T vs. chemical doping δ. For small values of δ anti-ferromagnetic ordering results in heavy fermions for $T < T_{RKKY}$. Increasing the value of δ heavy-fermion compounds transition into the Fermi liquid regime which occurs for $T_K > T_{RKKY}$. [After Doniach 1977] [17].

low temperatures. The increase in $m^{\star}$ in heavy fermion compounds usually occurs when the temperature of the compounds is below a coherence temperature $T^{\star} \sim 10$K.

In addition to the increased resistivity and specific heat of these materials it was found experimentally that they exhibit a number of other interesting phenomena such as unconventional superconductivity and long range anti-ferromagnetic ordering associated with the Ruderman-Kittel-Kasuya-Yosida (RKKY) exchange between the impurity and conduction electrons [14, 15, 16]. The competition between these various phenomena resulted in the Doniach criteria, which states that there is a competition between the RKKY and Kondo effect at low temperatures depending on the concentration free carriers (Fig. 1.3) [17]. For example as the density of the free carriers is increased in the heavy fermion compound by chemical doping, the conduction band mediated anti-ferromagnetic interaction resulting from the RKKY effect is reduced, which results in an increased Kondo effect increasing the Kondo spin flip exchange.

1.4.1 Cerium Volume Collapse

Cerium in its solid form under a large pressure isostructurally collapses to a smaller volume phase. This is called the cerium volume collapse (CVC). When cerium collapses its volume is reduced by 18% relative to the large volume phase; this isostructural transition occurs under large pressure of 1.5 GPa and at a temperature of 480 K. The large volume phase of cerium is called the γ phase and the small volume phase is called the α phase Fig. 1.4. Neutron spectroscopy experiments showed that close to the Fermi level a sharp peak in the intensity occurred in the α phase reminiscent of a Kondo peak which was absent in the γ phase. The presence of this peak indicated that the KVC was primarily the result of Kondo quenching of the inner f electron in cerium by the conduction electron. Kondo phenomenon required that the entropy of the α phase would be zero. Another scenario that was used to explain the large peak in the spectral data was the Mott transition model. In this model the electron's kinetic energy in the α phase was smaller than the kinetic energy in the γ phase which resulted in a Mott insulator; however this picture was not able to explain that the fixed valence of the $4f$ level in cerium in both the phases (local moment regime), therefore this model was rejected. From pressure vs. temperature data used in conjunction with the Clausius-Clapeyron equation it was possible to extrapolate the change in the entropy $\Delta S_{\alpha,\gamma}$ as the temperature went to zero as cerium collapsed, and determine which state had larger entropy and rule in favor of the Kondo or Mott pictures as the deciding factor of the electronic collapse of cerium. What was found from extrapolating the Clausius-Clapeyron equations to $T = 0$ and extracting the entropy of each phase was the following. When cerium is in the γ phase the angular momentum of cerium given by Hund's rule is $J = 5/2$, consequently the entropy of the γ phase is $S_\gamma = k_B\ln(6)$, and the paramagnetic ground state is degenerate with magnetization $M_J = +5/2, \cdots -5/2$. However the entropy in the α phase was found to be $S_\alpha = k_B\ln(1) = 0$ indicating that the ground state is in a singlet $|0\rangle$ state which corresponds to the correct ground-state due to Kondo screening of the inner f electrons by the conduction electrons. These values of entropy indicate strongly that the reason for the electronic collapse of cerium was primarily due to Kondo screening which invalidated the collapse as the result of a Mott transition [18]. This explanation of the KVC is generally accepted, however it was recently found that as the temperature of cerium is increased that the phonon becomes more active and its contribution to the entropy change across the transition is nearly half of the electronic contribution $\Delta S_{\alpha,\gamma}^{\mathrm{phonon}} = k_B\ln(3)$. It would seem reasonable that at high temperatures that phonon's would become more active

9
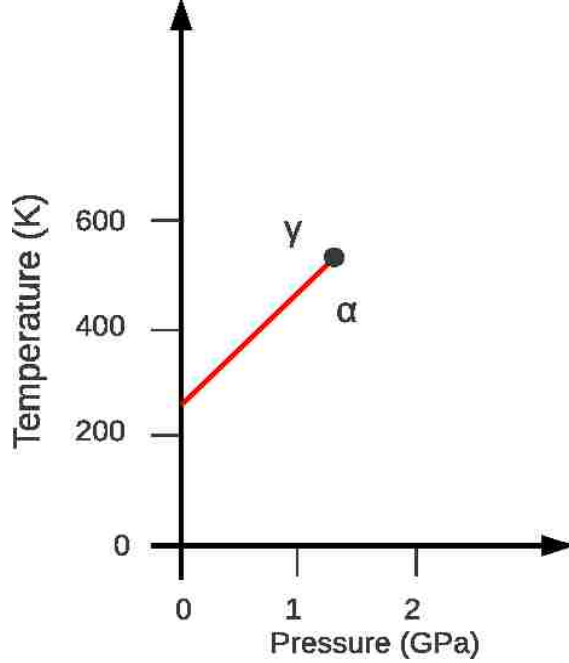
Figure 1.4: Phase diagram of Cerium in the vicinity of the $\alpha \leftrightarrow \gamma$ transition, illustrating that the slope of the coexistence line separating the small volume phase α from the large volume phase γ is positive, and therefore using the Clausius Clapeyron equation $\frac{\mathrm{d}P}{\mathrm{d}T} = \frac{\Delta S_{\alpha,\gamma}}{\Delta \Omega_{\alpha,\gamma}} > 0$, which implies that the entropy change $\Delta S_{\alpha,\gamma} < 0$ since the volume collapses gives $\Delta\Omega_{\alpha,\gamma} < 0$. [After Lipp (2008)][19].

since the specific heat due to phonon's is of the form $C = AT^3$. Consequently one would expect the electron-phonon interactions to be more relevant at higher temperatures also.

1.5   Breakdown of Perturbation Theory

Strongly correlated systems in condensed matter physics illustrate the breakdown of conventional perturbation theory. This happens because the kinetic energy and the potential energy due to the large Coulomb correlations between electrons are of the same order of magnitude, hence there is no small parameter to expand around to find the corresponding eigenenergies of the electrons. In the previous sections both the cuprate superconductors and the heavy fermion materials suffer from this problem since the physics of these problems is driven by large Coulomb correlations. In the case of the cuprate superconductors the ground state of the parent compound is an anti-ferromagnetic Mott insulator at half filling, thus large Coulomb correlations between electrons on adjacent sites prevent the electrons

from hopping. However when the system is doped away from half filling electrons can hop from site to site on the lattice. In the case of magnetically doped metals the system is in the Kondo phase since the RKKY interactions are negligible, and this phase only results from large Coulomb correlations between the conduction and impurity electrons, thus once again the kinetic and potential energies are of the same order of magnitude and conventional perturbation theory breaks down. These two primary examples of strongly correlated materials illustrate the need for a non-perturbative method of attack which allows for the analysis of strongly correlated materials, since conventional methods based on perturbation expansions about the dominant energy fail. Traditionally in the ordered state after perturbation theory breaks down theorists would resort to a mean-field argument with the knowledge of the groundstate wave function, in this way they were able to obtain a closed set of self-consistent equations which allowed them to solve for all the properties of the system. The most general example of this type is the Bardeen, Cooper and Schrieffer theory of superconductivity where perturbation theory breaks down. At this point any attempts to understand the ground-state properties of the cuprate superconductors have been based on two approaches. Either one can formulate the correct groundstate wave function, as Anderson proposed by formulating the RVB state and doping it away from half filling, or one can construct the appropriate model which describes the doped system and calculate based on a method which is self-consistent and without a priori knowledge of the groundstate. The latter approach has become a widespread and useful method that has allowed physicists to uncover the nature of highly correlated electronic materials, such as cuprate superconductors and heavy fermion compounds, and the former approach is still an active area of research since the ground state wave function of the cuprates is not known.

1.6 Dynamical Mean Field Theory

As mentioned in the last section, strongly correlated materials in which the electronic kinetic and potential energies are of the same order can be analyzed with the use of the non-perturbative self-consistent method called the Dynamical Mean Field Theory (DMFT) [20]. In DMFT one site within the lattice called the impurity site is singled out and electrons can hop on and off of the impurity with a hopping amplitude t and experience a Coulomb repulsion when two electrons of opposite spin occupy the impurity site at the same time. When the number of adjacent sites, z, to the impurity site goes to ∞ and the hopping is scaled in such a way as to keep the kinetic energy finite $t^{\star} = t\sqrt{z}$ as $z \to \infty$, a self-consistent

set of equations are generated which describe the quantum-mechanical probability amplitude $G_{\text{Impurity}}(\omega)$ of the electron to be at the impurity. From the information of $G_{\text{Impurity}}(\omega)$ it is possible to extract all the physical properties of interest in strongly correlated systems. In more traditional mean-field theories, where the spatial and temporal correlations are frozen out, the impurity feels the presence of the lattice in a static way. This is not the case within DMFT, one finds that the spatial correlations of the impurity still remain frozen out, where the temporal correlations are preserved hence the name Dynamical Mean Field Theory.

Here I will briefly outline the self-consistency cycle of DMFT, and the goal is to calculate the impurity quantum mechanical amplitude $G_{\text{Impurity}}(\omega)$. In general the self-consistency requires that the impurity amplitude $G_{\text{Impurity}}(\omega)$ and the coarse grained lattice amplitude $G_{\text{Lattice}}(\omega) = \sum_{\mathbf{k}} G(\mathbf{k}, \omega)$ are the same at the end of the self-consistent calculation, thus $G_{\text{Impurity}}(\omega) = G_{\text{Lattice}}(\omega)$. In general what this requirement means is that the impurity and the lattice are in equilibrium. To achieve equilibrium there is an equation that connects $G_{\text{Impurity}}(\omega)$ and $G_{\text{Lattice}}(\omega)$ which is the bath function $\mathcal{G}(\omega)$, which is calculated from the Dyson's equation via $\Sigma(\omega) = \mathcal{G}^{-1}(\omega) - G^{-1}_{\{\text{Impurity or Lattice}\}}(\omega)$, where $\Sigma(\omega)$ is the self-energy functional which is just the difference between the bath function and the impurity or lattice amplitudes. The following sequence is used to achieve self-consistency in DMFT. First we calculate the following quantities in the order outlined using $\Sigma(\omega)$ as input:

I . $G_{\text{Lattice}}(\Sigma(\omega))$

II . $\mathcal{G}^{-1}(\omega) = G^{-1}_{\text{Lattice}}(\omega) + \Sigma(\omega)$

III . $G_{\text{Impurity}}(\mathcal{G}(\omega))$

IV . $\Sigma(\omega) = \mathcal{G}^{-1}(\omega) - G^{-1}_{\text{Impurity}}(\omega)$

After the final step has been completed and a new $\Sigma(\omega)$ has been calculated it is used as input into the lattice amplitude in step I. $G_{\text{Lattice}}(\Sigma(\omega))$ and the process is continued until convergence is reached at which time $G_{\text{Impurity}}(\Sigma(\omega)) = G_{\text{Lattice}}(\Sigma(\omega))$. At this point it is clear how to compute $G_{\text{Lattice}}(\omega)$, $\mathcal{G}(\omega)$ and $\Sigma(\omega)$; next I will outline how to calculate $G_{\text{Impurity}}(\omega)$.

In general $G_{\text{Impurity}}(\omega)$ can be calculated in a number of different ways. The different methods used to calculate $G_{\text{Impurity}}(\omega)$ are the coherent potential approximation (CPA) for disordered systems, numerical renormalization group method (NRG) and quantum Monte Carlo (QMC) method. To obtain the ground-state properties of the system NRG is used to calculate $G_{\text{Impurity}}(\omega)$, however it is also desirable to know $G_{\text{Impurity}}(\omega)$ at finite temperatures then one would use QMC as the impurity solver.

1.7 Continuous Time Quantum Monte Carlo

Continuous Time Quantum Monte Carlo (CTQMC) is used in the DMFT cycle to calculate the impurity amplitude $G_{\text{Impurity}}(\omega)$ [22, 21]. Monte Carlo methods have been successfully employed to calculate complicated transcendental integrals of the form $I = \int_a^b f(x)dx$ numerically for years by randomly sampling the function $f(x)$ over the interval from $[a, b]$ and arriving at an estimation of I using the mean value theorem $I = \frac{1}{N}\sum_i^N f(x_i)(b - a)$, where x_i is randomly distributed in the interval $[a, b]$, or rather $x_i \; \epsilon \; [a, b]$ and N is the number of times the function $f(x)$ was sampled in the interval $[a, b]$. Similarly the impurity amplitude is also a multidimensional-dimensional integral

$$G_{\text{Impurity}}(\tau) = \sum_{n=0}^{\infty} \int_0^{\beta} d\tau_1 \cdots d\tau_n f(\tau_1, \cdots, \tau_n, \tau) \tag{1.1}$$

where the function $f(\tau_1, \cdots, \tau_n, \tau)$ will be explained in a later section and $\beta = \frac{1}{k_b T}$ is inverse temperature. This integral for the impurity amplitude $G_{\text{Impurity}}(\tau)$ is sampled using Monte Carlo, where τ and n are randomly sampled in the intervals $\tau \; \epsilon \; [0, \beta]$ and $n \; \epsilon \; [0, \infty]$. In practice this integral is calculated at finite temperature and convergence is achieved when the average order of the sum $\sum_{n=0}^{\infty}$ in $G_{\text{Impurity}}(\tau)$ is given by $\langle n \rangle \sim \beta U$ where U is the Coulomb repulsion between two electrons of opposite spin which occupy the impurity at the same time; when this condition for the average order is satisfied the Monte Carlo sampling of $G_{\text{Impurity}}(\tau)$ has reached thermal equilibrium. After equilibration we calculate the impurity amplitude $G_{\text{Impurity}}(\omega)$ by performing the Fourier transform

$$G_{\text{Impurity}}(\omega) \;\; = \;\; \frac{1}{\beta}\int_0^{\beta} G_{\text{Impurity}}(\tau)e^{i\omega\tau}\mathrm{d}\tau. \tag{1.2}$$

1.8 Structure of Thesis

The structure of this thesis will be presented in the following order according to subject matter. Chapters two through four of the thesis will outline and overview the author's research on the bimetallic oxalates. Chapters 5 through 7 will overview the author's research on the cerium volume collapse and chapter 8 will contain the conclusion of the thesis. Appendix A will contain a detailed derivation of the internal energy; and will also incorporate a derivation of the high frequency conditioning used to construct $\Sigma(\omega)$.

Chapter 2

Molecule Based Organic Magnets

2.1 Introduction to Molecule Based Organic Magnetism

Historically magnetism derives from atomic based organic materials composed of transition metals with a partially filled d shell (e.g. Fe, Co, Ni), however recently magnetism has also been found in molecular based inorganic materials. Since magnetic ordering was first reported in hexacyanometallates [23] in 1956 with $T_c < 50$ K, organic magnets have been synthesized in 1D chains, 2D layered structures and 3D structures which exhibit a wide range of magnetic transition temperatures which vary from 1 K in nitronylnitroxide radicals to above room temperature $T_c \sim 400$ K in the compound V[TCNE]$_x$ [24, 25, 26, 27]. Traditionally conventional inorganic magnetic materials require expensive metallurgical applications to fabricate and manipulate their magnetic properties; in contrast the synthesis and fabrication of organic magnets is based on synthetic organic chemistry methodologies which allows for an easier construction and manipulation of the underlying properties such as the structure, electric and magnetic properties of organic magnets. The synthesis of organic magnets is similar to what is used in the pharmaceutical industry in the preparation of medicines. Since the basic building blocks of organic magnets are molecules rather than atoms, the main focus area of study of these materials has come from organic and coordination chemistry, with theoretical investigations being carried out by physicists in an effort to better understand these materials from a microscopic view point, in an effort to assist in predicting other organic magnets which hitherto have not been synthesized or characterized. The crystal structure of the organic magnet and its resulting physical properties depend crucially on the underlying geometry of the basis molecule, since the magnetic properties of the crystal are molecular in origin rather than atomic (as in the case of inorganic materials), consequently one can expect a wide variety of emergent and exotic phenomenan to occur, since molecular interactions are much weaker than atomic interactions. As an example photomagnetic behavior has been reported in the molecule-based magnet $K_{0.2}Co_{1.4}[Fe(CN)_6]6.9H_2O$ in which elec-

tromagnetic waves incident on this material serve to tune the magnetism of this compound [28, 29]. Organic magnetic materials are one example of a smart material in which the magnetic properties can be controlled by the influence of an external stimuli such as pressure or photo-responsiveness, these materials have many applications which will serve to be useful in the coming years.

This chapter is structured in the following order in an effort to outline the magnetic properties of organic magnets: In section 2.2 we describe how magnetism results in molecule based magnets from unpaired spins of electrons in atoms, which results in long range magnetic ordering in these crystals below a characteristic temperature called the transition temperature T_c. Section's 2.3 and 2.4 will contain a detailed calculation of the spin wave spectrum of the Heisenberg ferromagnet and anti-ferromagnet. In section 2.4 we will focus on a particular class of organic magnets called the bimetallic oxalates which have the chemical formula A[M(II)M′(III)(ox)$_3$], where M(II) and M′(III) are transition metal ions with valences +2 and +3 respectively that are coupled by an oxalate molecule ox = C$_2$O$_4$ which forms a two dimensional open-honeycomb lattice, where A is an organic cation perpendicular to the two dimensional structure [30].

2.2   Magnetic Characterization

Long-range magnetic order in magnetic materials is the result of unpaired electronic spins residing in the atomic shells and how these unpaired spins in neighboring shells interact with one another determines the magnetic order of the material. Magnetic ordering in (e.g. Fe, Co, Ni) and most inorganic magnetic materials depends critically on the overlap or covalent bonding of the wave functions of unpaired electrons on adjacent sites and the Pauli exclusion principle. However the traditional magnetic exchange does not seem to be the case in organic materials since the magnetic atoms with unpaired spins residing in molecules are well separated and therefore no overlap of the wave-functions results in the magnetic exchange process, rather the intermediate oxalate molecule in the case of the bimetallic oxalates or the cations separating the magnetic ions is a necessary component in order for magnetism to exist in molecular-based magnets. The long-range magnetic behavior and magnetic coupling J between the unpaired spins in organic magnetics are determined according to a Curie law [31, 32] which states that the magnetic susceptibility scales as,

$$\chi \ = \ \frac{C}{T - \theta}. \tag{2.1}$$

In the case that neighboring spins do not interact and the spin arrangements ↑↓ and ↑↑ or ↓↓ are distributed throughout the material randomly, magnetic ordering can only occur in the presence of a non-zero magnetic field applied to the material. When the field is removed the magnetic order is lost, this type of magnetism is called paramagnetism. Paramagnetism requires that the Curie temperature $\theta = 0$ since the material does not magnetically order.

The magnetic coupling J is a parameter in the Heisenberg Hamiltonian which describes the magnetic coupling between adjacent atomic spins $-J\mathbf{S} \cdot \mathbf{S}'$, if $J > 0$ then the adjacent spins will tend to align parallel ↑↑. We call this ordering ferromagnetic where the Curie temperature $\theta > 0$. When $J < 0$ neighboring spins will align anti-parallel ↑↓ and the resulting magnetic order is called anti-ferromagnitism. In this case the Curie temperature is negative, $\theta < 0$, and magnetic ordering might occur when $T < |\theta|$. An additional type of magnetic order may occur when the magnetic exchange coupling $J < 0$ when neighboring electronic spins do not exactly cancel, the resulting magnetism is called ferrimagnetic and a magnetic moment can exist in the ground state and the Curie temperature remains negative $\theta < 0$ which implies that the magnetic exchange $J < 0$ is also negative.

In experiments the determination of the variety of different magnetic orderings which may occur in organic magnets is primarily based on the susceptibility in the presence of an external magnetic field H. Here we briefly review how to calculate the paramagnetic susceptibility of a free atom in a magnetic field H and how this measurement is the standard benchmark used to determine other types of magnetism for instance ferromagnetism and antiferromagnetism arising in other materials.

For a free ion within a solid the total moment can be written as $g(JLS)\mathbf{J} = \mathbf{L} + g_0\mathbf{S}$, where g_0 is the electronic g-factor which has a value close to 2.0023 in most solids, and $g(JLS)$ is a proportionality constant (which depends on the good quantum numbers (JLS)). This theorem allows for the calculation of matrix elements of the orbital and spin angular momentum $\langle \mathbf{L} + g_0\mathbf{S} \rangle$ involving the factor g_0 to be calculated in terms of matrix elements of the total angular momentum operator $g(JLS)\langle \mathbf{J} \rangle$ times the proportionality constant $g(JLS)$ which is diagonal for the expectation of $\langle \mathbf{J_z} \rangle$ in the basis $|JLSJ_z\rangle$,

$$\langle JLSJ_z|\mathbf{L_z} + g_0\mathbf{S_z}|J_z'SLJ\rangle \ = \ g(JLS)J_z\delta_{J_z,J_z'} \tag{2.2}$$

This matrix element will be important in the derivation of the magnetic susceptibility χ of a free ion.

Now when the free ion is placed into a magnetic field H_z which points in the z-direction, H_z interacts with the z-component of the magnetic moment of the atom $\mu_{\mathbf{z}}$. The corresponding interacting Hamiltonian is:

$$
\begin{aligned}
H_{int} &= -\mu_z H_z \\
&= -g(JLS)\mu_B J_z H_z,
\end{aligned}
\tag{2.3}
$$

as a consequence of the magnetic field H_z the degeneracy of the energy levels in the basis $|JLSJ_z\rangle$ ranging from $\{-J_z, -J_z + 1, ... + J_z - 1, +J_z\}$ is removed. μ_B is the the Bohr magneton and has the value $0.579\times$ eV/G. To calculate χ we will start from the calculation of the partition function Z using (2.3) as the Hamiltonian as input,

$$
Z = \sum_{J_z=-J}^{+J} e^{-\beta\gamma H_z J_z}
\tag{2.4}
$$

here $\beta = \frac{1}{k_B T}$ is inverse temperature, and $\gamma = g(JLS)\mu_B$. This sum in Z is geometric which can be summed explicitly to give

$$
Z = \frac{e^{\beta\gamma H_z(J+1/2)} - e^{-\beta\gamma H_z(J+1/2)}}{e^{\beta\gamma H_z/2} - e^{-\beta\gamma H_z/2}}.
\tag{2.5}
$$

Having calculated the partition function exactly we can now calculate thermodynamic quantities of interest which are the magnetization M and susceptibility χ, by performing the appropriate derivatives of $-\frac{\ln Z}{\beta}$ with respect to the external field H_z. The magnetization per unit volume is given by performing one derivative on $-\frac{\ln Z}{\beta}$ with respect to H_z

$$
\begin{aligned}
M &= -\frac{N}{V\beta}\frac{\partial \ln Z}{\partial H_z} \\
&= \frac{N}{V}\gamma J B_J(\beta\gamma J H_z).
\end{aligned}
\tag{2.6}
$$

Here $B_J(x)$ is called the Brillouin function and is defined to be

$$
B_J(x) = \frac{2J+1}{2J}\coth(\frac{2J+1}{2J}x) - \frac{1}{2J}\coth(\frac{1}{2J}x).
\tag{2.7}
$$

For comparison to experiment we are interested in how M initially varies in the presence of a

17

small applied external magnetic field H_z such that the system is magnetically perturbed, and at relatively high temperatures so any tendency for magnetic order is thermally removed. In particular we want to study the limiting value of (2.6) for the case that $\gamma H_z \ll k_B T$. In this limiting case the the Brillouin function can be written as

$$B_J(\beta\gamma J H_z) \approx \frac{J+1}{3J}(\beta\gamma J H_z) + O((\beta\gamma J H_z)^3), \qquad (2.8)$$

inserting this into (2.6) we find the limiting form of the magnetization to order $O((\beta\gamma J H_z)^3)$,

$$M = \frac{N}{V}\frac{(g\mu_B)^2}{3}\frac{J(J+1)}{k_B T}H_z. \qquad (2.9)$$

The magnetic susceptibility χ is calculated from (2.9) by performing the derivative

$$\chi = \frac{\partial M}{\partial H_z}$$
$$= \frac{N}{V}\frac{(g\mu_B)^2}{3}\frac{J(J+1)}{k_B T} \qquad (2.10)$$

which is valid in the limit $\gamma H_z \ll k_B T$. This result for χ in equation (2.10) is called Curie's law for the magnetic susceptibility of a paramagnetic material in which the magnetic behavior of the material is induced by the external field H_z. The Curie constant C may be deduced from equation (2.10) to be

$$C = \frac{N}{V}\frac{(g\mu_B)^2}{3}\frac{J(J+1)}{k_B} \qquad (2.11)$$

for a paramagnetic material $\theta = 0$, this value of C holds fairly well in insulating crystals and rare earth ions which have partially filled f shells, where the resulting angular momentum of the ion $\mathbf{J}$ is not affected by the surrounding crystal-field environment. In organic paramagnets Curie's constant is also upheld as long as the crystal-field surrounding the magnetic atom in the molecule does not affect the angular momentum of the partially filled shell of the magnetic ion; however, as we will demonstrate in a later section, the angular momentum of the magnetic ion in organic magnets is heavily influenced by the crystal-field and therefore the magnetic properties will deviate from that of a free ion.

Here we will overview how ferromagnetic and anti-ferromagnetic coupling between adjacent magnetic ions quantitatively differs from the Curie-like high-temperature paramagnetic form of χ found in equation (2.10), where in that case the magnetic ions did not interact.

In calculating the high-temperature magnetic susceptibility χ in the case of ferromagnetic and anti-ferromagnetic exchanges between adjacent ions we will find that χ diverges at a characteristic temperature $\theta \neq 0$. The starting point for the calculation of the magnetic susceptibility χ of ferromagnetic and anti-ferromagnetic ordering is the Heisenberg Hamiltonian in the presence of a magnetic field oriented along the z-axis H_z; this model describes the magnetic exchange $J_{i,j}$ between neighboring ion's, and each ion spin interaction with the magnetic field

$$H \;=\; -\sum_{i,j} J_{i,j} \mathbf{S}_i \cdot \mathbf{S}_j - g\mu_B H_z \sum_i S_{z,i,}. \tag{2.12}$$

If the magnetic exchange is positive, $J_{i,j} > 0$, then spin alignment between neighboring ions will be parallel. If the magnetic exchange is negative, $J_{i,j} < 0$, then the spin alignment between neighboring spins will favor anti-parallel alignment. To extract the high-temperature magnetic susceptibility from the Heisenberg Hamiltonian in (2.12) we use mean-field theory which isolates a particular spin at a lattice site $\mathbf{S}_i$ which allows for the determination of the magnetic properties of a single-site Hamiltonian, rather than solving the intractable problem of diagonalizing the N site problem that (2.12) poses, where N is a number the order of 0.6022×10^{24} atoms per mole (Avogadro's number). The mean-field Hamiltonian for the single site problem at site i is

$$\begin{aligned} H_{int,i} &\;=\; -\mathbf{S}_i \cdot \Big(\sum_{i \neq j} J_{i,j} \mathbf{S}_j + g\mu_B H_z \mathbf{z} \Big) \\ &\;=\; -g\mu_B \mathbf{S}_i \cdot \mathbf{H}_{eff}. \end{aligned} \tag{2.13}$$

One will notice the close resemblance between the effective Hamiltonians in equation (2.3) and (2.13). Consequently in order to calculate the magnetization M using our mean-field Hamiltonian in equation (2.13) just requires that we replace H_z in equation (2.6) by H_{eff}. Then the high-temperature expansion of M within mean-field theory requires that we take the limit $\gamma H_{eff} \ll k_B T$ which results in the same equation as (2.9) with H_z replaced with H_{eff}, and the magnetic susceptibility χ follows by constructing the ratio $\frac{M}{H_z}$. Before calculating these quantities we need to make a mean-field argument that justifies the linearization of equation (2.13) into a single-site problem. This requires replacing $\mathbf{S}_j$ in H_{eff} by its average value which is related to the magnetization per unit volume M via the relation

$$\langle \mathbf{S}_j \rangle \;=\; \frac{V}{N} \frac{M}{g\mu_B}. \tag{2.14}$$

19

Notice that the right hand side of (2.14) does not depend on the lattice site. The effective interaction H_{eff} can be written in the following way using (2.14)

$$
\begin{aligned}
H_{eff} &= H_z + \frac{1}{g\mu_B} \sum_{j \neq i} J_{i,j} \langle \mathbf{S}_j \rangle \\
&= H_z + \frac{V}{N} \frac{M}{(g\mu_B)^2} \sum_{j \neq i} J_{i,j} \\
&= H_z + \lambda M
\end{aligned}
\tag{2.15}
$$

where $\lambda = \frac{V}{N(g\mu_B)^2} \sum_{j \neq i} J_{i,j}$. In the high temperature limit $\gamma H_{eff} \ll k_B T$ within mean-field theory M can be calculated from (2.9) with the replacement that $H_z \Rightarrow H_{eff}$ therefore the mean-field magnetization depends on itself

$$
M = \frac{C}{T}(H_z + \lambda M)
\tag{2.16}
$$

solving for M we find

$$
M = \frac{CH_z}{T - C\lambda}.
\tag{2.17}
$$

Therefore the magnetic susceptibility is given by

$$
\begin{aligned}
\chi &= \frac{M}{H_z} \\
&= \frac{C}{T - C\lambda} \\
&= \frac{C}{T - \theta},
\end{aligned}
\tag{2.18}
$$

where χ diverges at the critical temperature $T_c = \theta = C\lambda$. The critical temperature T_c for which χ diverges depends critically on the value and sign of the magnetic exchange $J_{i,j}$; three cases may arise as illustrated in the following table,

$$
T_c = \begin{cases} \theta > 0 & \text{if } J_{i,j} > 0 \Rightarrow Ferromagnetic \\ \theta = 0 & \text{if } J_{i,j} = 0 \Rightarrow Paramagnetic \\ \theta < 0 & \text{if } J_{i,j} < 0 \Rightarrow Anti-Ferromagnetic. \end{cases}
$$

Magnetic characterization of organic magnets where the magnetism results from the magnetic exchange $J_{i,j}$ between localized atomic spins mediated by an intermediate oxalate molecule makes use of the magnetic susceptibility χ in (2.18) extensively to properly deter-

20
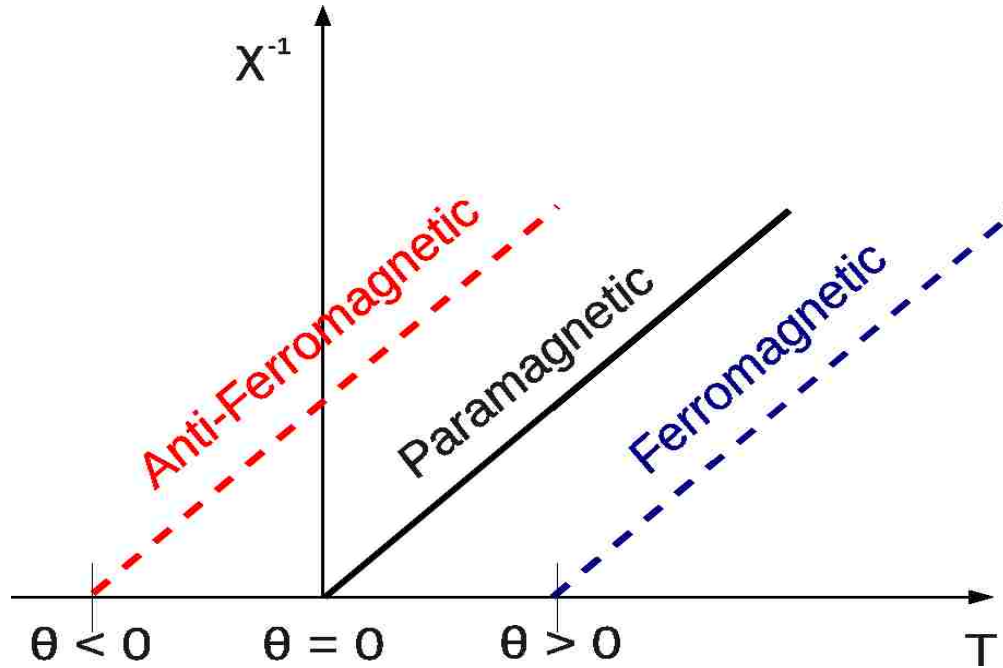
Figure 2.1: Plots of the inverse of the high temperature magnetic susceptibility χ^{-1} for the case that magnetic exchange between atoms favors anti-parallel spin alignment (Anti-Ferromagnetism) in this case the critical temperature $\theta < 0$, in the case that no magnetic exchange occurs between atoms (Paramagnetism) $\theta = 0$, and when the magnetic exchange between atoms favors parallel alignment (Ferromagnetism) the transition temperature is given by $\theta > 0$.

mine magnetic coupling and ultimately the onset of long-range magnetic behavior in these materials. Experimentally a rough estimate of the critical transition temperature $T_c = \theta$ and the magnetic ordering is determined by evaluating the inverse of the high-temperature magnetic susceptibility χ^{-1} data which is compared against Figure 2.1 to determine whether the material tends to order ferromagnetically, para-magnetically or anti-ferromagnetically.

2.3 Spin Waves

The low lying excitations in the ferromagnetic and antiferromagnetic Heisenberg model are called spin waves and are of interest since they allow for the direct comparison to neutron diffraction experiments of materials. In the next couple of sections we will calculate the spin wave excitation spectrum in the ferromagnetic Heisenberg model and we will discover that the excitation spectrum is quadratic, $\omega(\mathbf{k}) \sim k^2$. Also we will calculate the anti-ferromagnetic

spin wave excitation spectrum and find it has a linear excitation relation $\omega(\mathbf{k}) \sim k$. The differences in the two spin wave excitation spectrums are a direct consequence of different magnetic exchanges in the ferromagnetic and anti-ferromagnetic case and this results in different thermodynamic properties between ferromagnetic and anti-ferromagnetic materials. For example the specific heat of a ferromagnet will obey the Bloch law at low temperatures $T^{3/2}$ and in the anti-ferromagnetic case will have the resulting form T^3.

2.3.1   Spin-Waves in the Ferromagnetic Heisenberg Model

Here we will calculate the spin wave excitation spectrum of the Heisenberg model by performing a Holstein-Primakoff transformation. The Heisenberg Hamiltonian in the presence of an external magnetic field oriented along the z-direction has the following form

$$H \quad = \quad -J\sum_{j,\delta}\mathbf{S}_j\cdot\mathbf{S}_{j+\delta} - 2\mu_0 H_0\sum_j S_{jz}. \tag{2.19}$$

Here $-J$ corresponds to ferromagnetic exchange between two adjacent atoms in the lattice, the sum over j runs over all lattice sites and δ is summed over all the nearest neighbors sites; the term $\mathbf{S}_j\cdot\mathbf{S}_{j+\delta}$ represents the spin interaction between the atom at site j with spin $\mathbf{S}_j$ and the nearest neighbor site $\mathbf{S}_{j+\delta}$. μ_0 is the magnetic moment of the atom with spin S_{jz} and H_0 is an external magnetic field which introduces anisotropy into the systems which serves to break the spin symmetry.

The first step to calculate the excitation spectrum is to write the Hamiltonian in (2.19) in terms of the independent operators S^+, S^-, S_z. This is possible since

$$\begin{aligned} S_j^+ &= S_{jx} + iS_{jy} \\ S_j^- &= S_{jx} - iS_{jy}. \end{aligned} \tag{2.20}$$

Using S_j^+ and S_j^- it is possible to invert these equations to solve for S_{jx} and S_{jy} and insert them into (2.19)

$$\begin{aligned} S_{jx} &= \frac{1}{2}(S_j^+ + S_j^-) \\ S_{jy} &= \frac{1}{2i}(S_j^+ - S_j^-) \end{aligned} \tag{2.21}$$

Using this representation for S_{jx} and S_{jy} in (2.19) the Heisenberg Hamiltonian has the

following form

$$H = -J \sum_{j,\delta} \{\frac{1}{2}(S_j^+ S_{j+\delta}^- + S_j^- S_{j+\delta}^+) + S_{zj} S_{zj+\delta}\} - 2\mu_0 H_0 \sum_j S_{jz}. \qquad (2.22)$$

Next we employ the Holstein-Primakoff transformation of S_j^+, S_j^- and S_{zj}

$$
\begin{aligned}
S_j^+ &= \sqrt{2S}(1 - \frac{a_j^\dagger a_j}{2S})^{\frac{1}{2}} a_j \\
S_j^- &= \sqrt{2S} a_j^\dagger (1 - \frac{a_j^\dagger a_j}{2S})^{\frac{1}{2}} \\
S_{zj} &= S - a_j^\dagger a_j,
\end{aligned}
\qquad (2.23)
$$

into the bosonic variables $a_j^\dagger$ and a_j, which satisfy bosonic commutation properties

$$[a_j, a_l^\dagger] = \delta_{j,l}. \qquad (2.24)$$

At low temperatures the number of magnons that are thermally excited is small so the ratio $< a_j^\dagger a_j > /S << 1$ and therefore equations of S_j^+ and S_j^- simplify

$$
\begin{aligned}
S_j^+ &= \sqrt{2S} a_j \\
S_j^- &= \sqrt{2S} a_j^\dagger.
\end{aligned}
\qquad (2.25)
$$

Performing the Fourier transform we find the following forms for S_j^+, S_j^- and S_{zj}

$$
\begin{aligned}
S_j^+ &= \sqrt{\frac{2S}{N}} \sum_{\mathbf{k}} e^{-i\mathbf{k}\cdot\mathbf{x}_j} b_{\mathbf{k}} \\
S_j^- &= \sqrt{\frac{2S}{N}} \sum_{\mathbf{k}} e^{i\mathbf{k}\cdot\mathbf{x}_j} b_{\mathbf{k}}^\dagger \\
S_{zj} &= S - \frac{1}{N} \sum_{\mathbf{k}\mathbf{k}'} e^{i(\mathbf{k}-\mathbf{k}')} b_{\mathbf{k}}^\dagger b_{\mathbf{k}'}.
\end{aligned}
\qquad (2.26)
$$

Here S is the spin of the atoms in the lattice. Inserting equations (2.26) into the Hamiltonian (2.19) and performing the sum over the lattice and nearest neighbor sites we obtain the Fourier transformed Hamiltonian

$$H = \sum_{\mathbf{k}} \{2JzS(1 - \gamma_{\mathbf{k}}) + 2\mu_0 H_0\} b_{\mathbf{k}}^\dagger b_{\mathbf{k}}$$

$$= \sum_{\mathbf{k}} \omega(\mathbf{k}) b_{\mathbf{k}}^{\dagger} b_{\mathbf{k}}. \tag{2.27}$$

Here we see that the spin wave spectrum has the following form

$$\omega(\mathbf{k}) = 2JzS(1 - \gamma_{\mathbf{k}}) + 2\mu_0 H_0. \tag{2.28}$$

Here $\gamma_{\mathbf{k}} = \frac{1}{z} \sum_{\delta} e^{i\mathbf{k} \cdot \delta}$. In the long wave length limit $\mathbf{k} \sim$ small number and the $e^{i\mathbf{k} \cdot \delta}$ can be expanded for a square lattice to give $1 - (ka)^2$. So in the limit that the external field is set to zero, $H_0 = 0$, the spin wave excitation becomes

$$\omega(\mathbf{k}) = 2JzS(ka)^2. \tag{2.29}$$

When the external field is $H_0 \neq 0$ we see that as $k \to 0$ that $\omega(0) = 2\mu_0 H_0$; in this case there exists a gap in the spin wave spectrum, therefore in order to excite a spin wave would require an energy of $2\mu_0 H_0$ to be applied by the external agent. Here we see that the spin wave dispersion for the ferromagnetic exchange coupling has a quadratic dispersion in the spin wave momentum $\mathbf{k}$ in the long wavelength limit. When the specific heat is calculated using this dispersion relation one finds that the specific heat of a ferromagnet at low temperature obeys the Bloch law

$$C = aT^{3/2}. \tag{2.30}$$

2.3.2   Spin-Waves lin the Antiferromagnetic Heisenberg Model

In this section we calculate the spin wave excitation spectrum of the Heisenberg Antiferromagnetic Hamiltonian given by

$$H = J \sum_{j,\delta} \mathbf{S}_j \cdot \mathbf{S}_{j+\delta} - 2\mu_0 H_0 \sum_{j} S_{jz}^a + 2\mu_0 H_0 \sum_{j} S_{jz}^b. \tag{2.31}$$

In this equation the superscripts on S_{jz}^a and S_{jz}^b represent the z-component of the spin of sub-lattice a and b. In the case of antiferromagnetism the total spin S of sublattices a and b are the same, thus the anti-ferromagnetic order does not reveal itself as a magnetic field as in the case of the ferromagnet, since the spin of ions at adjacent lattice sites cancel. All the terms in this Hamiltonian are equivalent to the ferromagnetic case with the same understanding except the sign on the magnetic exchange is positive to reflect that magnetic exchange interaction between ions is positive in the case of antiferromagnetism. So to extract

the low lying elementary spin wave excitations we need to perform exactly the same steps as was done for the ferromagnet, however we need to keep track of the sub-lattice spin.

In order to achieve this we to transform equation (2.31) into the variables $S_{aj}^+, S_{aj}^-, S_{zj}^a$ and $S_{bj}^+, S_{bj}^-, S_{zj}^b$. This is possible using the relations

$$
\begin{aligned}
S_{jx}^a &= \frac{1}{2}(S_{aj}^+ + S_{aj}^-) \\
S_{jy}^a &= \frac{1}{2i}(S_{aj}^+ - S_{aj}^-) \\
S_{jx}^b &= \frac{1}{2}(S_{bj}^+ + S_{bj}^-) \\
S_{jy}^b &= \frac{1}{2i}(S_{bj}^+ - S_{bj}^-)
\end{aligned}
$$
(2.32)

Inserting these values into (2.31) we find that the Hamiltonian has the following form

$$
\begin{aligned}
H &= -J\sum_{j,\delta}\{\frac{1}{2}(S_{aj}^+ S_{bj+\delta}^- + S_{aj}^- S_{bj+\delta}^+) + S_{zj}^a S_{zj+\delta}^b\} \\
&\quad - 2\mu_0 H_0 \sum_j S_{jz}^a + 2\mu_0 H_0 \sum_j S_{jz}^b.
\end{aligned}
$$
(2.33)

Next we perform the Holstein-Primakoff transformation using the Fourier representation of $S_{aj}^+ \cdots S_{jz}^b$

$$
\begin{aligned}
S_{aj}^+ &= \sqrt{\frac{2S}{N}}\sum_{\mathbf{k}} e^{-i\mathbf{k}\cdot\mathbf{x}_j} c_{\mathbf{k}} \\
S_{aj}^- &= \sqrt{\frac{2S}{N}}\sum_{\mathbf{k}} e^{i\mathbf{k}\cdot\mathbf{x}_j} c_{\mathbf{k}}^\dagger \\
S_{bj}^+ &= \sqrt{\frac{2S}{N}}\sum_{\mathbf{k}} e^{-i\mathbf{k}\cdot\mathbf{x}_j} d_{\mathbf{k}}^\dagger \\
S_{bj}^- &= \sqrt{\frac{2S}{N}}\sum_{\mathbf{k}} e^{i\mathbf{k}\cdot\mathbf{x}_j} d_{\mathbf{k}} \\
S_{jz}^a &= S - \frac{1}{N}\sum_{\mathbf{k}\mathbf{k}'} e^{i(\mathbf{k}-\mathbf{k}')} c_{\mathbf{k}}^\dagger c_{\mathbf{k}'} \\
S_{jz}^b &= -S + \frac{1}{N}\sum_{\mathbf{k}\mathbf{k}'} e^{-i(\mathbf{k}-\mathbf{k}')} d_{\mathbf{k}}^\dagger d_{\mathbf{k}'}.
\end{aligned}
$$
(2.34)

Inserting these expressions into (2.33) and performing the sum over the j and δ we obtain

the following expression for the Hamiltonian in momentum space,

$$H \;=\; 2JzS\sum_{\mathbf{k}}\{A_1(\mathbf{k})(c_{\mathbf{k}}d_{\mathbf{k}} + c_{\mathbf{k}}^{\dagger}d_{\mathbf{k}}^{\dagger}) + (A_2 + A_3)(c_{\mathbf{k}}^{\dagger}c_{\mathbf{k}} + d_{\mathbf{k}}^{\dagger}d_{\mathbf{k}})\}. \tag{2.35}$$

Here we have defined

$$A_1(\mathbf{k}) \;=\; 2JzS\gamma_{\mathbf{k}} \tag{2.36}$$
$$A_2 \;=\; 2JzS \tag{2.37}$$
$$A_3 \;=\; 2\mu_0 H_0. \tag{2.38}$$

The Hamiltonian in equation (2.35) is not in diagonal form. To diagonalize it we use the equation of motion technique where we defined

$$i\frac{du_{\mathbf{k}}}{dt} = [\underline{u}_{\mathbf{k}}, H] = \underline{M}_{\mathbf{k}}\,\underline{u}_{\mathbf{k}} = \omega_{\mathbf{k}}\underline{u}_{\mathbf{k}}, \tag{2.39}$$

here $\underline{u}_{\mathbf{k}}$ and $\underline{M}_{\mathbf{k}}$ are defined by

$$\underline{u}_{\mathbf{k}} \;=\; \left\{\begin{array}{c} c_{\mathbf{k}} \\ d_{\mathbf{k}}^{\dagger} \end{array}\right\} \tag{2.40}$$

$$\underline{M}_{\mathbf{k}} \;=\; \left\{\begin{array}{cc} A_2 + A_3 & A_1(\mathbf{k}) \\ -A_1(\mathbf{k}) & -(A_2 + A_3) \end{array}\right\}. \tag{2.41}$$

To calculate the eigen-frequencies from (2.39) we calculate $\mathrm{Det}(\underline{M}_{\mathbf{k}} - I\omega_{\mathbf{k}})$ and we find that the eigen-frequencies are given by

$$\omega_{\mathbf{k}} \;=\; \sqrt{(A_2 + A_3)^2 - A_1(\mathbf{k})^2}$$
$$\;=\; \sqrt{(2JzS + 2\mu_0 H_0)^2 - (2JzS\gamma_{\mathbf{k}})^2}. \tag{2.42}$$

Just as in the case of the ferromagnetic on a square lattice when $k \to 0$ one should expect a spin gap to appear of the order $2\mu_0 H_0$. In the case that the external field is zero, $H_0 = 0$, then 2.42 reduces to the following form

$$\omega_{\mathbf{k}} \;=\; 2JzS\sqrt{1 - \gamma_{\mathbf{k}}^2}. \tag{2.43}$$

For a square lattice in the long wavelength limit this formula reduces to

$$\underline{\omega}_{\mathbf{k}} = 2JzS(ka). \qquad (2.44)$$

We obtained the very important result that the spin wave dispersion for an anti-ferromagnet is a linear function of the spin wave momentum $\mathbf{k}$, which is very different from the quadratic behavior in the ferromagnetic case. In addition using the anti-ferromagnetic spin wave dispersion one can show that the heat capacity of an anti-ferromagnetic will have the following form

$$C = BT^3. \qquad (2.45)$$

2.4 Bimetallic Oxalates

The Bimetallic Oxalates are one particular family of organic magnets which have the chemical formula $A[\text{M(II)M}'(\text{III})(\text{ox})_3]$, where A is an organic cation that separates the negatively charged hexagonal metallic layers and M(II) and M$'$(III) are transition metal ions with valences of plus $+2$ and $+3$ respectively, and are separated by an oxalate molecule, $ox = C_2O_4$. Magnetic exchange occurs between M(II) and M$'$(III) and the sign of the exchange depends critically on the choice of the transition metal ion M(II) and M$'$(III); the magnetic exchange can be either ferromagnetic or antiferromagnetic. Early theoretical attempts to better understand these materials was first carried out by Fishman and Reboredo on the ferrimagnetic bimetallic oxalate compound Fe(II)FeIII which exhibits a magnetization reversal, where the direction of the magnetization changed at a temperature of 28K below the ferrimagnetic transition temperature of 45K. Modeling the bimetallic oxalate Fe(II)FeIII Fishman and Reboredo considered a model Hamiltonian that incorporated the effects of the crystal field due to the $ox = C_2O_4$ molecule which changed the orbital angular momentum of the Fe(II) ion. This model also incorporates the effects of the ferrimagnetic exchange $J\mathbf{S}_{II} \cdot \mathbf{S}_{III}$ coupling between the two ions and the effect of spin-orbit coupling $\lambda \mathbf{L}_{II} \cdot \mathbf{S}_{II}$ on the Fe(II) ion [33]. To successfully capture the magnetization reversal in the bimetallic oxalates Fe(II)FIII the inclusion of the crystal-field and spin-orbit coupling of about the Fe(II) ion was only relevant because the angular momentum of Fe(II) and Fe(III) ions given by Hund's rule were $L_{II} = 2$ and $L_{III} = 0$, therefore any crystal-field induced effect on Fe(III) could be neglected. X-ray diffraction measurements data showed that the oxygen atoms around Fe(II) ion formed a

triangle above and below the ion that were rotated by 48° from one another. From the symmetry of the crystal-field environment around the Fe(II) ion it was possible to construct the crystal-field potential $V(\rho, \theta, \phi)$. After constructing the crystal-field potential Fishman and Reboredo formulated the matrix Hamiltonian $H^{cf} = \langle m|V(\rho, \theta, \phi)|m\rangle$ where $m = 0, \pm 1, \pm 2$ which they diagonalized and found a pair of degenerate low-energy orbital doublets $|\psi_{1,2}\rangle$ with energies $\epsilon_{1,2} = \epsilon^0 = ((\gamma + \gamma') - r)/2$, where γ, γ' and r were non-zero overlap integrals of the crystal-field potential constructed in the Hilbert space of $|m\rangle$. These states also had a non-zero value associated with the z component of the orbital angular momentum calculated from the matrix elements

$$
\begin{aligned}
\langle\psi_1|L_z|\psi_1\rangle &= -\langle\psi_2|L_z|\psi_2\rangle \\
&= \frac{2|\alpha|^2 - (\gamma - \gamma')^2 - (\gamma - \gamma')r}{4|\alpha|^2 - (\gamma - \gamma')^2 + (\gamma + \gamma')r}.
\end{aligned}
\tag{2.46}
$$

It was found that the crystal-field induced angular momentum $L_z^{cf} = |\langle\psi_1|L_z|\psi_1\rangle|$ of Fe(II) would vary from unquenched ($L_z^{cf} = 2$) to completely quenched ($L_z^{cf} = 0$) values depending on the strength of the crystal-field. It was argued that if the temperature $T << |\epsilon^0|$ then the orbital double would have a lower energy than the singlet state $|0\rangle$ and therefore the ground-state of Fe(II) in the presence of the crystal-field would be the low energy doublet $|\psi_{1,2}\rangle$ which would have a non-zero value of angular momentum $L_z^{cf} \neq 0$ in the presence of the crystal-field.

The total magnetization $M = M_{II} + M_{III}$ was calculated in the low energy subspace $\epsilon^0 < 0$ and $L_z^{cf} > 0$ where the magnetization of Fe(II) ion was $M_{II} = \langle 2S_z + L_z\rangle$ and magnetization of $M_{III} = 2\langle S_z\rangle$. The magnetization was calculated with the use of the reduced mean-field Hamiltonians associated with the Fe(II) and Fe$'$(III) ions $H_{II} = \lambda \mathbf{L} \cdot \mathbf{S} + 3J\mathbf{S_{II}} \cdot \langle\mathbf{S_{III}}\rangle$ and $H_{III} = 3J\mathbf{S_{III}} \cdot \langle\mathbf{S_{II}}\rangle$ respectively. Both Hamiltonians are diagonal in the subspace of $|\psi_1, \sigma\rangle$ $\sigma = 0, \pm 1, \pm 2$. The energy of $\langle H_{II}\rangle$ in the state $|\psi_1, \sigma\rangle$ was found to be $\epsilon_{1\sigma} = \epsilon^0 + (\lambda L_z^{cf} + 3JM_{III})\sigma$ and in $|\psi_2, \sigma\rangle$ the energy was $\epsilon_{1\sigma} = \epsilon^0 + (-\lambda L_z^{cf} + 3JM_{III})\sigma$. The anisotropy due to the crystal field lifted the degeneracy of the low energy subspace $|\psi_{1,2}, \sigma\rangle$. The ensemble average of M_{II} was constructed with the use of $\epsilon_{\{1,2\},\sigma}$, however these energies depend on the magnetization M_{III} which was calculated using the Brillioun function since this site does not depend on spin-orbit coupling $M_{III}(T) = 2S_{III}B_{S_{III}}(-3S_{III}J\langle S_z^{II}\rangle/T)$. The total magnetization is calculated using the formula $M^{avg} = (M_{II} + M_{III})/2 = (|M_{II}| - |M_{III}|)/2$, since $M_{II}(M_{III})$ and $M_{III}(M_{II})$ require that M_{II} and M_{III} be calculated self-consistently. Within this mean-field calculation they found that for spin-orbit coupling $\lambda =$

$-8J$ and for the crystal-field angular momentum of $Fe(II)$ between the values $0.54 < L_z^{cf} < 1$, magnetization reversal was possible. This work indicated that the effect of the crystal field and spin-orbit interactions were responsible for the magnetization reversal observed in Fe(II)Fe(III).

Finally a Holstein-Primakoff transformation was performed on the ferrimagnetic Hamiltonian in the presence of the crystal-field of the Fe(II) ion in an effort to extract the spin-wave gap of these materials and it was found to be [34]

$$
\begin{aligned}
\Delta_{sw} &= \lambda L_z^{cf}/2 - 3J(S_{III} - S_{II})/2 \\
&+ \{9J^2(S_{III} - S_{II})^2 + (\lambda L_z^{cf})^2 - 6\lambda L_z^{cf} J(S_{III} + S_{II})\}^{1/2}/2.
\end{aligned}
\tag{2.47}
$$

Using this equation in conjunction with the values of L_z^{cf} in the region of magnetic compensation they were able to predict the value of the spin-wave gap in Fe(II)Fe′(III) which was found to be the order of $\Delta_{sw} \approx 1.65$meV.

In chapters 3 and 4 the author extends the research of Fishman and Reboredo in an effort to predict magnetic reversal in other compounds with the bimetallic oxalate structure that have the the chemical formula $A[\text{M(II)M}′\text{(III)(ox)}_3]$ by considering various combinations of transition metals M(II) and M′(III) ions . The extension involved incorporating spin-orbit coupling on both the M(II) and M′(III) ions. We found that there are a number of other bimetallic oxalates that should exhibit magnetic reversal and possess a large spin-wave gap due to the anisotropy of the crystal-field situated around the M(II) and M(III) ions.

Chapter 3

Magnetic Compensation in the Bimetallic Oxalates

3.1 Introduction

Bimetallic oxalates [1] are layered molecule-based magnets with either ferromagnetic or antiferromagnetic interactions between transition metals M(II) and M'(III) on an open honeycomb lattice. Some Fe(II)Fe(III) bimetallic oxalates exhibit magnetic compensation (MC) at a compensation temperature $T_{\mathrm{comp}} \approx 30$ K below the ferrimagnetic transition temperature $T_{\mathrm{c}} \approx 45$ K. To see if MC is possible in other bimetallic oxalates, we construct a theoretical model for bimetallic oxalates that exhibit antiferromagnetic interactions. By varying the M(II) and M'(III) average orbital angular momentum, which can be controlled by the choice of interlayer cations, we find regions of MC in the families M(II)Mn(III) with M = Fe, Co, or Ni and V(II)M'(III) with M' = Cr or V but not in the family M(II)Ru(III) with M = Fe or Cu.

One of the most intensively-studied molecule-based magnets, the bimetallic oxalates [50, 36] are isostructural layered compounds with the chemical formula A[M(II)M'(III)(ox)$_3$], where M(II) and M'(III) are transition-metal ions with valences +2 and +3. Coupled by the oxalate molecules ox = C_2O_4, M(II) and M'(III) form the open honeycomb lattice sketched in the inset to Fig.1. While the organic cation A between the bimetallic layers affects the overall properties of the material, it does not change the sign of the magnetic interactions between M(II) and M'(III), which can be either ferromagnetic or antiferromagnetic (AF) with moments pointing out of the layer.

When the magnetic interactions are AF, the moments on the M(II) and M'(III) sublattices may cancel at a compensation temperature T_{comp} below the ferrimagnetic transition temperature T_{c}. Magnetic compensation (MC) has been extensively documented in the Fe(II)Fe(III) compounds [37, 38, 39, 40, 41], where it occurs only for certain cations A.

---

[1]This chapter first appeared as: P. Reis, *et al.*, Phys. Rev. B, **77**, 174433 (2008). © APS. *From the website of the American Physical Society (APS).*

Fe(II)Fe(III) compounds that exhibit MC are reported to have higher values of the transition temperature $T_c \approx 45$ K and of the Curie-Weiss constant C, with $T_c \approx 30$ K [38]. In earlier papers [58], two of us developed a model that explains the appearance of MC in some Fe(II)Fe(III) compounds. In the present paper, we investigate three families of bimetallic oxalates where the AF interactions permit MC but MC has not yet been observed. We conclude that MC is possible in the M(II)Mn(III) (M = Fe, Co, or Ni) [9] and V(II)M'(III) (M' = Cr or V) [55] families but not in the M(II)Ru(III) (M = Fe or Cu) [44] family.

Strong experimental evidence indicates that the coupling between layers is not primarily responsible for the magnetic ordering of the bimetallic oxalates. In Fe(II)Fe(III) bimetallic oxalates with A = N(n-C$_n$H$_{2n+1}$)$_4$, the separation l between bimetallic layers grows from 8.2 Å to 10.2 Å as n increases from 3 to 5 [38]. If the magnetic order depended on the coupling between the layers, then T_c would decrease as n increases from 3 to 5 rather than increasing from 35 to 48 K. Perhaps even more compelling is the observation [45, 46] that the magnetic $s = 1/2$ cation FeCp$_2^*$ (Cp* = pentamethylcyclopentadienyl) hardly changes the transition temperature and coercive field of a wide range of bimetallic oxalates. Therefore, some mechanism besides interlayer coupling is needed to explain the magnetic ordering of well-separated bimetallic layers. Recent studies of Fe(II)Fe(III) compounds [58] demonstrated that the spin-orbit coupling on the Fe(II) (3d^6) sites can produce long-range magnetic order even for isolated two-dimensional layers. On the other hand, the spin-orbit coupling sums to zero on the Fe(III) (3d^5) sites.

We now extend that model to treat a more general class of bimetallic oxalates, where the spin-orbit coupling affects both the M(II) and M'(III) moments. The susceptibility measurements [9, 39, 55] discussed below reveal that the orbital angular momentum of most bimetallic oxalates is incompletely quenched. MC occurs if the M(II) or M'(III) ions initially order more rapidly with decreasing temperature, due to their stronger spin-orbit coupling, than the M'(III) or M(II) ions with the larger saturation moments. So within our model, spin-orbit coupling is responsible for both the two-dimensional order of well-separated layers and the MC within a single bimetallic layer. The cation A can change the magnitude of the spin-orbit coupling, which depends sensitively on the crystal-field potential, but not the sign of the magnetic interaction between M(II) and M'(III), which depends on the overlap between the metal and oxalate wavefunctions within a single plane. As demonstrated shortly, the spin-orbit interaction is also responsible for the perpendicular magnetic anisotropy of the bimetallic oxalates.

3.2 Hamiltonian

The Hamiltonian for the bimetallic oxalates is assumed to contain three tiers of energies. Because the spin correlations within each 3d ion are strong, we assume that Hund's first rule is obeyed. So as confirmed by measurements [9] of the magnetic susceptibility and Curie constant C, the lowest-energy multiplet is in a high-spin state. The crystal-field potential produced by the six oxygen atoms surrounding each 3d ion is the next largest energy, inducing a splitting of the $L = 2$ multiplet. However, due to the larger spatial extent of their wavefunctions, 4d transition metals such as Ru manifest stronger crystal-field effects which favor a low-spin state [44]. The weakest energies are the AF exchange $J_c \mathbf{S}_2 \cdot \mathbf{S}_3$ between the ions and the spin-orbit coupling $\lambda_i \mathbf{L}_i \cdot \mathbf{S}_i$ ($i = 2$ or 3) on each metal ion. Also included within this lowest energy scale are contributions to the crystal-field potential that violate C_3 symmetry around the M(II) or M'(III) sites.

Surrounding each M(II) and M'(III) ion are six oxygen atoms that form a heavily-compressed octahedron with C_3 symmetry. Based on symmetry grounds, the crystal-field potential can be expressed as the matrix [58]

$$
H^{cf} = \begin{pmatrix}
\gamma & 0 & 0 & \alpha & 0 \\
0 & \gamma' & 0 & 0 & -\alpha \\
0 & 0 & 0 & 0 & 0 \\
\alpha^* & 0 & 0 & \gamma' & 0 \\
0 & -\alpha^* & 0 & 0 & \gamma
\end{pmatrix},
\tag{3.1}
$$

where the five-fold degenerate d-orbitals are used as the basis and a diagonal matrix has been subtracted. The parameters γ, γ' and α depend on the crystalline field at the M(II) and M'(III) sites, which in turn depends on the positions and ionic states of the surrounding oxygens.

Upon diagonalizing H^{cf}, we obtain two sets of degenerate doublets $|\psi_{1,2}\rangle$ and $|\psi_{4,5}\rangle$ and a singlet $|\psi_3\rangle$ [58]. The doublets can be higher or lower in energy than the singlet depending on the crystal-field parameters $\gamma/|\alpha|$ and $\gamma'/|\alpha|$. As shown in Fig.3.1, the singlet has the highest energy below the bottom left curve $\gamma\gamma' = -|\alpha|^2$ and the lowest energy above the top right curve $\gamma\gamma' = |\alpha|^2$. It lies between the two doublets in the central region. In addition, Fig.3.1 displays lines of constant orbital angular momentum for both doublets: $\langle\psi_1|L_z|\psi_1\rangle$ and $\langle\psi_4|L_z|\psi_4\rangle = 1 - \langle\psi_1|L_z|\psi_1\rangle$, both of which only depend on the ratio $(\gamma - \gamma')/|\alpha|$
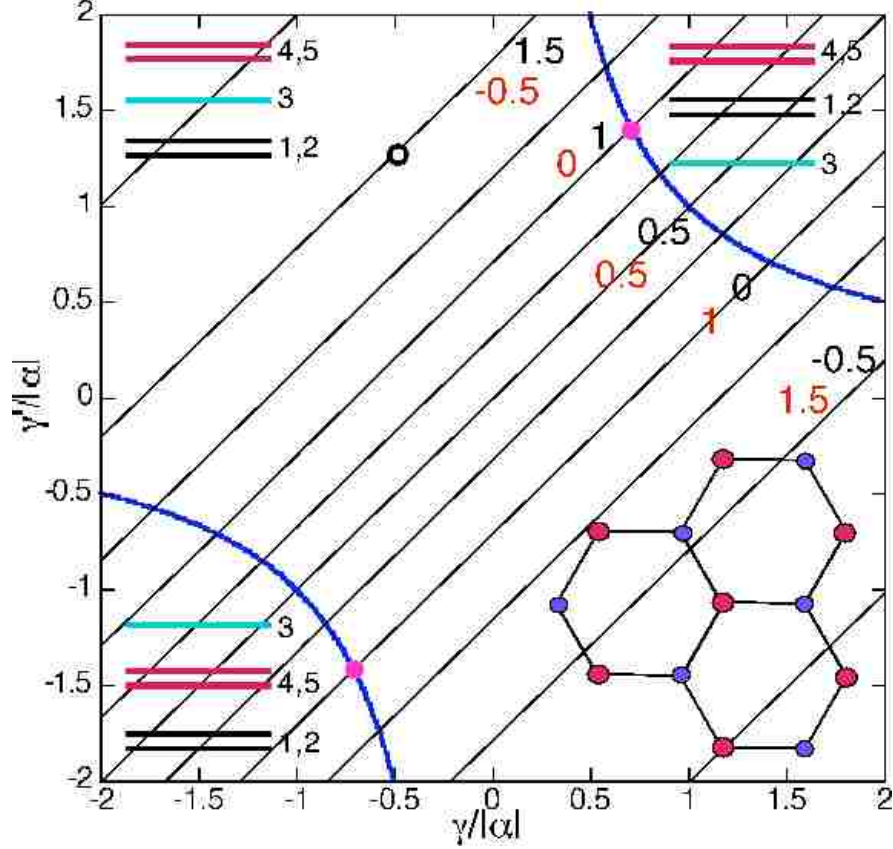
Figure 3.1: (Color online) Variation of the orbital angular momentum $\langle L_z \rangle$ of the two doublets due to the crystal-field at the transition metal ion. The diagonal lines correspond to constant values of $\langle \psi_1 | L_z | \psi_1 \rangle$ (upper-right value) and $\langle \psi_4 | L_z | \psi_4 \rangle$ (lower-left value). Three possible electronic configurations depend on $\gamma/|\alpha|$ and $\gamma'/|\alpha|$. Points of octahedral symmetry are indicated by the two dots, located on the curved boundaries where the singlet and one of the doublets are degenerate. Inset in the lower right is a portion of the open-honeycomb structure of a single bimetallic layer.

[58]. For example, the black circle in Fig.3.1 located at $\gamma/|\alpha| = -0.5$ and $\gamma'/|\alpha| = 1.25$ corresponds to the values $\langle \psi_1 | L_z | \psi_1 \rangle = 1.5$ and $\langle \psi_4 | L_z | \psi_4 \rangle = -0.5$. Due to time-reversal symmetry $\langle \psi_2 | L_z | \psi_2 \rangle = -\langle \psi_1 | L_z | \psi_1 \rangle$ and $\langle \psi_5 | L_z | \psi_5 \rangle = -\langle \psi_4 | L_z | \psi_4 \rangle$ within each doublet. In this electronic configuration it is possible for any combination of M(II) and M'(III) transition metal ions to occupy the low energy doublet, such that the the ground state of these ions in the presence of the crystal field has an uncompensated spin, which is ferrimagnetically coupled to its neighboring spin.

The valence electron configuration, Spin and spin-orbit coupling constants in units of (meV), for M(II) and M(III) transition metal ions are listed in the following table.

33

ion	n	S	λ[meV]
V^{3+}	$3d^2$	1	12.89
Cr^{3+}	$3d^3$	3/2	11.28
V^{2+}	$3d^3$	3/2	6.94
Mn^{3+}	$3d^4$	2	10.91
Fe^{2+}	$3d^6$	2	-12.64
Co^{2+}	$3d^7$	3/2	-21.94
Ni^{2+}	$3d^8$	1	-40.29
Cu^{2+}	$3d^9$	1/2	-102.78
Ru^{3+}	$4d^5$	1/2 (low spin)	116.54

The occupation of the cyrstal-field levels is assumed to follow Hund's first rule and the Aufbau principle with the $L = 2$ levels filling independently [47]. The orbital configurations, spins, and spin-orbit coupling constants λ [48] for the transition metals studied in this paper are summarized in Table I. Using mean-field (MF) theory to treat the exchange interaction $J_c \mathbf{S}_2 \cdot \mathbf{S}_3$, the Hamiltonians on the M(II) and M'(III) sites can be written

$$H_2 = \lambda_2 \mathbf{L}_2 \cdot \mathbf{S}_2 + 3J_c \langle S_{3z} \rangle S_{2z}, \tag{3.2}$$

$$H_3 = \lambda_3 \mathbf{L}_3 \cdot \mathbf{S}_3 + 3J_c \langle S_{2z} \rangle S_{3z}. \tag{3.3}$$

The spin-orbit and exchange interactions are assumed to be much smaller than the crystal-field splittings. Therefore, each Hamiltonian can be restricted to a configuration where one doublet, carrying an average orbital angular momentum L_2 or L_3, is occupied by an odd number of electrons. We can treat the case where each doublet is occupied by an even number of electrons by setting L_2 or L_3 to zero. Of course, $\langle \mathbf{L}_i \rangle$ is only nonzero along the z direction perpendicular to the bimetallic planes.

To demonstrate this approach, consider again the black circle in Fig.1. For a Mn(III) ($3d^4$) ion with these crystal-field parameters, the upper doublet $|\psi_{4,5}\rangle$ would contain a single electron so that $L_3 = 0.5$. But for a Ni(II) ($3d^8$) ion with the same crystal-field parameters, the lower doublet $|\psi_{1,2}\rangle$ would be completely filled by 4 electrons and the upper doublet $|\psi_{4,5}\rangle$ would be half filled by 2 electrons (both in the same spin state) so that $L_2 = 0$. Since the ratios $\gamma/|\alpha|$ and $\gamma'/|\alpha|$ will be different on the M(II) and M'(III) sites, L_2 and L_3 are independent of each other. Because $\langle \psi_{1,2}|L_\pm|\psi_{1,2}\rangle = \langle \psi_{4,5}|L_\pm|\psi_{4,5}\rangle = 0$, the matrix elements

of $\mathbf{L}_2 \cdot \mathbf{S}_2$ and $\mathbf{L}_3 \cdot \mathbf{S}_3$ on the M(II) and M'(III) sites are diagonal with $\langle \psi_i; \sigma_2 | \mathbf{L}_2 \cdot \mathbf{S}_2 | \psi_i; \sigma_2 \rangle = \pm L_2 \sigma_2$ and $\langle \psi_i; \sigma_3 | \mathbf{L}_3 \cdot \mathbf{S}_3 | \psi_i; \sigma_3 \rangle = \pm L_3 \sigma_3$, where σ_2 and σ_3 are the z components of the spin for the M(II) and M(III)' ions. So the eigenvalues of H_2 and H_3 are $\epsilon_{2\sigma_2}^{\pm} = (\pm \lambda_2 L_2 + 3J_c \langle S_{3z} \rangle) \sigma_2$ and $\epsilon_{3\sigma_3}^{\pm} = (\pm \lambda_3 L_3 + 3J_c \langle S_{2z} \rangle) \sigma_3$.

The magnetic moments $M_2(T) = \langle 2S_{2z} + L_{2z} \rangle$ and $M_3(T) = \langle 2S_{3z} + L_{3z} \rangle$ on the M(II) and M'(III) sites are evaluated self-consistently. The average magnetization is then given by $M_{\mathrm{avg}}(T) = (M_2(T) + M_3(T))/2$, where we adopt the convention that $M_3(T) > 0$. The magnetic moment $M_2(T)$ is obtained from the equations

$$\langle S_{2z} \rangle = \frac{2}{Z_2} \sum_{\sigma_2} \sigma_2 e^{-3J_c \langle S_{3z} \rangle \sigma_2 / T} \cosh\left(\lambda_2 \sigma_2 L_2 / T\right), \tag{3.4}$$

$$\langle L_{2z} \rangle = -\frac{2L_2}{Z_2} \sum_{\sigma_2} e^{-3J_c \langle S_{3z} \rangle \sigma_2 / T} \sinh(\lambda_2 \sigma_2 L_2 / T), \tag{3.5}$$

$$Z_2 = 2 \sum_{\sigma_2} e^{-3J_c \langle S_{3z} \rangle \sigma_2 / T} \cosh(\lambda_2 \sigma_2 L_2 / T). \tag{3.6}$$

Of course, $M_3(T)$ is obtained by switching $\lambda_2 \leftrightarrow \lambda_3$, $L_2 \leftrightarrow L_3$, $\sigma_2 \leftrightarrow \sigma_3$, and $\langle S_{2z} \rangle \leftrightarrow \langle S_{3z} \rangle$.

We evaluate the critical temperature T_c by linearizing $\langle S_{2z} \rangle$ and $\langle S_{3z} \rangle$, which results in the expression

$$\left(\frac{T_c}{J_c}\right)^2 = 9 \frac{\sum_{\sigma_2} \sigma_2{}^2 \cosh\left(\frac{\lambda_2 \sigma_2 L_2}{T_c}\right)}{\sum_{\sigma_2} \cosh\left(\frac{\lambda_2 \sigma_2 L_2}{T_c}\right)}$$

$$\times \frac{\sum_{\sigma_3} \sigma_3{}^2 \cosh\left(\frac{\lambda_3 \sigma_3 L_3}{T_c}\right)}{\sum_{\sigma_3} \cosh\left(\frac{\lambda_3 \sigma_3 L_3}{T_c}\right)}. \tag{3.7}$$

This relationship must be solved self-consistently for T_c/J_c, which appears on both sides of Eq.(3.7). In the limit $S_2 = 2$, $S_3 = 5/2$, and $L_3 = 0$, Eq.(3.7) reduces to an earlier result [58] for the Fe(II)Fe(III) bimetallic oxalates. As $T \to T_c$ from below, M_2, M_3, and M_{avg} all vanish within MF theory as $(T_c - T)^{1/2}$. As $T \to 0$, $\langle S_{2z} \rangle \to -S_2$, $\langle S_{3z} \rangle \to S_3$, whereas $M_0 \equiv \lim_{T \to 0} M_{\mathrm{avg}}(T)$ depends on the signs of λ_2 and λ_3. There are four possibilities:

Figure 3.2: (Color online) MC regions for the family M(II)Mn(III) with M = Ni (region 1), Co (region 2), or Fe (region 3) plotted as a function of the average orbital angular momenta L_2 and L_3.

$$
M_0 = \begin{cases}
\left(S_3 - \dfrac{L_3}{2}\right) - \left(S_2 - \dfrac{L_2}{2}\right); & \lambda_2 > 0,\ \lambda_3 > 0 \\[2mm]
\left(S_3 + \dfrac{L_3}{2}\right) - \left(S_2 + \dfrac{L_2}{2}\right); & \lambda_2 < 0,\ \lambda_3 < 0 \\[2mm]
\left(S_3 + \dfrac{L_3}{2}\right) - \left(S_2 - \dfrac{L_2}{2}\right); & \lambda_2 > 0,\ \lambda_3 < 0 \\[2mm]
\left(S_3 - \dfrac{L_3}{2}\right) - \left(S_2 + \dfrac{L_2}{2}\right); & \lambda_2 < 0,\ \lambda_3 > 0.
\end{cases}
$$

3.3   Magnetic Compensation

To find the regions of MC, we use the conditions that either $M_{\mathrm{avg}}(T)$ changes sign near T_{c} or $M_{\mathrm{avg}}(T)$ vanishes at $T = 0$. MC regions are indicated in Fig.3.2 for the family M(II)Mn(III) with M = Ni, Co, or Fe [9], denoted by the labels 1, 2 and 3, respectively. Fig.3.3 shows MC regions 4 and 5 for the family V(II)M'(III) with M' = Cr or V, respectively. The straight lines bordering the MC regions indicate that $M_0 = 0$, which implies that the zero-
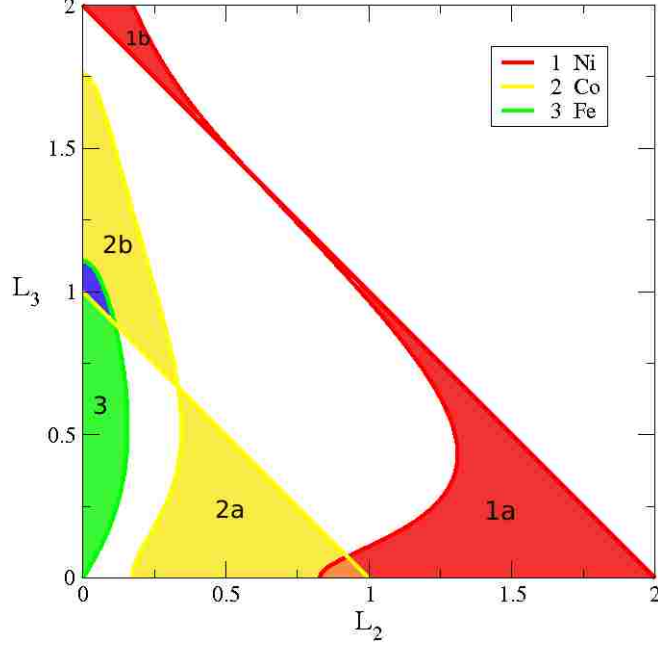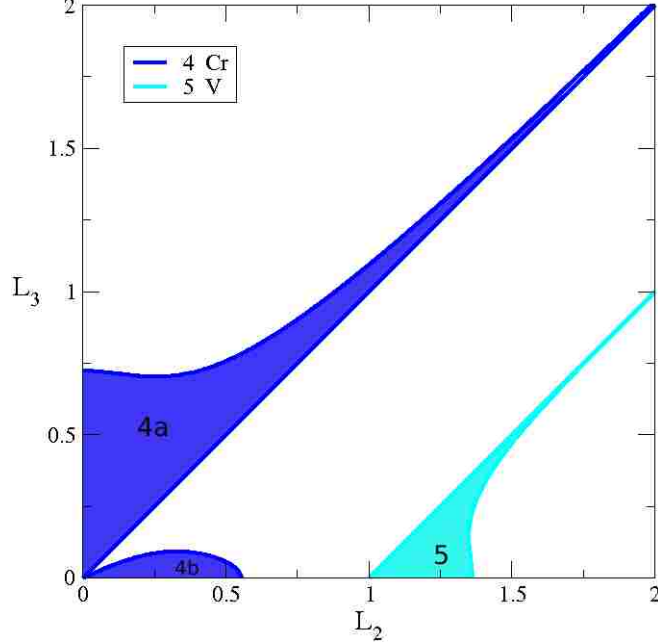
Figure 3.3: (Color online) MC regions for the family V(II)M'(III) with M' = Cr (region 4) or V (region 5) plotted as a function of the average orbital angular momenta L_2 and L_3.

temperature sublattice moments exactly cancel. The MC regions above and below these lines are classified by their saturation values, with $M_0 > 0$ (below) when $|M_3(0)| > |M_2(0)|$ and $M_0 < 0$ (above) when $|M_2(0)| > |M_3(0)|$. Curved boundaries indicate the onset of MC near T_c. Consequently, T_{comp} is small near the straight boundary and approaches T_c near the curved boundary.

In Fig.3.2, the MC regions for Co(II) and Ni(II) have similar shapes but region 2 is shifted with respect to region 1 due to the larger spin $S_2 = 3/2$ for Co(II) compared to $S_2 = 1$ for Ni(II). Since Mn(III) has a spin of $S_3 = 2$ and both Co(II) and Ni(II) have negative values for λ_2 (implying that $\mathbf{L}_2$ and $\mathbf{S}_2$ tend to be parallel), a smaller value of L_2 is required for MC in the Co(II)Mn(III) compound. MC for Ni(II) and Co(II) occurs in regions 1a and 2a with $M_0 > 0$ and in regions 1b and 2b with $M_0 < 0$. In regions 1a and 2a with $M_0 > 0$, the Ni(II) and Co(II) moments are greater than the Mn(III) moment close to T_c; in regions 1b and 2b with $M_0 < 0$, the Mn(III) moment dominates close to T_c. In Fig.3.4, we plot the average magnetization for Co(II)Mn(III) compounds with $L_2 = 0.5$ and $L_3 = 0.0, 0.26$, or 0.52, traversing region 2a. The MC regions are distributed in an odd fashion with respect to the $M_0 = 0$ line because λ_2 and λ_3 have opposite signs. Because both Fe(II) and Mn(III)
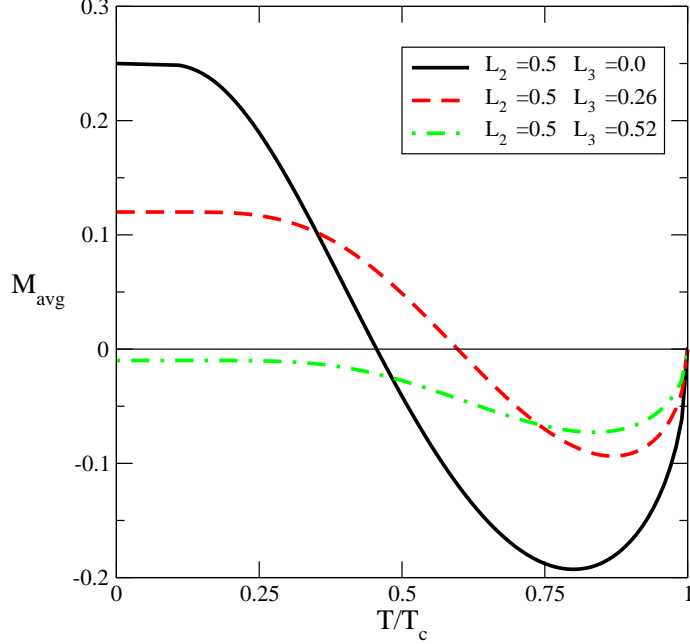
37

Figure 3.4: (Color online) M_{avg} versus T/T_c for Co(II)Mn(III) compounds with $L_2 = 0.5$ and $L_3 = 0.0$ (solid), 0.26 (dashed), and 0.52 (dash-dotted), which traverse region 2a in Fig.3.2.

have the same spin $S_2 = S_3 = 2$, MC region 3 for Fe(II) in Fig.3.2 is restricted to small values of L_2. Since $M_0 < 0$, the Mn(III) moment (with $\lambda_3 > 0$ or antiparallel spin-orbit coupling) is greater than the Fe(II) moment (with $\lambda_2 < 0$ or parallel spin-orbit coupling) close to T_c. For larger values of L_2, the Fe(II) moment would always dominate over the Mn(III) moment.

Our results for the V(II)M'(III) series [55] are displayed in Fig.3.3. Regions 4 and 5 have different shapes because Cr(III) has the same spin $S_3 = 3/2$ as V(II) with $S_2 = 3/2$, while V(III) has the smaller spin $S_3 = 1$. All of these ions have positive values for λ (see Table I), so $\mathbf{S}_i$ and $\mathbf{L}_i$ tend to be antiparallel. For V(II)Cr(III) compounds, the majority of the MC region (4a) occurs when $M_0 < 0$ and $L_3 > L_2$ because $\lambda_3 > \lambda_2$. As a result, the Cr(III) moment is usually larger than the V(II) moment close to T_c. In region 4b with $M_0 > 0$, a bubble of MC exists for small values of L_3, where the V(II) moment dominates the Cr(III) moment near T_c due to its stronger spin-orbit energy $\lambda_2 L_2 S_2 > \lambda_3 L_3 S_3$. Fig.3.5 plots the average magnetization for V(II)Cr(III) compounds with fixed $L_2 = 0.25$ and $L_3 = 0.0, 0.2$, and 0.4, traversing regions 4a and 4b. Notice that MC is absent for $L_3 = 0.2$, which lies between regions 4a and 4b. For V(II)V(III) compounds, MC exists in region 5 only for small values of L_3 with $M_0 > 0$ so that the V(II) moment dominates near T_c.
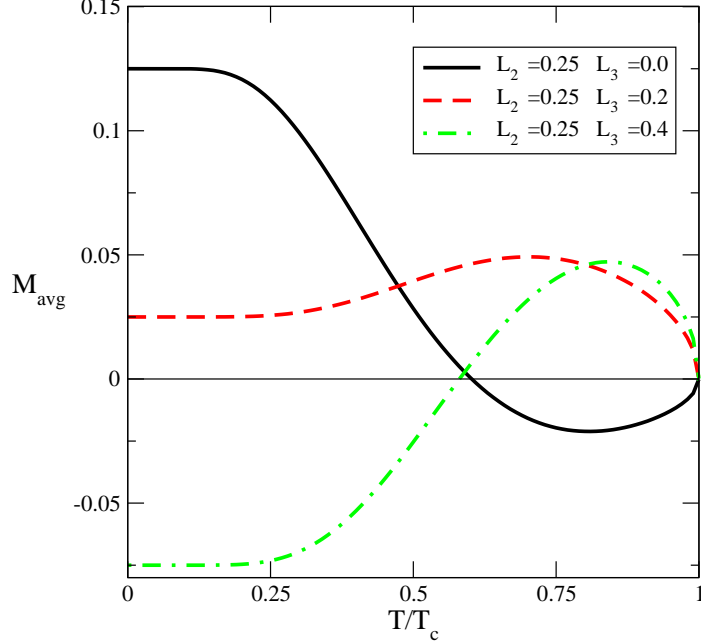
Figure 3.5: (Color online) M_{avg} versus T/T_{c} for V(II)Cr(III) compounds with $L_2 = 0.25$ and $L_3 = 0.0$ (solid), 0.2 (dashed), and 0.4 (dot-dash), which traverse regions 4a and 4b in Fig.3.

We also investigated the series M(II)Ru(III) (M = Fe or Cu) [44]. MC is absent due to the large spin-orbit coupling λ_3 of Ru(III) (see Table I) and the resulting low-spin state $S_3 = 1/2$ induced by the crystal-field potential. For Fe(II)Ru(III) compounds with $S_2 = 2$, the Fe(II) moment is always much larger than the Ru(III) moment despite the large spin-orbit coupling of Ru(III). For Cu(II)Ru(III) compounds, the spins on the two sublattices are identical with $S_2 = S_3 = 1/2$. Because λ_2 and λ_3 have approximately the same magnitudes but opposite signs, the Cu(II) moment remains larger than the Ru(III) moment for all temperatures and for all values of L_2 and L_3. Hence, the magnetic moments of Fe(II) and Cu(II) always dominate in the family M(II)Ru(III).

Generally, MC occurs because the ion with the smaller saturation moment but stronger spin-orbit coupling initially orders more rapidly with decreasing temperature than the ion with the larger saturation moment. As demonstrated by region 3 of Fig.2 near $L_2 = 0$ and by region 4b of Fig.3 near $L_3 = 0$, MC can even occur when $S_2 = S_3$ and with antiparallel spin-orbit coupling ($\lambda_i > 0$) between $\mathbf{S}_i$ and $\mathbf{L}_i$, despite the smaller saturation moment $|2S_i - L_i|$, due to the stronger initial ordering of the spin $\mathbf{S}_i$. Without spin-orbit coupling, the ion with the larger saturation moment would always dominate over the ion with the smaller saturation moment.

The MC regions in Figs.3.2 and 3.3 result from the interplay between S_2, S_3, L_2, L_3, λ_2, and λ_3. When $M_3(T)$ orders more rapidly below M_{avg} but $|M_2(0)| > |M_3(0)|$, MC appears in regions 1b, 2b, 3, and 4a. When $M_2(T)$ orders more rapidly below T_c but $|M_3(0)| > |M_2(0)|$, MC appears in regions 1a, 2a, 4b, and 5. The relative magnitude of λ_2 or λ_3 changes the sizes of the MC regions but not their overall placement: compare the sizes of regions 1a and 1b. By contrast, the placement of the MC regions in Figs.3.2 and 3.3 are primarily determined by S_2, S_3, L_2, and L_3.

Experiments reveal that the deviation in the paramagnetic susceptibility χ from its spin-only value [39, 55, 9] is relatively small. For example, the Curie constant C for a Fe(II)Mn(III) compound is about 30% higher than its spin-only value [9]. This implies that there is a small but nonzero orbital contribution to the magnetic moment [49]. Earlier work [58] indicated that Fe(II)Fe(III) compounds which exhibit MC have values of L_2 just above the threshold of 0.25. Correspondingly, in the families of ferrimagnetic compounds studied here, L_2 and L_3 are probably smaller than 1. We conclude that MC is most likely in the compounds Fe(II)Mn(III), Co(II)Mn(III), and V(II)Cr(III): see regions 2a, 3, 4a, and 4b in Figs.3.2 and 3.3. On the other hand, MC is less likely in the compounds Ni(II)Mn(III) and V(II)V(III), where larger values of L_2 and L_3 are required for MC in regions 1 and 5.

In contrast to the wide range of cations that have been used in the synthesis of Fe(II)Fe(III) bimetallic oxalates [38], only the single cation A = N(n-C$_4$H$_9$)$_4$ has been employed in the synthesis of Fe(II)Mn(III), Co(II)Mn(III), and V(II)Cr(III) compounds [55, 9]. While this cation is associated with MC in the Fe(II)Fe(III) oxalates, there is no guarantee that it will also produce MC in other ferrimagnetic compounds. Therefore, it may be worth investigating Fe(II)Mn(III), Co(II)Mn(III), and V(II)Cr(III) compounds with some of the other cations that produce MC in the Fe(II)Fe(III) oxalates like A = N(n-C$_5$H$_{11}$)$_4$, N(C$_6$H$_5$CH$_2$)(n-C$_4$H$_9$)$_3$, (C$_6$H$_5$)$_3$PNP(C$_6$H$_5$)$_3$, P(n-C$_4$H$_9$)$_4$, CoCp$_2^*$, and FeCp$_2^*$. We are hopeful that at least some of these compounds will yield values of L_2 and L_3 associated with MC in Figs.2 and 3. This paper has investigated the possibility of MC in several families of bimetallic oxalates that exhibit AF interactions between transition metals M(II) and M'(III). For certain cations, MC may be possible within the families of M(II)Mn(III) and V(II)M'(III) bimetallic oxalates but is not possible within the family of M(II)Ru(III) compounds.

Chapter 4

Spin-waves in the Bimetallic Oxalates

4.1   Introduction

Bimetallic oxalates [1] are molecule-based magnets with transition-metal ions M(II) and M'(III)
arranged on an open honeycomb lattice. Performing a Holstein-Primakoff expansion, we ob-
tain the spin-wave spectrum of antiferromagnetically-coupled bimetallic oxalates as a func-
tion of the crystal-field angular momentum L_2 and L_3 on the M(II) and M'(III) sites. Our
results are applied to the Fe(II)Mn(III), Ni(II)Mn(III), and V(II)V(III) bimetallic oxalates,
where the spin-wave gap varies from 0 meV for quenched angular momentum to as high as
15 meV. The presence or absence of magnetic compensation appears to have no effect on the
spin-wave gap.

Bimetallic oxalates have been the source of intense experimental research since they were
first synthesized in 1992 [50]. Within each bimetallic layer, transition-metal ions M(II) and
M'(III) are coupled by oxalate molecules ox = C_2O_4 on the open honeycomb lattice sketched
in Fig. 1 with nearest-neighbor separation $a \approx 5.4$ [51, 52]. The chemical formula for the
bimetallic oxalates is A[M(II)M'(III)(ox)$_3$], where A is an organic cation that separates the
bimetallic layers. For different transition-metal ions, bimetallic oxalates can magnetically or-
der as ferrimagnets, antiferromagnets, or ferromagnets [56, 53, 54, 55] with moments pointing
out-of-the-plane. The cation A lying between the layers does not change the sign of the ex-
change between the M(II) and M'(III) moments but can influence the optical and metallic
properties of the bimetallic oxalates [57]. Recent theoretical calculations [58, 59, 60] used a
simple model to explain many of the magnetic properties of these materials. We now extend
those calculations to evaluate the spin-wave (SW) spectrum of antiferromagnetically-coupled
bimetallic oxalates.

---

[1]This chapter first appeared as: P. Reis and R. Fishman, J. Phys. Condens. Matter, **21**, 016005 (2009).
© J. Phys. Condens. Matter. *From the website of the Journel of Physics: Condensed Matter.*
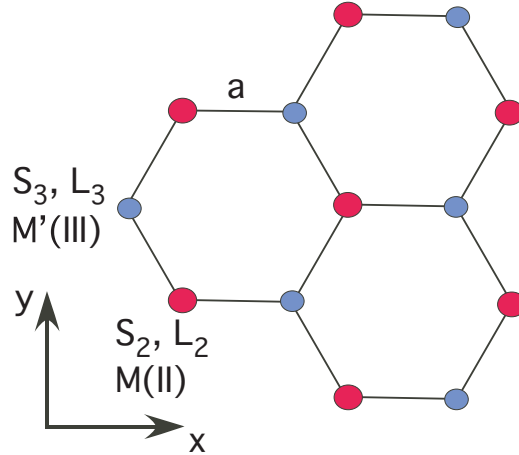
Figure 4.1: (Color online) The open honeycomb lattice showing the alternating M(II) and M'(III) sites. L_2 and L_3 are the crystal-field orbital angular momenta on each site.

Evidence that the cation A is not responsible for the magnetic order of bimetallic oxalates was found in the Fe(II)Fe(III) family, where it was observed that even compounds with well-separated bimetallic layers can have high transition temperatures [53]. Additional support stems from the observation that a radical spin-1/2 cation does not appreciably change the transition temperature and coercive field [52], suggesting that the bimetallic planes are weakly coupled. Earlier work [58, 59] argued that the magnetic properties of the bimetallic oxalates are controlled by the spin-orbit coupling, which can stabilize magnetic order within an isolated layer.

When the exchange interaction between the M(II) and M'(III) moments is antiferromagnetic, it is possible for the sublattice magnetizations to exactly cancel at a compensation temperature T_{comp} below the transition temperature T_{c}. Magnetic compensation (MC) has been observed in the Fe(II)Fe(III) compounds only for certain cations A [53]. Compounds that exhibit MC also possessed the highest values of T_{c} and of the Curie-Weiss constant C [53]. Fishman and Reboredo [58, 59] suggested that MC occurs when the orbital angular momentum of the low-lying crystal-field doublet on the Fe(II) sites exceeds a threshold value. To determine if other bimetallic oxalates could also exhibit MC for certain cations, we included spin-orbit coupling on both the M(II) and M'(III) sites [60]. MC was found to be possible in the M(II)Mn(III) (M = Fe, Co, or Ni) and V(II)M'(III) (M' = Cr or V) families.

Spin-orbit anisotropy is also expected to generate a gap in the SW spectrum. So it is natural to wonder if there is any connection between the presence of MC and the magnitude of the SW gap.

This paper is divided into five sections. Section II discusses the important energy scales in the bimetallic oxalates. Section III briefly explains how we calculate the magnetization of a bimetallic layer including spin-orbit coupling on both sublattices. The SW spectrum of an antiferromagnetically-coupled bimetallic oxalate is derived in Section IV. A conclusion appears in Section V.

4.2   Crystal-Field

Bimetallic oxalates are characterized by three different energy scales. Since the spin correlations within the 3d orbitals are large, Hund's first rule is obeyed [52]. Measurements of the magnetic susceptibility χ, magnetic moment, and Curie constant C of the bimetallic oxalates all confirm that the 3d ions are found in their high-spin states [55, 53]. The C_3-symmetric crystal-field potential produced by the six oxygen atoms surrounding each ion is the next-highest energy level. This potential induces a splitting of the degenerate 3d orbitals. Lowest in energy are the spin-orbit coupling $\lambda_r \mathbf{S}_r \cdot \mathbf{S}_r$ ($r = 2$ or 3) for each metal ion and the antiferromagnetic exchange $J_c \mathbf{S}_2 \cdot \mathbf{S}_3$ mediated by the oxalate molecules.

With matrix elements given by the overlap integrals of the crystal-field potential with the five-fold degenerate d orbitals, the crystal-field Hamiltonian of a single M(II) or M'(III) ion can be written as a 5×5 matrix [58]. Upon diagonalizing this matrix, we obtain two doublet energy levels and one singlet, with eigenvectors $|\psi_{1,2}\rangle$, $|\psi_{4,5}\rangle$, and $|\psi_3\rangle$. The orbital angular momenta of the low-lying doublets on the M(II) and M'(III) sites are given by $\pm L_2$ and $\pm L_3$: $\langle \psi_{1,2} | \mathbf{L} | \psi_{1,2} \rangle = \pm L_r \mathbf{z}$ points in the out-of-the plane or $\mathbf{z}$ direction. Whereas the orbital angular momenta of the doublets are generally nonzero, the orbital angular momentum of the singlet vanishes. If the singlet on the M(II) or M'(III) site lies lowest in energy, we would take L_2 or L_3 equal to zero.

Within the low-energy doublets, the effective Hamiltonian for an antiferromagnetically-coupled bimetallic oxalate can be written

$$H = J_c \sum_{\langle i,j \rangle} \mathbf{S}_{2i} \cdot \mathbf{S}_{3j} + \lambda_2 \sum_i L_{2i}^z S_{2i}^z + \lambda_3 \sum_j L_{3j}^z S_{3j}^z, \tag{4.1}$$

where the $\langle i, j \rangle$ sum runs over all nearest-neighbors, the i sum runs over all M(II) sites, and

the j sum runs over all M'(III) sites. The antiferromagnetic exchange J_c is positive. As discussed above, $L_{2i}^z = \pm L_2$ and $L_{3j}^z = \pm L_3$ can each take two values on the low-energy doublets.

We would like to emphasize that the orbital angular momenta of the low-energy doublets, L_2 and L_3, are modified by the crystal fields. They are not the same as the total angular momenta of the M(II) or M'(III) multiplets before the crystal field is taken into account. For example, in an octahedral crystal field (which can be obtained as a limit of the C_3-symmetric potential [59]), the orbital angular momentum L_3 of the e_g doublet for a Mn(III) ion is quenched although the 3d^4 multiplet had $L = 2$ before it was split by the crystal field.

4.3   Magnetization and Magnetic Compensation

Mean-field (MF) theory is used to treat the exchange interaction $J_c \mathbf{S}_2 \cdot \mathbf{S}_3$ between the antiferromagnetically-coupled M(II) and M'(III) spins. The MF Hamiltonians on M(II) and M'(III) sites are then

$$H_2 = \lambda_2 L_2^z S_2^z + 3J_c S_2^z \langle S_3^z \rangle \tag{4.2}$$

$$H_3 = \lambda_3 L_3^z S_3^z + 3J_c S_3^z \langle S_2^z \rangle. \tag{4.3}$$

Since Eqs.(4.2) and (4.3) are evaluated in the subspace of the M(II) and M'(III) doublets, the energy levels ϵ_r are given by

$$\epsilon_2 = (\pm\lambda_2 L_2 + 3J_c \langle S_3^z \rangle)\sigma_2, \tag{4.4}$$

$$\epsilon_3 = (\pm\lambda_3 L_3 + 3J_c \langle S_2^z \rangle)\sigma_3, \tag{4.5}$$

where $\sigma_2 = S_2, S_2 - 1, \ldots, -S_2$ and $\sigma_3 = S_3, S_3 - 1, \ldots, -S_3$.

Taking $g = 2$ for both M(II) and M'(III) ions and setting $\mu_B = 1$, the magnetic moments on the M(II) and M'(III) sites are $M_2 = \langle 2S_2^z + L_2 \rangle$ and $M_3 = \langle 2S_3^z + L_3 \rangle$, which must be solved self-consistently. The average magnetization is then given by $M_{avg} = (M_2 + M_3)/2$. We adopt the convention that $M_2 > 0$ and $M_3 < 0$. Results in the next section also employ the estimate $J_c = 0.5$ meV obtained from MF theory [58]. Although a recent Monte-Carlo study [61] suggests that J_c is about twice as large, our results are insensitive to the precise value of J_c provided that it is small compared to the spin-orbit coupling.

To characterize the magnetic behavior of a bimetallic layer as a function of the crystal-field angular momenta L_2 and L_3, we make use of the limiting behavior of M_{avg} as $T \to T_c$

and $T \to 0$. In the first case,

$$M_{avg} \sim \sqrt{T_{\mathrm{c}} - T}, \quad T \to T_{\mathrm{c}}. \qquad (4.6)$$

While the square-root behavior is an artifact of MF theory [61], the proportionality factor is a function of L_2 and L_3. As $T \to 0$, the ground-state magnetization depends on the signs of the spin-orbit coupling on the M(II) and M'(III) sites. The spin-orbit coupling constant λ of a $3\mathrm{d}^n$ electronic configuration is negative when the d orbitals are more than half filled ($n > 5$) and positive when they are less than half filled ($n < 5$). So for electronic configurations $3\mathrm{d}^{n_2}$ and $3\mathrm{d}^{n_3}$ on the M(II) and M'(III) sites, the average magnetization at $T = 0$ is given by

$$
\begin{aligned}
M_0 &= \left(S_2 + \frac{L_2}{2} \operatorname{sgn}(n_2 - 5) \right) \\
&\quad - \left(S_3 + \frac{L_3}{2} \operatorname{sgn}(n_3 - 5) \right).
\end{aligned}
\qquad (4.7)
$$

Knowing the sign of M_{avg} near T_{c} together with its sign at $T = 0$ allowed us to determine possible regions of MC in the parameter space of $\{L_2, L_3\}$. For example, when $M_{avg} < 0$ as $T \to T_{\mathrm{c}}$ and $M_0 > 0$ then the sublattice magnetizations change from $|M_3| > |M_2|$ above T_{comp} to $|M_2| > |M_3|$ below T_{comp}.

Regions of MC are presented in Fig. 4.2 for the three compounds M(II)Mn(III) (M = Fe and Ni) and V(II)V(III). The prominent features that distinguish the MC regions are the shapes of their boundaries. For Ni(II)Mn(III) and V(II)V(III), the MC regions have straight diagonal boundaries along which the sublattice magnetizations exactly cancel at $T = 0$. The curved boundaries represent the onset of MC at T_{c}. In all cases, the sublattice with the smaller magnetization at $T = 0$ initially orders faster than the sublattice with the larger magnetization at $T = 0$.

4.4   Spin-Wave Frequencies

We now calculate the SW spectrum for an antiferromagnetically-coupled bimetallic oxalate. Because the spin-orbit interaction $\lambda_3 \mathbf{L}_{2i} \cdot \mathbf{S}_{2i}$ or $\lambda_3 \mathbf{S}_{3j} \cdot \mathbf{S}_{3j}$ can be replaced by $\lambda_2 L_{2i}^z S_{2i}^z$ or $\lambda_3 L_{3j}^z S_{3j}^z$ within the low-energy doublet on the M(II) or M'(III) sites, there are no $L_{2i}^{\pm}$ or $L_{3j}^{\pm}$ terms in the Hamiltonian of Eq.(4.1) that can flip the orbital angular momentum. Therefore, the crystal-field orbital angular momentum acts as an Ising variable and has no intrinsic dynamics. At low temperatures, $\langle L_{2i}^z \rangle$ and $\langle L_{3j}^z \rangle$ are almost fully saturated and can

be replaced by $-\mathrm{sgn}(\lambda_2)L_2$ and $\mathrm{sgn}(\lambda_3)L_3$. So the Hamiltonian at low temperatures can be rewritten

$$H = J_c \sum_{\langle i,j \rangle} \mathbf{S}_{2i} \cdot \mathbf{S}_{3j} - |\lambda_2|L_2 \sum_i S_{2i}^z + |\lambda_3|L_3 \sum_j S_{3j}^z. \qquad (4.8)$$

The absolute values insure that the energy is minimized with the convention that $\langle S_{2i}^z \rangle > 0$ and $\langle S_{3j}^z \rangle < 0$.

A Holstein-Primakoff (HP) expansion about the classical limit is performed for the Hamiltonian in Eq.(4.8). The Heisenberg operators $\mathbf{S}_{2i}$ and $\mathbf{S}_{3j}$ can be transformed to boson creation and destruction operators $a_i^\dagger, b_j^\dagger, a_i$, and b_j provided that $\langle a_i^\dagger a_i \rangle \ll S_2$ and $\langle b_j^\dagger b_j \rangle \ll S_3$. These conditions are satisfied at low temperatures and for large spins S_2 and S_3. To first order in $1/S_i$, the Heisenberg operators take the form

$$S_{2i}^+ = \sqrt{2S_2}a_i, \qquad (4.9)$$

$$S_{3j}^+ = \sqrt{2S_3}b_j^\dagger, \qquad (4.10)$$

$$S_{2i}^- = \sqrt{2S_2}a_i^\dagger, \qquad (4.11)$$

$$S_{3j}^- = \sqrt{2S_3}b_j, \qquad (4.12)$$

$$S_{2i}^z = S_2 - a_i^\dagger a_i, \qquad (4.13)$$

$$S_{3j}^z = -S_3 + b_j^\dagger b_j. \qquad (4.14)$$

Fourier transforming Eqs.(4.9)-(4.14) and substituting the results into Eq.(4.8), we obtain the SW Hamiltonian

$$\begin{aligned}
H^{\mathrm{SW}} &= \sum_{\mathbf{k}} \left\{ 3J_c\sqrt{S_2 S_3}(\gamma_{\mathbf{k}}^* a_{\mathbf{k}}^\dagger b_{\mathbf{k}}^\dagger + \gamma_{\mathbf{k}} a_{\mathbf{k}} b_{\mathbf{k}}) \right. \\
&+ (3J_c S_3 + |\lambda_2|L_2)a_{\mathbf{k}}^\dagger a_{\mathbf{k}} \\
&+ \left. (3J_c S_2 + |\lambda_3|L_3)b_{\mathbf{k}}^\dagger b_{\mathbf{k}} \right\},
\end{aligned} \qquad (4.15)$$

where

$$\gamma_{bfk} = \frac{1}{3}\left\{ e^{ik_x a} + 2e^{-ik_x a/2}\cos\left(\frac{\sqrt{3}}{2}k_y a\right) \right\} \qquad (4.16)$$

is complex with $\gamma_{\mathbf{k}} = \gamma_{-\mathbf{k}}^*$ due to the lack of inversion symmetry. Generally, the error involved in a HP expansion for spins of magnitude S at low temperatures is of order $1/(2S+1)$.

An equations-of-motion technique is used to diagonalize H^{SW}. The vector

$$\underline{u}_{\mathbf{k}} = \begin{pmatrix} a_{\mathbf{k}} \\ b_{\mathbf{k}}^{\dagger} \end{pmatrix}, \tag{4.17}$$

is a solution of

$$i\frac{d\underline{u}_{\mathbf{k}}}{dt} = \left[\underline{u}_{\mathbf{k}}, H^{\mathrm{SW}}\right] = \underline{M}\,\underline{u}_{\mathbf{k}} = \omega(\mathbf{k})\underline{u}_{\mathbf{k}} \tag{4.18}$$

where $\underline{M}$ is a 2×2 matrix. This system of equations requires that $\mathrm{Det}\{\underline{M} - \omega(\mathbf{k})\underline{I}\} = 0$, which yields a pair of solutions for $\omega(\mathbf{k})$. Replacing $\underline{u}_{\mathbf{k}}$ by $\underline{u}_{\mathbf{k}}^{\dagger}$ gives another pair of solutions. The four solutions to the two determinental equations then consist of two equal and opposite pairs. We retain the two positive solutions

$$
\begin{aligned}
\omega^{\pm}(\mathbf{k}) &= \pm\frac{1}{2}\Big(3J_c(S_3 - S_2) + |\lambda_2|L_2 - |\lambda_3|L_3\Big) \\
&+ \frac{1}{2}\Big\{\Big(3J_c(S_2 + S_3) + |\lambda_2|L_2 + |\lambda_3|L_3\Big)^2 \\
&- 36J_c^2|\gamma_{\mathbf{k}}|^2 S_2 S_3\Big\}^{1/2}.
\end{aligned}
\tag{4.19}
$$

When $S_2 = 2$, $S_3 = 5/2$, and $\lambda_3 = 0$, this expression reduces to an earlier one $Fish08$ for the Fe(II)Fe(III) bimetallic oxalates.

At $\mathbf{k} = 0$, $\gamma_{\mathbf{k}} = 1$ and the SW spectrum develops a gap Δ due to the spin-orbit anisotropy. Defining the $\mathbf{k} = 0$ SW frequencies by $\Delta_{\pm} \equiv \omega^{\pm}(\mathbf{k} = 0)$, the SW gap is given by $\Delta = \min(\Delta_+, \Delta_-)$. To better appreciate the behavior of Δ as a function of L_2 and L_3, we have constructed the three contour plots in Fig. 4.2 for Fe(II)Mn(III), Ni(III)Mn(III), and V(II)V(III) compounds. The contours represent constant values of Δ in $\{L_2, L_3\}$ parameter space. It is clear that the SW gap is enhanced as $L_2, L_3 \to 2$. The contours consist of two channels, Δ_+ and Δ_-, running parallel to the L_3 and L_2 axis, respectively. Along the diagonal lines in Fig. 4.2, Δ_+ and Δ_- are equal, which is satisfied when

$$3J_c(S_3 - S_2) + |\lambda_2|L_2 - |\lambda_3|L_3 = 0. \tag{4.20}$$

The slope of this diagonal separator is given by $|\lambda_2/\lambda_3|$ which is noticable in the plot below. The spin-wave gap channels are depend primarily only on one value of orbital angular momentum. As described below.
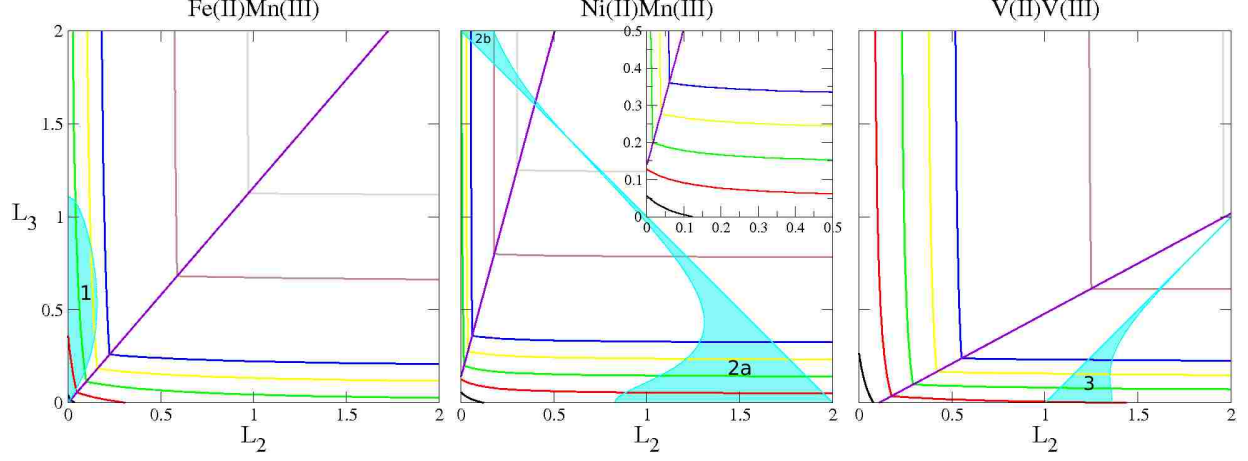
Figure 4.2: (Color online) Contour plots of the SW gap $\Delta(L_2, L_3)$ and the associated MC region for Fe(II)Mn(III), Ni(II)Mn(III), and V(II)V(III). Each plot contains seven contours with $\Delta = 1, 2, 3, 4, 5, 10$ and 15 meV, moving out from the origin as Δ increases. The diagonal separators satisfy the condition $\Delta_+ = \Delta_-$.

The result that the channels Δ_+ and Δ_- are essentially constant or parallel to the L_3 and L_2 axis, respectively, can be understood by expanding the frequencies in powers of J_c/f

$$\Delta_+ \approx |\lambda_2| L_2 + 3 J_c S_3 + \vartheta \left(\frac{J_c^2}{f} \right), \tag{4.21}$$

$$\Delta_- \approx |\lambda_3| L_3 + 3 J_c S_2 + \vartheta \left(\frac{J_c^2}{f} \right). \tag{4.22}$$

where $f \equiv |\lambda_2| L_2 + |\lambda_3| L_3 \gg J_c$. So to lowest order in $J_c/|\lambda_i|$, Δ_+ and Δ_- are given by $|\lambda_2| L_2$ and $|\lambda_3| L_3$, respectively, and are independent of L_3 and L_2. From Eq.(4.19), the SW gap vanishes in the limit $L_2, L_3 \to 0$, independent of the channel Δ_+ or Δ_-.

The contours $\Delta(L_2, L_3)$ of Fig. 4.2 contain seven values ranging from 1 to 15 meV. To illustrate the possible interplay between the SW gap and MC, each figure also indicates the region of MC for that compound. For Fe(II)Mn(III) compounds, the sublattice spins are identical with $S_2 = S_3 = 2$ and the spin-orbit couplings $\lambda_2 = -12.64$ meV and $\lambda_3 = 10.91$ meV are similar in magnitude. Consequently, the first term in Eq.(4.20) vanishes and the separator terminates at the origin with slope $|\lambda_2/\lambda_3| \approx 1.15$. Notice that $\Delta \to 0$ in both the Δ_+ and Δ_- channels as $L_2, L_3 \to 0$. Because $|\lambda_2| \approx |\lambda_3|$, Δ_+ and Δ_- are evenly distributed in $\{L_2, L_3\}$ parameter space. Also notice that the MC region for Fe(II)Mn(III) overlaps the Δ_+ frequencies between 0 and 4 meV.
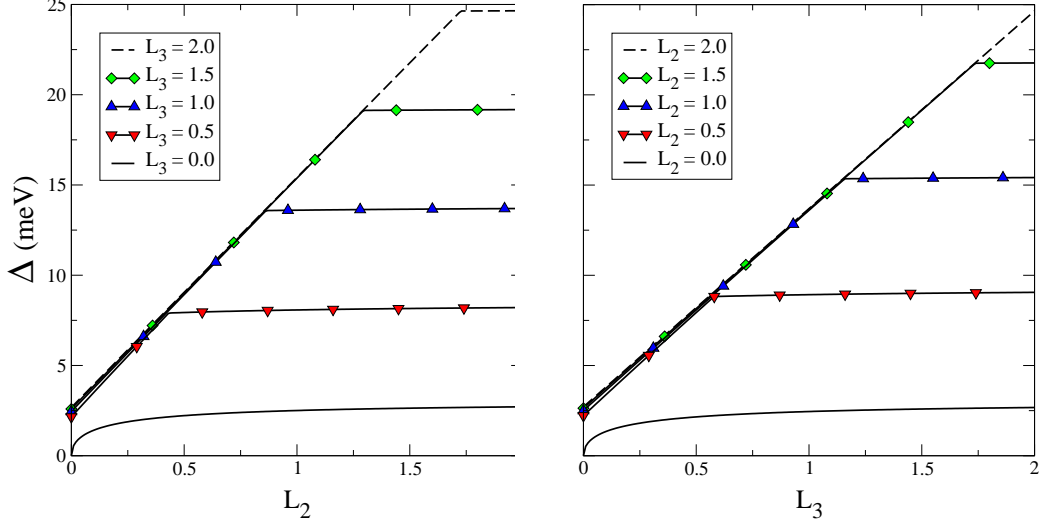
Figure 4.3: (Color online) The SW gap Δ versus L_2 and L_3 for Fe(II)Mn(III). Fixed values of L_2 and L_3 are increased from 0 to 2 in steps of 0.5.

Another view of the contour plot for Fe(II)Mn(III) compounds is provided in Fig. 4.3, which illustrates the behavior of Δ versus L_2 and L_3. Below the kink on the left-hand or right-hand panel, $\Delta = \Delta_+$ or Δ_-; above the kink, $\Delta = \Delta_-$ or Δ_+. These plots clearly reveal the behavior of Eqs.(4.21) and (4.22): above the kinks, Δ_- depends weakly on L_2 and Δ_+ depends weakly on L_3. The lowest curves in Fig. 4.3 indicate that $\Delta \to 0$ in both the Δ_+ and Δ_- channels as L_2 and $L_3 \to 0$.

A contour plot for Ni(II)Mn(III) compounds is shown in the center of Fig. 4.2. Unlike the case for Fe(II)Mn(III) compounds, the sublattice spins are unequal and the magnitude of the spin-orbit couplings are quite different: Ni(II) has $S_2 = 1$ and $|\lambda_2| = 40.29$ meV while Mn(III) has $S_3 = 2$ and $|\lambda_3| = 10.91$ meV. Since the first term on the right-hand side of Eq.(4.20) is nonzero, $\Delta_+ - \Delta_- \to 3J_c(S_3 - S_2) = 1.5$ meV as $L_2, L_3 \to 0$ and the separator has a slope of $|\lambda_2/\lambda_3| = 3.69$. The nonzero intersect of Eq.(4.20) with the L_3 axis allows the Δ_- channel to occupy a greater portion of the $\{L_2, L_3\}$ parameter space. In the inset, we have blown up the region from $L_r = 0$ to 0.5. Notice that the contours $\Delta = 1$ and 2 meV exist only in the Δ_- channel. As the gap energy increases to 3 meV, the Δ_+ channel reappears. The two MC regions for Ni(II)Mn(III) compounds appear in Fig. 4.2. While the SW channel Δ_- traverses region 2a, Δ_+ traverses region 2b.

On the right of Fig. 4.2, the last set of contours is drawn for V(II)V(III) compounds. The V(II) and V(III) ions have spins $S_2 = 3/2$ and $S_3 = 1$, and spin-orbit coupling $\lambda_2 = 6.94$ meV and $\lambda_3 = 12.89$ meV, respectively. So $\Delta_+ - \Delta_- \to 3J_c(S_3 - S_2) = -3/4$ meV as
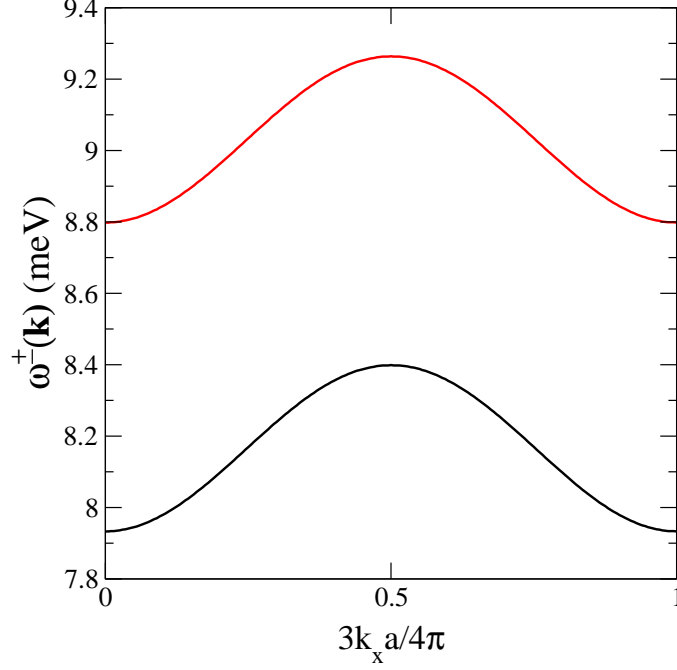
Figure 4.4: (Color online) The SW frequencies $\omega^{\pm}(\mathbf{k})$ versus $k_x a$ for Fe(II)Mn(III) with $L_2 = L_3 = 0.5$ and $k_y = 0$.

$L_2, L_3 \to 0$. Because $S_3 < S_2$, Eq.(4.20) has a nonzero intersect with the L_2 axis. Due to the small slope $|\lambda_2/\lambda_3| = 0.53$ of the separator, the Δ_+ channel occupies the majority of parameter space. Notice that the contours in the Δ_- channel transverse the region of MC for V(II)V(III) compounds.

The SW frequencies $\omega^{\pm}(\mathbf{k})$ are plotted as a function of $k_x a$ in Fig. 4.4 for the compound Fe(II)Mn(III) with $L_2 = L_3 = 0.5$. As can easily be seen from Fig. 1, the wavevector of the ferrimagnetic order on the open honeycomb lattice is given by $\mathbf{Q} = (4\pi/3a)\mathbf{x}$. The maximum in the dispersion along the k_x axis occurs at $k_x = 2\pi/3a$, corresponding to a change of about 0.5 meV relative to the Γ point $\mathbf{k} = 0$. Generally, Eq.(4.19) can be expanded in powers of J_c/f to show that the width of the SW dispersion along the k_x axis is approximately $8J_c^2 S_2 S_3/f$. The difference between the two frequencies $\omega^{\pm}(\mathbf{k})$ is constant as k_x crosses the first Brillouin zone, with a value given by Eq.(4.20). The lower frequency at $\mathbf{k} = 0$ gives the SW gap Δ_-, in agreement with the Fe(II)Mn(III) contours of Fig. 4.2.

We have calculated the SW frequencies for antiferromagnetically-coupled bimetallic ox-alates. Our results for the SW gap were demonstrated by studying the compounds Fe(II)Mn(III), Ni(II)Mn(III), and V(II)V(III) as a function of their associated crystal-field orbital angular momentum L_2 and L_3. The SW gap varied from 0 meV to as high as 15 meV as the angular

momentum L_2 and L_3 increased. There does not seem to be any relationship between the SW gap and the presence or absence of MC. Indeed, the SW gap can achieve its largest value outside regions of MC, as seen particularly in Fig. 2 for the Fe(II)Mn(III) compounds. These results indicate that even compounds that do not exhibit MC may have sizeable SW gaps. However, when the singlet levels on both the M(II) and M'(III) sites lie lowest in energy, then both L_2 and L_3 would vanish and MC would be absent. Since any magnetic anisotropy would then be produced by single-ion anisotropy $D_i \propto \lambda_i^2$, the SW gaps would tend to be much smaller than those predicted here.

Depending on whether Δ_+ or Δ_- is smaller, the SW gap depends primarily on the orbital angular momentum L_2 or L_3 of the M(II) or M'(III) ion, respectively. This surprising result stems from the small value of the exchange interaction J_c compared to the magnitude of the spin-orbit coupling constants λ_i. In addition to the above compounds, we also constructed the contours $\Delta(L_2, L_3)$ for V(II)Cr(III), Co(II)Mn(III), Fe(II)Ru(III), and Cu(III)Ru(III). For the V(II)Cr(III) and Co(II)Mn(III) compounds, we found similar behavior as in Fig. 4.2. On the other hand, Ru(III) compounds with a $4d^5$ electronic configuration displayed an order-of-magnitude higher value of Δ because of the large spin-orbit coupling $\lambda_3 = 116.54$ meV and low-spin $S_3 = 1/2$ state [54].

Hopefully, this paper will inspire future measurements of the SW excitations in the bimetallic oxalates. Although almost all samples are polycrystalline, inelastic neutron-scattering measurements on deuterated materials should be able to measure the SW gap without difficulty.

Chapter 5

Cerium Volume Collapse

5.1   Introduction to the Cerium Volume Collapse

Cerium possesses the fascinating property that at room temperature and pressure 0.8 GPa, it undergoes an isostructural first order phase transition where its volume is reduced by 17% [62, 63], see Fig. 5.1. On both sides of the transition the magnetic properties of Cerium are very different. In the γ phase (large volume) the magnetic order is described by a Curie-Weiss susceptibility, and in the α phase (small volume) the susceptibility is Pauli-like; the former is indicative of localized and the latter itinerant magnetic order.

The driving mechanism leading to the volume collapse and change in magnetic order has been widely disputed, and many physical scenarios have been proposed. One of the first of these was the (metal to insulator) Mott transition, in which the $4f^1$ electrons transition from itinerant in the α phase to localized in the γ phase, due to the strong Coulomb correlations between f electrons [64]. Within the Mott picture, the difference between the kinetic energy of the electrons in the α and γ phases was used to describe the volume change. However the Mott transition does not properly describe the existence of a quasi-particle peak in the α phase as seen in photo-emission spectroscopy measurements[65], or the increase in resistivity below a characteristic temperature in both phases, leading many to believe that a Mott transition does not capture the physics of the volume collapse.

The second explanation of the volume collapse which could explain most of the observed experimental electronic features of experiment was the Kondo model [66]. In this model the interaction between the conduction electrons in the $5d^1$ band and valance electrons located in the $4f^1$ magnetic ions results in very different magnetic properties depending on whether cerium is above or below the Kondo temperature T_K. When cerium is above T_K the magnetic moment of the $4f^1$ electrons are unscreened by the conduction electrons leaving cerium magnetic and in the γ phase. However as the temperature is decreased below T_K, the $4f^1$ electron is compensated by the conduction electrons, quenching the magnetic order,
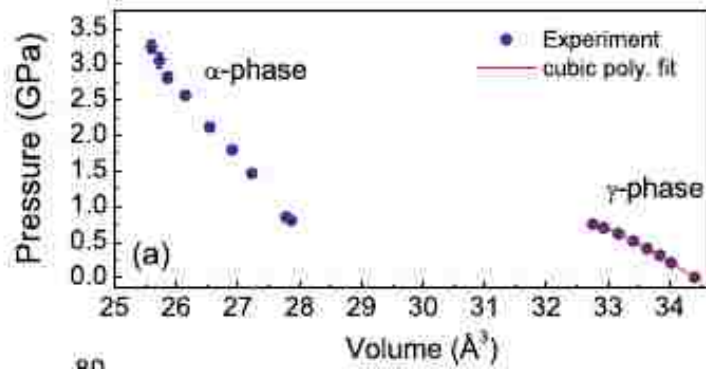
Figure 5.1: The P-V isotherm for the α-γ phase transition in Cerium. At room temperature this transition occurs around 0.8GPa as indicated by the absence of data points at this pressure for volumes between 33 Å^3 and 28 Å^3 , as displayed in reference [63].

and placing cerium in the α phase. The Kondo mechanism explained the disappearance of the magnetic behavior as the transition from $\gamma \to \alpha$ progressed and in addition was in good agreement with the change in electronic entropy verified by experiments at the time, alluding to the fact that the entropy change was independent of phonons.

Recently pulsed neutron measurements have provided an indication that in addition to strong electron correlations phonons do contribute to the volume collapse in cerium[62]. To this end it was shown that the Debye temperature $\Theta_D(V,T)$ was different in the α and γ phases, corresponding to a finite change in entropy across the transition. The volume dependence of $\Theta_D(V,T)$ across the transition has it roots in the different electronic structure of the $4f$ orbital of each phase, where Kondo screening is relevant in the α phase and absent in the γ phase. The difference in electronic structure in both phases results in different inter-atomic forces between the cerium ions, resulting in different frequencies of the phonons in the α and γ phases. Ultimately differences in $\Theta_D(V,T)$ between the phases α and γ provides credence to the role of phonons during the transition.

In our investigation of the cerium volume collapse we will use the periodic Anderson model (PAM), which will allow us to control the effect that pressure plays in fixing the $4f$ level occupation $n_f \simeq 1$ to provide the Kondo physics of the collapse. To better understand the importance of electron-phonon interactions in the volume collapse we couple the phonon to the conduction electrons. We believe this coupling to be the most important electron-phonon interaction during the transition, and not the interaction of the phonons with the $4f^1$ electron, which is in stark contrast to coupling the phonon to the localized f electrons which would inhibit the Kondo physics of the collapse [67].

Extracting information of the $\gamma \to \alpha$ transition of cerium from the PAM with the phonons coupled to the conduction electrons will be done by using dynamical mean field theory (DMFT) [70, 72] with Continuous Time Quantum Monte Carlo (CTQMC) as the impurity solver [71, 73, 92]. Using this method we gain significant insight into the nature of the transition with respect to phonon frequency ω and hybridization V between the $4f^1$ and $5d^1$ orbitals, variables which are critical to our understanding of the volume collapse in cerium. In particular our calculation will allow us to address the question, what electron phonon interactions are important during the transition? Many suggest that the electron phonon interaction during the transition may not be of standard form, but this is speculative, and we wish to rule this in or out. This calculation is highly computational. We calculate the single particle Green's function and the self-energy, among other quantities, to better understand the nature of the $\alpha \to \gamma$ volume collapse of cerium.

The structure of this chapter is as follows. First in section 5.2 we will describe the recent experimental aspects of the cerium volume collapse. In particular we discuss the important photoemission experiments [66], which suggest that the main driving mechanism of the $\alpha \leftrightarrow \gamma$ transition is due to the change in the overlap of the conduction band and the localized f level, which tends to Kondo screen the localized electron in the f level. Additionally in section 5.2 we discuss the more recent experiments which suggest that lattice vibrations are different in the α and γ phases. After identifying that Kondo screening of the inner f electron and lattice vibrations (phonons) are very important constituents in the $\alpha \leftrightarrow \gamma$ transition, the remainder of this chapter will focus on the different models that have been put forth to explain the Kondo effect and phonon correlations. Then we merge the two purposed models in an effort to explain the Cerium $\alpha \leftrightarrow \gamma$ phase transition. Therefore in section section 5.3 we overview the Kondo problem and how its physics leads to a characteristic temperature scale called the Kondo temperature $T_{\mathbf{K}}$. In section 5.4 we demonstrate the equivalence of the Anderson and Kondo models at low temperatures. In section 5.5 the Periodic Anderson model (PAM) is introduced which also exhibits the Kondo effect for temperatures below the coherence temperature $T^\star$, and is the appropriate model to explain the Kondo physics of the $\alpha \leftrightarrow \gamma$ phase transition. Next in section 5.6 we will overview an appropriate phononic model called the Holstein model which we find is relevant to properly describe the electron-phonon interactions in the Cerium volume collapse. Finally in section 5.7 we will describe our effective model for describing the Kondo and phononic correlations in the Cerium volume collapse, which will amount to merging the PAM and the Holstein models.

5.2   Experiments of the Cerium Volume Collapse

Here we will briefly review some of the key experimental aspects of the Cerium Volume Collapse[74]. In particular we will overview three important experiments which show that different electronic and phononic correlations exist in the α and γ phases of Cerium [75, 76]. Early experiments used a number of different spectroscopy measurements such as photoemission (PES), Bremsstrahlung (BIS) and x-ray photoemission (XPS) in an effort to determine the change in the band-structure of cerium as it collapsed; additionally these measurements were used to determine the $4f$ level occupancy, effective hybridization function Δ between the f and conduction electrons and relative position of the f energy level ϵ_f in cerium on both sides of the collapse. Theoretical investigation using the 1/N expansion of the single impurity Anderson model were also used to assist in calculating the spectroscopic parameters concerning the valence of the $4f$ occupancy. The convincing early spectroscopy measurement of Cerium across the collapse using BIS which indicated that the transition in cerium was Kondo driven as a result of the large change in the hybridization between the f and conduction electrons as shown in Figure 5.2. In Figure 5.2 a sharp peak appears in the intensity for energies in the interval $[0, -1.0]eV$ which is reminiscent of a Kondo peak in the small volume phase α. Clearly this peak is absent in the large volume phase γ as indicated in the lower panel; this data was obtained using (BIS) spectroscopy measurements.

More recently experiments have shown that in addition to different electronic structures in the α and γ phases the phononic frequencies in the two phases are also very different [62]. The pioneering work of Jeong using high-pressure, high-resolution neutron and synchrotron x-ray powder diffraction was used to estimate the thermal lattice displacements across the $\alpha \leftrightarrow \gamma$ transition. It was found that a significant change in the lattice displacement occurred as Cerium collapsed. From the thermal lattice displacements it was found that the Debye temperatures Θ_D were different in the α and γ phases, in the γ phase $\Theta_D^{\gamma} = 104(3)K$ and in the α phase $\Theta_D^{\alpha} = 133(3)K$. Clearly these changes indicate that inter-atomic spacing associated with the FCC crystal structure of cerium in the α phase is smaller than the FCC inter-atomic spacing in the γ phase, since $\Theta_D \sim \pi/a$, where a is the lattice spacing between cerium atoms in the direct lattice. From the differences in Θ_D they were able to extract the vibronic entropy difference between the α and γ phase and it was found to be

$$\Delta S_{phonon}^{\gamma-\alpha} \quad \approx \quad 3k_b \ln \frac{\Theta_D^{\alpha}}{\Theta_D^{\gamma}}$$

$$\approx \quad k_B(0.75 \pm 0.15). \tag{5.1}$$

This data clearly indicated that electron-phonon correlations were important in understanding the volume collapse, since this entropy change accounted for half of the total change in entropy. The electronic entropy change across the volume collapse of cerium is calculated as follows. The degeneracy of the f^1 electron in the γ phase is $(2J + 1)$ where $J = 5/2$, and in the α phase the f^1 state is Kondo quenched so the electronic entropy change is given by

$$
\begin{aligned}
\Delta S_{electronic}^{\gamma - \alpha} &= k_B \ln(2J + 1) \\
&= k_B \ln(6) \\
&\approx k_B 1.79
\end{aligned}
\tag{5.2}
$$

Comparing the phonon and electronic entropy changes it is clear that a substantial change in entropy of the Cerium volume collapse results from differences in phonon frequencies in the α and γ phases.

The temperature and pressure of the critical point in the $\alpha - \gamma$ phase diagram has also been located using X-ray diffraction measurements and was located at a pressure of 1.5 ± 0.1 GPa and temperature of 480 ± 10 K [63]. The nature of the $\alpha \leftrightarrow \gamma$ phase transition closely resembles that of a liquid-gas transition in that the slope of the coexistence line separating the α and γ phases increases and ends at a critical point. However there is a distinct difference between the liquid-gas and $\alpha \leftrightarrow \gamma$ phase transition around the critical point. In the case of the liquid gas transition one can go from the liquid phase to the gas phase by increasing the pressure and volume in such a way as to go around the critical point without a discontinuous change in the order parameter characterizing the phase. Owing to the close analogy to the liquid-gas transition in the Cerium volume collapse the critical point was obtained through the analysis of the pressure-volume (P-V) isotherms from x-ray diffraction data. It was found that a free energy functional that included the effects of phonons and Kondo correlations could be used to explain the curvature of the P-V isotherms indicating that phonons are indeed an important ingredient for a successful understanding of the volume collapse in cerium. From this analysis it was clear that the volume collapse was a first order solid to solid transition as a result of the absence of data points in the neutron diffraction data for temperatures below the critical temperature 480 ± 10 K and critical pressure 1.5 ± 0.1 GPa.

The effects of electron-phonon correlations in the volume collapse of cerium has also been resolved through the use of x-ray diffraction measurements of the phonon dispersion of

56
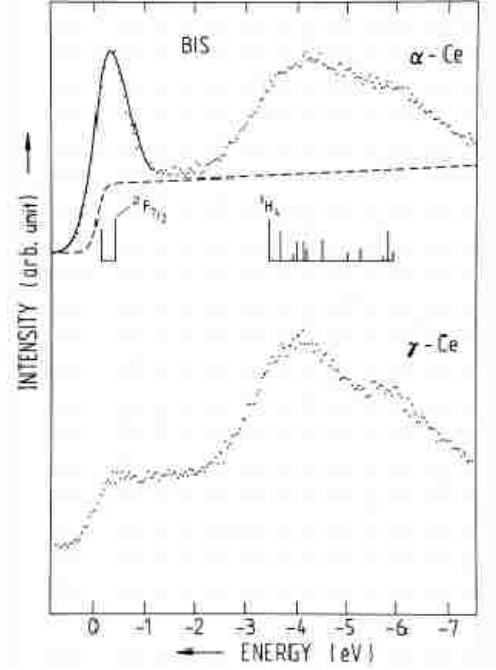
Figure 5.2: Spectroscopy measurement which shows the presence of an enhancement in the spectroscopic intensity of Cerium in the heavily compressed α phase relative to the γ phase. [After Wuilloud (1983)] [74].

cerium in the γ and α phases [69]. In this work it was shown that a large phonon softening in the phonon dispersion occurred in the α phase of cerium around the X point of the reciprocal lattice of the FCC structure in the first Brillouin zone. In addition the Gruneisen parameter was also measured $\gamma_q = -\frac{\partial \ln E(q)}{\partial \ln V}$, which measures the change in the phonon energy with respect to changes in the volume. This measurement was largely negative in the vicinity of the X point, which indicated that increasing electron-phonon correlations were responsible for softening of the phonon dispersion in the α phase of cerium.

5.3 Kondo Physics

It was found experimentally in the 1930's that when a metal with a small amount of magnetic impurities was cooled to very low temperatures its resistivity did not obey the relation

$$\rho(T) = \rho_0 + AT^2 + BT^5, \tag{5.3}$$

where ρ_0 is a residual metallic resistivity, AT^2 is the Fermi-liquid or metallic resistivity, and BT^5 is the resistance due to electron-phonon scattering. Rather it was found that the resistance had a minimum given by

$$\rho(T) \;=\; \rho_0 + AT^2 + BT^5 - C\ln(\frac{k_B T}{W}). \qquad (5.4)$$

The last term of (5.4) was explained in 1964 by Jun Kondo. This minimum occurs at a characteristic temperature $T_\mathbf{K}$ [77]. What Kondo realized was that when the conduction electrons in the host material interacted with the magnetic impurities a spin exchange would occur which would flip the spin of the scattered conduction electron. The Hamiltonian which Kondo used to describe this effect is

$$H \;=\; \sum_{\mathbf{k},\sigma} c^\dagger_{\mathbf{k},\sigma} c_{\mathbf{k},\sigma} + J\mathbf{S} \cdot \mathbf{s} \qquad (5.5)$$

where the first term describes the kinetic energy of the conduction electrons, and the second term describes the interaction between the conduction electron with spin $\mathbf{s}$ and localized electron with spin $\mathbf{S}$. Kondo used second order perturbation theory on this Hamiltonian to show that a resistance minimum would result at a low temperature called the Kondo temperature $T_\mathbf{K}$. Here we briefly explain Kondo's second order calculation and how it results in the resistance minimum of equation (5.4). After writing the interacting term of (5.5) which involves the spin of the impurity $\mathbf{S}$ using second quantization operators $f^\dagger$ and f, the interactions between the localized and conduction electrons has the form,

$$H_{int} \;=\; J \sum_{k,\alpha,\alpha',\beta,\beta'} (\sigma_{\alpha'\alpha} \cdot S_{\beta',\beta}) f^\dagger_{\beta'} c^\dagger_{k,\alpha'} c_{k,\alpha} f_\beta \qquad (5.6)$$

Here the sums are over the momentum $\mathbf{k}$ and spin α, α' of the conduction electrons, and the spin of the impurity ion β, β'. This interaction describes two electrons that interact via their spin degree of freedom. In fact the Kondo effect is the result of the spin degrees of freedom of the conduction and impurity electrons forming a singlet state at low enough temperature $T_\mathbf{K}$, so the interacting Hamiltonian does incorporate the correct spin interactions. Most many-body perturbation calculations start from the Green's function, which describes how one electron propagates from one point in space to another point in space in the presence of a complicated interacting Hamiltonian like (5.6). As the temperature is lowered the probability that an electron can propagate freely without feeling the effects of the spin interaction is

not likely. The Dyson equation is a self-consistent equation that allows us to determine the Green's function

$$
\begin{aligned}
G(k,\omega) &= G_0(k,\omega) + G_0(k,\omega)\Sigma(k,\omega)G(k,\omega) \\
&= \frac{1}{G_0^{-1}(k,\omega) - \Sigma(k,\omega)} \\
&= \frac{1}{\omega - \epsilon_k - \Sigma(k,\omega)}.
\end{aligned} \tag{5.7}
$$

Here we have chosen to write $G(k,\omega)$ in terms of the variables k,ω where ϵ_k is the dispersion of the conduction electrons in the material and $\Sigma(k,\omega)$ is the self-energy of the electron. This is a complex number in which the real part $\mathrm{Re}\Sigma(k,\omega)$ changes the effective energy dispersion of the conduction electrons $\epsilon_k + \mathrm{Re}\Sigma(k,\omega)$. The imaginary part of the self-energy $\mathrm{Im}\Sigma(k,\omega)$ provides information about the life-time τ of the propagating particle, in this case the propagating conduction electron. The resistivity of the material is also related to the scattering life-time through $R \propto \tau^{-1} = \mathrm{Im}\Sigma(k,\omega)$. In order to utilize this result we must decompose $\Sigma(k,\omega)$ into another function called the vertex function $\Gamma(k,\omega)$ which will allow us to examine the nature of the instability in $G(k,\omega)$ [77]. $\Sigma(k,\omega)$ may be written in terms of the vertex function in the following way,

$$
\begin{aligned}
\Sigma(k) &= \sum_{\omega_1,\omega_2} \int d^3p_1 d^3p_2 \Gamma^0(k, p_1 + p_2 - k; p_1, p_2) G_{cc}(p_1) G_{ff}(p_2) G_{ff} \\
&\times \ \Gamma(p_1, p_2; p_1 + p_2 - k, k)
\end{aligned} \tag{5.8}
$$

where we have related $\Sigma(k)$ to the interacting vertex function $\Gamma(p_1, p_2; p_1 + p_2 - k, k)$. The interacting vertex function is directly related to the second order diagram that Jun Kondo showed would diverge at very low temperatures. To show this Γ has to be expanded to second order which we call Γ_2

$$
\begin{aligned}
\Gamma_2 &= J + J \sum_{\alpha',\beta'} (\sigma_{\alpha'\alpha} \cdot S_{\beta',\beta})(\sigma_{\alpha''\alpha} \cdot S_{\beta'',\beta}) J \\
&\times \ \frac{1}{\beta} \sum_{l,\omega_m} G_{0,cc}(l,\omega_n) G_{0,ff}(\omega_m - \omega_n).
\end{aligned} \tag{5.9}
$$

The last term in equation (5.9) is the source of the divergence when the temperature is lowered. We analytically continue the last term $(i\omega_m \to \omega + i\delta)$. Upon performing the

integral over frequency ω and momentum l the integral has the following form,

$$K(0 + i\delta) \approx J\rho\ln(\frac{D}{2\pi T}) \tag{5.10}$$

In the last equation, clearly as the temperature is lowered K diverges, which causes Γ, Σ and consequently the resistance R to diverge at low temperatures. Therefore we find that the resistance diverges at very low temperatures:

$$R \propto J^2[1 + J\rho\ln(\frac{2\pi T}{D})] \tag{5.11}$$

which coincides with equation (5.4) given above for the Kondo portion of the resistivity of a metal which incorporates a dilute concentration of magnetic impurities. We still need to connect this divergence to the Kondo Temperature $T_{\mathbf{K}}$. It turns out that we can sum the vertex function which only incorporates the singular term $K(i\omega_m)$ by performing a power series expansion in the form of

$$\Gamma(i\omega_m) = \frac{J}{1 + 2K(i\omega_m)} \tag{5.12}$$

Once again to obtain meaningful results we must analytically continue the vertex function in (5.12)

$$\Gamma(0 + i\delta) = \frac{J}{1 + 2K(0 + i\delta)} \tag{5.13}$$

which is singular when the denominator of (5.13) is zero which is true when any of the following conditions are upheld

$$0 = 1 + 2K(0 + i\delta)$$
$$\text{or}$$
$$1 = 2|J|\rho\ln(\frac{D}{2k_B T})$$
$$\text{or}$$
$$T_{\mathbf{K}} = \frac{D}{2k_B}e^{-\frac{1}{2|J|\rho}}. \tag{5.14}$$

The singularity in the vertex function $\Gamma(0 + i\delta)$ is the result of spin-flip correlations building up between the conduction and localized electrons. At the Kondo temperature $T_{\mathbf{K}}$, the local spins form bound states with the conduction electrons which is called a Kondo

60
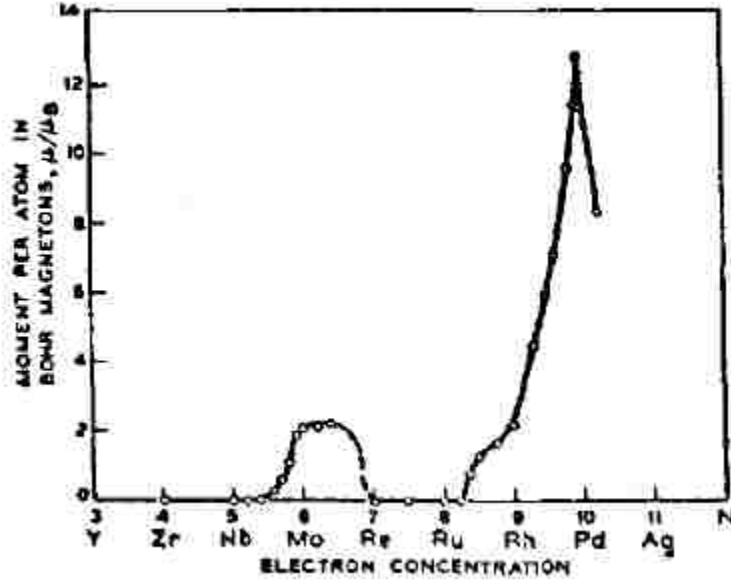
Figure 5.3: Small concentrations of Fe are dissolved into different transition metals as indicated on the horizontal axis. As the electron concentration of the transition metal ions increases a magnetic moment appears. This phenomenon was explained through the use of the Single Impurity Anderson Model (SIAM). Changes in electron concentration were directly related to the model by changes in the position and width of the impurity level. [After Clogston (1962)] [80].

singlet state since the conduction and localized electrons form an anti-ferromagnetic spin singlet state with coupling constant J. It has been observed that the net effect of the Kondo spin-exchange interaction is to modify the density-of-states at the Fermi energy E_F by adding a Lorentzian peak

$$D_{T \sim T_{\mathbf{K}}}(E) = D(E) + \frac{c}{\pi} \frac{\gamma}{(E - E_F)^2 + \gamma^2}. \tag{5.15}$$

The Lorentzian is the result of the spin-flip physics of the Kondo problem. This additional density-of-states at E_f drastically changes the transport properties of materials. Next we will discuss more of the microscopic origins of the Kondo problem when we consider the Anderson model, which is a model more appropriate to Cerium than the Kondo model, but nevertheless still incorporates the important physics of the Kondo model.

5.4 Anderson Impurity Problem

The solution to the single impurity Anderson model (SIAM) was found before the solution to the Kondo problem, however at the time it was not clear how the Anderson impurity problem could explain the low temperature resistivity given by equation (5.4) [78]. The explanation of this phenomenon would wait until Schrieffer and Wolff in 1966 closely examined the model at low temperatures [79]. The SIAM was originally established to explain why when magnetic impurities such as Fe are dissolved into various transition metals, they became magnetic (see Fig. 5.3). This indicated that the impurity ion was able to retain its magnetic moment in a nonmagnetic host. The SIAM Hamiltonian is

$$H = \sum_{\mathbf{k},\sigma} \epsilon_{\mathbf{k}} c^{\dagger}_{\mathbf{k},\sigma} c_{\mathbf{k},\sigma} + \epsilon_f \sum_{\sigma} f^{\dagger}_{\sigma} f_{\sigma} + \sum_{\mathbf{k}\sigma} V_{\mathbf{k}} (c^{\dagger}_{\mathbf{k},\sigma} f_{\sigma} + f^{\dagger}_{\sigma} c_{\mathbf{k},\sigma}) + U n^f_{\uparrow} n^f_{\downarrow}. \qquad (5.16)$$

The first term in the SIAM Hamiltonian represents the kinetic energy of the conduction electrons with dispersion $\epsilon_{\mathbf{k}}$, the second term corresponds to the impurity electrons located at the impurity level ϵ_f. The third term represents the hybridization $V_{\mathbf{k}}$ of the conduction and impurity electrons. The last term corresponds to the Coulomb repulsion between two impurity electrons attempting to occupy the impurity site at the same time. This term along with the hybridization $V_{\mathbf{k}}$ were essential ingredients in explaining the magnetic behavior illustrated in Figure 5.3.

In the following we briefly demonstrate the essential properties of the SIAM for $U = 0$ and $U \neq 0$. When $U = 0$ the SIAM can be solved exactly. The quantity of interest is the local Green's function G_{ff} which has the following structure

$$G_{ff}(\omega) = \frac{1}{\omega - \epsilon_f - \Sigma_{ff}(\omega)}, \qquad (5.17)$$

where the self-energy $\Sigma_{ff}(\omega)$ is

$$\begin{aligned}
\Sigma_{ff}(\omega) &= \sum_{\mathbf{k}} \frac{|V_{\mathbf{k}}|^2}{\omega - \epsilon_{\mathbf{k}} + i\eta} \\
&= P \sum_{\mathbf{k}} \frac{|V_{\mathbf{k}}|^2}{\omega - \epsilon_{\mathbf{k}}} - i\pi \sum_{\mathbf{k}} |V_{\mathbf{k}}|^2 \delta(\omega - \epsilon_{\mathbf{k}}) \\
&= \mathrm{Re}\Sigma_{ff}(\omega) + i\mathrm{Im}\Sigma_{ff}(\omega). \qquad (5.18)
\end{aligned}$$

In the last line we identified the real and imaginary parts of $\Sigma_{ff}(\omega)$. It turns out that we can approximate $-\text{Im}\Sigma_{ff}(\omega) = \Delta = \pi|V|^2 D(\epsilon)$, where $D(\epsilon)$ is the conduction band density-of-states. For this model, since $U = 0$, and the Hamiltonian is spin independent, the density of states profile at the impurity level is found to be

$$
\begin{aligned}
\rho_f(\omega) &= -\frac{1}{\pi}\text{Im}G_{ff}(\omega) \\
&= \frac{1}{\pi}\frac{\Delta}{(\omega - \epsilon_f - \text{Re}\Sigma(\omega))^2 + \Delta^2}
\end{aligned}
\tag{5.19}
$$

which is also spin-independent. This result is important for a couple of reasons, first it shows that the density-of-states at the impurity has a width associated width Δ. Since the result is in the form of a Lorentzian, that the impurity electron quasi-particle life-time is given by $\tau = \Delta^{-1}$. In the absence of interactions $U = 0$, $\rho_f(\omega)$ is centered around the localized orbital at ϵ_f, which indicates that the localized electron in the energy level ϵ_f can quantum mechanically tunnel via $V_{\mathbf{k}}$ into the conduction band in the form of a Friedel resonance, see Fig. 5.4. Additionally, since this result is spin-independent $\rho_f^{\uparrow}(\omega) = \rho_f^{\downarrow}(\omega)$, if we calculated the magnetic moment in the z-direction we would find $S_z = \langle n_{\uparrow}^f - n_{\downarrow}^f \rangle = 0$. So for $U = 0$ it is not possible for the impurity to form a moment! So for magnetism to exist we must include electron-electron correlations between spin $\uparrow$ and $\downarrow$ impurity electrons.

When $U \neq 0$ it is possible for the impurity electron in a metal to possess a magnetic moment $S_z = \langle n_{\uparrow}^f - n_{\downarrow}^f \rangle \neq 0$. The formation of the magnetic moment at the impurity is measured by the susceptibility at the impurity. So we look for a divergence in the local magnetic susceptibility $\chi_{ff}(\omega)$ as a function of increasing Coulomb repulsion U. The magnetic susceptibility at the impurity has the form

$$
\chi_{ff}(\omega) = \frac{\Gamma_{ff}(\omega)}{1 - U\Gamma_{ff}(\omega)},
\tag{5.20}
$$

where $\Gamma_{ff}(\omega)$ is given by

$$
\Gamma_{ff}(\omega) = \frac{1}{2\pi}\int_{-\infty}^{+\infty} G_{ff}(\omega + \epsilon)G_{ff}(\epsilon).
\tag{5.21}
$$

Just as in the case of a bulk ferromagnet we now consider the instability of the impurity to occur when the denominator of 5.20 is zero or rather the interaction U times $\Gamma_{ff}(\omega = 0)$ in

the static response case must satisfies

$$U\Gamma_{ff}(0) = 1. \tag{5.22}$$

So the Green's function for $U \neq 0$ in the ferromagnetic state when the spin symmetry is broken requires making the replacement $\epsilon_f \rightarrow \epsilon_f + U\langle n_\sigma^f \rangle \equiv \bar{\epsilon}_{f\sigma}$ in the denominator of the impurity Green's function given in equation (5.17). With this replacement the impurity Green's function becomes spin-dependent in the ferromagnetic state

$$G_{ff,\sigma}(\omega) = \frac{1}{\omega - \overline{\epsilon_f}_\sigma - \Sigma_{ff}(\omega)}. \tag{5.23}$$

Since $G_{ff,\sigma}(\omega)$ is spin-dependent in the ferromagnetic state any other quantity that depends on $G_{ff,\sigma}(\omega)$, for instance the impurity density $\rho_f(\omega)$ in equation 5.19 will also be spin-dependent in the ferromagnetic state

$$\begin{aligned} \rho_{f,\sigma}(\omega) &= -\frac{1}{\pi}\mathrm{Im}G_{ff,\sigma}(\omega) \\ &= \frac{1}{\pi}\frac{\Delta}{(\omega - \overline{\epsilon_f}_\sigma - \mathrm{Re}\Sigma(\omega))^2 + \Delta^2}. \end{aligned} \tag{5.24}$$

Anderson showed that if the ratio $\dfrac{U}{\Delta} > \dfrac{1}{\pi}$ then it was possible for a magnetic moment to exist at the impurity site. When $\dfrac{U}{\Delta} > \dfrac{1}{\pi}$ the resonance given by equation 5.24 splits into two resonances $\rho_{f,\uparrow}(\omega)$ and $\rho_{f,\downarrow}(\omega)$ situated above and below the Fermi energy E_f see Fig. 5.5.

As mentioned in the introduction, Schrieffer and Wolff found in 1966 that the SIAM incorporated the physics of the Kondo Hamiltonian. The SIAM is a much richer model than the Kondo model since it possesses a local moment phase described above. We will now demonstrate that it also incorporates the spin-flip phenomenon of the Kondo model by performing a Schrieffer and Wolff transformation on the SIAM. Schrieffer and Wolff realized that the two spin states of the impurity electron associated with the resonances ($\rho_{f,\uparrow}$ and $\rho_{f,\downarrow}$) are mixed due to the hopping of conduction electrons on and off the local orbital as a result of the hybridization $V_{\mathbf{k}}$. Hence there is a Kondo resonance which occurs in the SIAM for $U \neq 0$ and $\dfrac{U}{\Delta} > \dfrac{1}{\pi}$. They asked the following question, "under what conditions can this hopping quench the localized moment?" To answer this question we perform a canonical transformation in the spirit of Schrieffer and Wolff, on the SIAM in the local moment regime
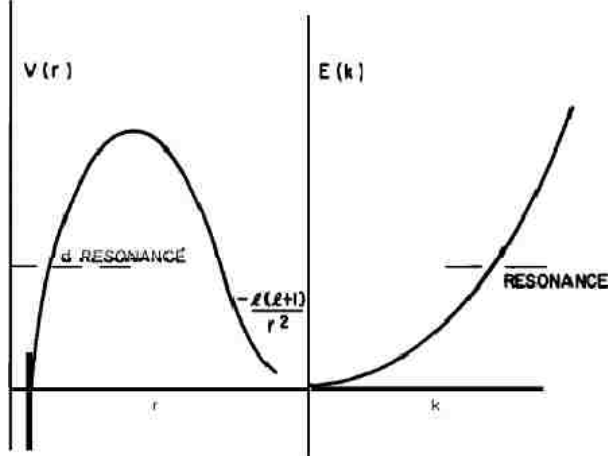
Figure 5.4: Schematic illustration of impurity electron quantum-mechanically tunnel out of a centrifugal barrier into a continuum resulting in a resonance width of $\Delta = \pi|V_{\mathbf{k}}|^2 D(0)$. [After Anderson (1961)] [78].

$\dfrac{U}{\Delta} > \dfrac{1}{\pi}$ to eliminate the linear terms in $V_{\mathbf{k}}$

$$\overline{H} = e^S H e^{-S}. \tag{5.25}$$

In the Hamiltonian of equation (5.16) we include in H_0 all terms that do not contain the hybridization term and in H_1 the hybridization term only. With this understanding the SIAM can be written as

$$H = H_0 + H_1. \tag{5.26}$$

Expanding equation (5.25) in powers of S

$$\overline{H} = H_0 + H_1 - [H_0, S] - [H_1, S] + ... \tag{5.27}$$

we can eliminate H_1, if we choose S in such a way that its commutator with H_0 in 5.27 cancels H_1, that is

$$H_1 = [H_0, S] \tag{5.28}$$

which results in the following transformed equation for $\overline{H}$

$$\overline{H} \;=\; H_0 + \frac{1}{2}[S, H_1] + ... \tag{5.29}$$

plus higher order commutators which are of order $O(V^3)$. Since V is small in the local moment regime we can safely neglect these contributions. After working out the commutator in 5.28 it is found that S has the following form

$$S \;=\; \sum_{\mathbf{k},\sigma} a_{\mathbf{k},\sigma} V_{\mathbf{k}} (f_\sigma^\dagger c_{\mathbf{k},\sigma} - c_{\mathbf{k},\sigma}^\dagger f_\sigma). \tag{5.30}$$

the parameter $a_{\mathbf{k}}$ when evaluated at the Fermi level $\mathbf{k}_F$ the magnetic exchange $J_{\mathbf{k_F}}$ has the following value,

$$J_{\mathbf{k_F}} \;=\; 2\frac{|V|^2 U}{\epsilon_f(\epsilon_f + U)}. \tag{5.31}$$

The commutator in equation (5.29) yields the Kondo interaction between the conduction and localized electrons, so our transformed Hamiltonian reduces to

$$\overline{H} \;=\; H_0 - \frac{1}{2} \sum_{\mathbf{k},\mathbf{k}',\sigma,\sigma'} J_{\mathbf{k}_F} f_\sigma^\dagger c_{\mathbf{k},\sigma} c_{\mathbf{k}',\sigma'}^\dagger f_{\sigma'} \tag{5.32}$$

It is clear by looking at the last term that it is of the form of a spin-flip interaction, a conduction electron $c_{\mathbf{k},\sigma}$ with spin σ interacts with a localized electron $f_{\sigma'}$ which has spin σ' anti-ferromagnetic-ally through the exchange coupling $J_{\mathbf{k}_F} = 2|V|^2 \dfrac{U}{e_f(e_f + U)}$ which flips the spin of each electron to $c_{\mathbf{k},\sigma'}^\dagger$ and $f_\sigma^\dagger$. This type of spin-exchange only involves a transfer of the spin degree of freedom of the electron, the charge degree of freedom isn't transferred through the exchange because of the large Coulomb repulsion between the conduction and impurity electrons. At low temperature just as in the case of the Kondo problem this interaction will diverge at a critical temperature which is the Kondo temperature $T_{\mathbf{K}}$, which is given by, the same formula as in the Kondo problem

$$
\begin{aligned}
T_{\mathbf{K}} \;&=\; \frac{D}{k_B} \exp\Big(-\frac{1}{N(0) J_{\mathbf{k}_F}} \Big) \\
&=\; \frac{D}{k_B} \exp\Big(-\frac{1}{N(0) 2|V|^2 \frac{U}{e_f(e_f + U)}} \Big)
\end{aligned}
\tag{5.33}
$$
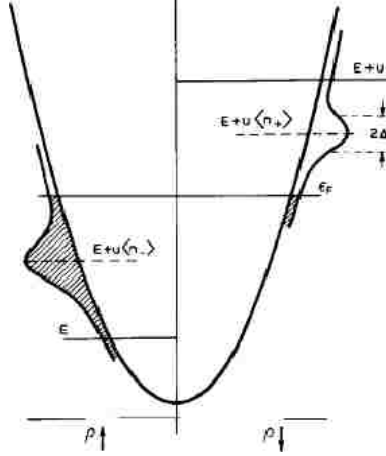
Figure 5.5: In the case that the resonance width Δ divided by U satisfies the condition that $\Delta/U < \pi$ a magnetic solution exists for the SIAM as shown above. This is a plot of the density-of-states showing that the resonances have split into two magnetically polarized solutions with one above the Fermi-level and the other below. [After Anderson (1961)] [78].

where in the last line we were able to link the microscopic parameters of our model to the Kondo temperature.

5.5   Periodic Anderson Model

In this section we extend the single impurity Anderson model to the case where there is a magnetic ion located at every lattice site. This leads us into the physics of heavy fermions and the periodic Anderson model [78]. Examples of materials which fall into the heavy fermion category are the rare earth elements such as the Cerium and Praseodymium. When many Cerium atoms are brought closes together to form a crystal, emergent phenomena occur associated with the occupancy of the 4f level in Cerium, such as the Cerium volume collapse into the α phase. These new behaviors cannot be explained by the SIAM alone.

The $4f^2$ level of Cerium is approximately 10 eV above the $4f^1$ state so there is a strong Coulomb repulsions between electrons, however the $4f^1$ and $4f^0$ levels are pretty close in energy so one would expect that the electron could fluctuate out of the f level into the conduction band. This phenomenon is called mixed-valence-regime of Cerium. Cerium is called a heavy fermion because its resistance follows a formula similar to a metal $\rho(T) = \rho(0) + AT^2$, where A is the contribution from the Fermi-liquid phase, which is proportional to the reduced mass $m^\star$ of the electron. This quantity in heavy fermions is often one-

hundred to a thousand times larger than the mass of the electron. Other experiments which indicate that $m^\star$ is increased in heavy fermion compounds are calculations of the specific heat $C(T) = \gamma T + BT^3$ where γT is the metallic contribution and BT^3 is the phononic contribution to the specific heat. It turns out γ is up to three orders of magnitude larger than in normal metals.

In these examples of heavy fermions the constant A in the resistivity and γ in the specific heat are proportional to the density of states at the Fermi level, $D(E_f)$, so the mysterious increase in these quantities is directly related to an increase in $D(E_f)$. The increase in $D(E_f)$ is the result of a resonance appearing at the Fermi-level, which was shown in the previous section to be related to the Kondo spin-flip interactions.

Another emergent phenomenon in heavy fermion materials is the so called Doniach competition, which is a competition between the Kondo effect and magnetic ordering as a function of hybridization [81]. The magnetic ordering results because the magnetic moment on one impurity site polarizes the conduction electrons which propagates the polarization to another impurity site. This interaction tends to align the impurity magnetic moments antiferromagnetically. The interaction responsible for the magnetic ordering is referred to as RKKY (or Ruderman-Kittel-Kasuya-Yosida) interaction [82]. However the RKKY interaction competes with the Kondo effect, for instance in the dilute limit when the hybridization between the local moment and conduction band is small the system will favor the will antiferromagnetically order through the RKKY interaction since the RKKY ordering energy is $J^2 N(0)$; when the hybridization is large the the system will favor the Kondo effect, since the Kondo energy is $T_{\mathbf{K}} \sim e^{-\frac{1}{JN(0)}}$.

In the following we briefly outline a few of the important aspects of the PAM, following Rice and Ueda's variational Gutzviller calculation [85], and then report on Jarrell's numerical investigations of the model [86]. First we note that the periodic Anderson model has the following Hamiltonian

$$
\begin{aligned}
H &= \sum_{\mathbf{k},\sigma} \epsilon_{\mathbf{k}} c^{\dagger}_{\mathbf{k},\sigma} c_{\mathbf{k},\sigma} + \epsilon_f \sum_{i,\sigma} f^{\dagger}_{i,\sigma} f_{i,\sigma} + \sum_{\mathbf{k},i,\sigma} V_{\mathbf{k}}(c^{\dagger}_{\mathbf{k},\sigma} f_{i,\sigma} + f^{\dagger}_{i,\sigma} c_{\mathbf{k},\sigma}) \\
&+ \sum_i U n^f_{i,\uparrow} n^f_{i,\downarrow}.
\end{aligned}
\tag{5.34}
$$

The PAM has the same structure as the SIAM, the difference is that the PAM contains a sum over lattice sites where the SIAM did not.

Rice and Ueda derived an effective low energy Hamiltonian that describes the basic properties of the PAM at low temperatures and in the Kondo regime. In the Kondo regime

the Coulomb repulsion energy U is large and the filling of the impurity satisfies $n_f \simeq 1$. The low energy effective Hamiltonian they used was the following,

$$H_{eff} = \sum_{\mathbf{k},\sigma} \epsilon_{\mathbf{k}} c^{\dagger}_{\mathbf{k},\sigma} c_{\mathbf{k},\sigma} + \epsilon_f \sum_{i,\sigma} f^{\dagger}_{i,\sigma} f_{i,\sigma} + \sum_{i,\sigma} \overline{V}_{\sigma} (c^{\dagger}_{i,\sigma} f_{i,\sigma} + f^{\dagger}_{i,\sigma} c_{i,\sigma}). \qquad (5.35)$$

Notice that the Hubbard term is absent and the hybridization function was replaced by the renormalized hybridization function $\overline{V}_{\sigma}$ which depends on the occupancy of the f electrons ,

$$\begin{aligned} \overline{V}_{\sigma} &= \sqrt{q_{\sigma}} V \\ &= \sqrt{\frac{1 - n_f}{1 - n_{f,\sigma}}} V. \end{aligned} \qquad (5.36)$$

When $n_f \approx 1$ in the local moment regime the re-normalized hybridization is very small, and it is very difficult for an electron to hop from site to site since U is very large. Nevertheless if $\overline{V}_{\sigma}$ is finite the impurity electrons can hybridize into the conduction band and hybridize back into another impurity site somewhere else in the lattice, so they identify an effective bandwidth associated with the impurity electrons

$$W \approx (1 - n_f) V. \qquad (5.37)$$

Since U is large in the Kondo regime, $n_f \approx 1$, the effective bandwidth for the electrons W narrows. The bandwidth is related to a number of physically interesting properties, for instance the effective mass $m^{\star}$, the coherence temperature $T^{\star}$ which is the temperature when the Kondo scattering becomes coherent. Finally the density of states at the Fermi level can be calculated from the result of band narrowing. The effective mass is found to be related to the Fermi-energy T_F and the characteristic temperature $T^{\star}$ in the following way

$$\frac{m^{\star}}{m} \approx \frac{T_F}{T^{\star}}. \qquad (5.38)$$

The coherence temperature possesses the following form in the Kondo regime for the PAM using Rice and Ueda's variational Gutzviller approach,

$$T^{\star} = W e^{-\frac{1}{2|J|N(0)}}. \qquad (5.39)$$
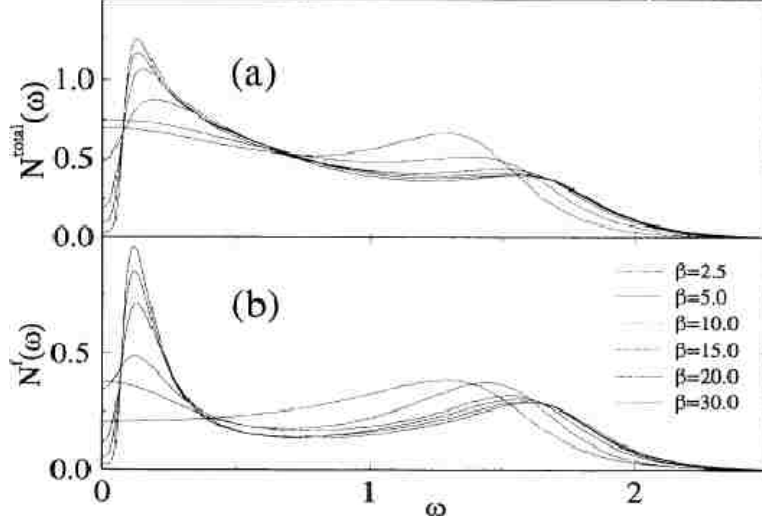
Figure 5.6: (a) Plot of the total density-of-states $N^{total}(\omega)$ (b) and f electron density-of-states $N^f(\omega)$, as the temperature is reduce a sharp peak develops close to $\omega = 0$, indicating that the Kondo single state is forming since $T < T_{\mathbf{K}}$. [After Jarrell (1995)] [86]

The density-of-states at the Fermi level is found to be enhanced indicating that a Kondo resonance develops for temperatures $T < T^{\star}$

$$
\begin{aligned}
\rho_f(E_F) &\approx \rho(E_F)\frac{T_F}{T^*} \\
&\approx \rho(E_F)\frac{m^{\star}}{m}.
\end{aligned}
\tag{5.40}
$$

The increase in $\rho_f(E_F)$ was independently confirmed by Jarrell who used dynamical-mean-field-theory (DMFT) with Hirch-Fye quantum Monte Carlo as the impurity solver. He used the case of the symmetric PAM with the parameters in his Hamiltonian set to $\epsilon_f = -\frac{U}{2}, n_f = 1$ and $n_c = 1$, which required his simulations to be particle-hole symmetric. Shown in Figure 5.6 one notices that a sharp peak (Kondo peak) develops around $\omega = 0$ in the total density-of-states $N^{total}(\omega)$ and the f electron density-of-states $N^f(\omega)$ for $T < T^{\star}$. As the temperature is decreased further below $T^{\star}$ the Kondo peak increases and a pseudogap begins to develop which indicates that the system is transitioning from a metal to an insulator. In the limit that $T \to 0$ one would expect that the pseudogap would become a full gap; Jarrell estimated this gap to be $\Delta \approx 0.5T^{\star}$.

Here we have surveyed most of the important properties of the PAM which are relevant to the Cerium volume collapse. We observed that the PAM in the strong coupling regime

provides an explanation of the increased effective mass $m^\star$ in heavy fermions, and it possesses a Kondo crossover at temperature $T^\star$. Finally we observe that all of the phenomena stated here are directly related to the fact that the localized electrons form an form a narrow band W at half filling $n_f = 1$, the localized electrons cannot hop easily from one site to another because of the large Coulomb repulsion U. As a consequence the localized electrons are associated with a large mass. As U increases the narrow bandwidth W decreases, which implies that the characteristic temperature $T^\star$ also decreases. This implies that increases in U correspond to a decrease in the Kondo resonance close to the Fermi-level (i.e. $T^\star$ decreases). These arguments are in good agreement with Rice and Ueda and also Jarrell's early investigations of the PAM.

The PAM is the model that we have chosen to capture the Kondo-like correlations of the $\alpha \leftrightarrow \gamma$ phase transition of Cerium, however it does not include any of the necessary phononic correlations which have recently been proved to play an important role in the transition. So in the next section we set up a model Hamiltonian called the Holstein model which describes how phonons interact with electrons.

5.6   Holstein Model

Lattice vibrations in the Cerium volume collapse play a crucial role in renormalizing the electronic correlations as Cerium collapses. It has been shown that 50% of the total entropy change is directly related to different phonon frequencies in the α and γ phases, which indicates that the phonon involvement in the collapse of Cerium is very significant. The other half of the total entropy change is the result of different electronic correlations in the α and γ phases. This leads one to believe that the changes in phononic and electronic correlations during the Cerium volume collapse are not independent of each other but in fact influence one another. For this reason we will use a model that incorporates the effect of electron-phonon correlations which has the following form [87, 88]

$$ H \;=\; \sum_{\mathbf{k},\sigma} \epsilon_{\mathbf{k}} c^{\dagger}_{\mathbf{k},\sigma} c_{\mathbf{k},\sigma} + \sum_i \left(\frac{P_i^2}{2M} + \frac{1}{2}k x_i^2 \right) + g \sum_i n_i^c x_i. \tag{5.41} $$

This is the Holstein Hamiltonian. It describes the interaction of electrons with the motion of the ions in the lattice. In this Hamiltonian the first term describes the energy of the conduction elections, the second and third terms correspond to the mobility of the ions which are constrained to move about their equilibrium positions, and the last term is the

electron-ion or electron-phonon interaction, which will be used to describe the cooperative electronic and phononic correlations in Cerium.

The Holstein Hamiltonian has been used extensively to explain phenomena such as conventional superconductivity where close to the Fermi surface interact through an attractive interaction which is cause by lattice vibrations. This interacting mechanism ultimately will lead to a breakdown of the Fermi surface, in which all the electrons reside in a new ground state which is called the superconducting state.

Another effect which the electron-phonon interaction has explained is the Peierls transition [89] which occurs in one-dimensional chains of Polyacetylene, where at half-filling one would expect this material to be metallic, however, due to the strong electron-phonon interactions, dimerization occurs in which Polyacetylene becomes insulating [90]. This transition requires a rearrangement of the unit cell which effectively increases it, which sets up a charge density wave in the system.

Some of the earliest effects of the electron-phonon interactions were to slow down the mobility of the electrons in a material; as a result of Coulomb interaction the electrons would polarize the electronic cloud around the atom which causes a distortion in the phonon field and the electron would essentially drag a cloud of phonons as it propagates through the material. The electron and resulting phonon cloud was called a polaron [91]. When the frequency of the lattice vibrations are small the electron-phonon interaction may tend to favor polaron formation over superconductivity.

As a result the Holstein Hamiltonian is capable of exhibiting most of the phenomena that could arise when electron-phonon interactions in materials are important. Now the interesting question is what physics will emerge when the PAM and Holstein Hamiltonian are merged together? Will it provide an explanation of the $\alpha \leftrightarrow \gamma$ transition in Cerium? We believe that these two models independently contain most of the important phenomena needed to provide a good quantitative explanation of the $\alpha \leftrightarrow \gamma$ transition in Cerium.

5.7 Periodic Anderson-Holstein Model

Here we introduce the Hamiltonian which will be the basis for our investigation of the Cerium volume collapse. As mentioned in the previous sections the volume collapse in Cerium involves changes in electronic and phonic correlations across the $\alpha \leftrightarrow \gamma$ transition;
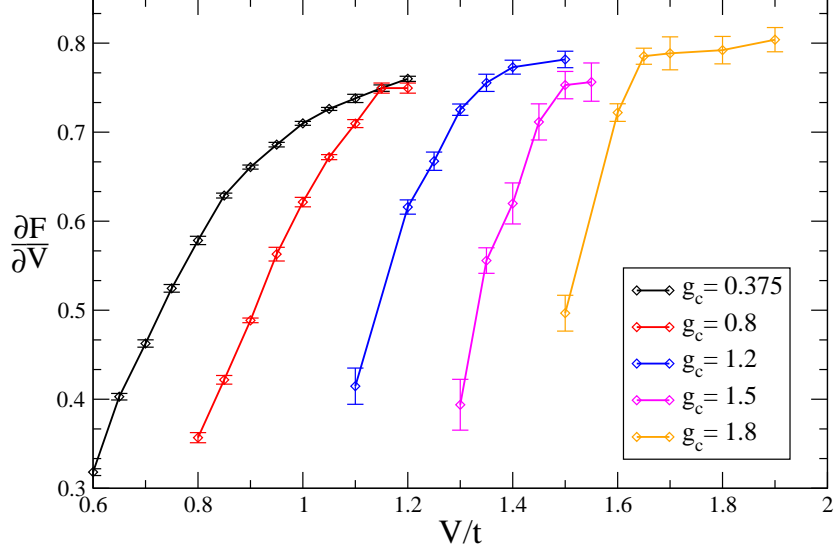
Figure 5.7: Plot of the Kondo order parameter $\frac{\partial F}{\partial V}$ as function of hybridization V, and electron-phonon coupling g_c. As V increases $\frac{\partial F}{\partial V}$ also increase indicating a transition to the Kondo phase where the conduction electrons screen the localized moment. Notice as g_c increases that $\frac{\partial F}{\partial V}$ decreases resulting in an unscreened local moment phase.

our prospective model which we will use to capture these correlations will be the PAM plus Holstein model which has the following form,

$$
\begin{aligned}
H &= \sum_{\mathbf{k},\sigma} \epsilon_{\mathbf{k}} c^{\dagger}_{\mathbf{k},\sigma} c_{\mathbf{k},\sigma} + \epsilon_f \sum_{i,\sigma} f^{\dagger}_{i,\sigma} f_{i,\sigma} + \sum_{\mathbf{k},i,\sigma} V_{\mathbf{k}} (c^{\dagger}_{\mathbf{k},\sigma} f_{i,\sigma} + f^{\dagger}_{i,\sigma} c_{\mathbf{k},\sigma}) \\
&+ \sum_i U n^f_{i,\uparrow} n^f_{i,\downarrow} + \sum_i \left(\frac{P_i^2}{2M} + \frac{1}{2} k x_i^2 \right) + g \sum_i n^c_i x_i.
\end{aligned} \tag{5.42}
$$

The first four terms correspond to the PAM; as mentioned in previous sections this portion of the model will incorporate the Kondo-like correlations of the α phase and include the local-moment physics of the γ phase, where the last three terms plus the first term represent the Holstein model which will introduce the polaronic correlations which are essential for an accurate description of the Cerium volume collapse within our model calculation. What type of physics do we expect to emerge from this Hamiltonian? Clearly there will be a competition between the Kondo effect and phononic correlations. We have just introduced two energy scales into the problem: one is the Kondo energy given by $T_{\mathbf{K}}$ and the other is the phononic deformation energy g. Early in the simulations of (5.42) which we solved using Dynamical-Mean-Field-Theory (DMFT), it was very important to understand which electron-phonon

coupling was the most relevant during the collapse. From our early simulation of (5.42) we found that when the phonon was coupled to the conduction electrons induced a large change in the Kondo order parameter give by

$$\frac{\partial F}{\partial V} = \langle c^\dagger f + f^\dagger c \rangle. \tag{5.43}$$

Figure 5.7 is a plot of the Kondo order parameter, calculated using our model Hamiltonian in (5.42). The parameters of the Hamiltonian were fixed to $U = 4.0t^\star, \omega_0 = 0.01t^\star, \frac{g^2}{2k} = 0.375t^\star, 0.8t^\star, 1.2t^\star, 1.5t^\star, 1.8t^\star$ and the temperature was set to $T = 0.1t^\star$, where the hybridization V was varied as indicated on the horizontal axis. $t^\star$ is the band width of the density of states used in DMFT. Notice as V is increased for all values of $\frac{g^2}{2k}$ that $\frac{\partial F}{\partial V}$ also increases indicating that Kondo screening of the local moment has occurred. Observe as $\frac{g^2}{2k}$ increases that Kondo screening of the local moment is reduced, thus the electronic and phononic correlations are conspiring in such a way as to reduce the Kondo screening which results in a unscreened local moment!

Chapter 6

The Theory of Correlated Systems

6.1 Dynamical Mean Field Theory

The method that we use to extract information from our model Hamiltonian in (5.42) is the Dynamical Mean Field Theory (DMFT) [95]. DMFT allows us to construct all the physical correlation functions required to arrive at an understanding of the physics of our model. The basic idea of DMFT that makes our complicated Hamiltonian (5.42) tractable is that the self energy which arises from the electron-electron and electron-phonon interactions $\Sigma(\mathbf{k}, \omega) = \Sigma(\omega)$ is momentum $\mathbf{k}$ independent, where the temporal correlations ω are preserved. The basic system of equations of DMFT which are solved self consistently are the following. The derivation of these equations can be found in [95]. First we start with $\Sigma(\omega) = 0$ as the initial condition for the self energy, we calculate the local propagator by coarse graining over momentum $\mathbf{k}$ or integrate out over the density of states

$$G_\sigma(i\omega_n) \;=\; \int_{-\infty}^{\infty} d\epsilon \frac{D(\epsilon)}{i\omega_n - \epsilon + \mu - \Sigma_\sigma(i\omega_n)} \tag{6.1}$$

where $D(\epsilon) = \frac{1}{t\sqrt{2\pi}}\exp(-\frac{\epsilon^2}{2t^2})$ is the non-interacting density of conduction electron states in the limit that the dimensionality $d \to \infty$ or the coordination number $Z \to \infty$, and t is the bandwidth. After calculating the local propagator, we calculate the bath function

$$\mathcal{G}_\sigma^{-1}(i\omega_n) \;=\; G_\sigma(i\omega_n)^{-1} + \Sigma_\sigma(i\omega_n) \tag{6.2}$$

which is used as input to recalculate the local propagator using the path-integral representation where all the other degrees of freedom have been integrated out except for the local site,

$$G_\sigma(\tau) \;=\; -\frac{1}{Z}\int \{D\overline{\Psi}_\sigma(\tau')D\Psi_\sigma(\tau')\}[\overline{\Psi}_\sigma(\tau) \otimes \Psi_\sigma(\tau')]\exp(-S_{loc}(\mathcal{G}_\sigma^{-1})) \tag{6.3}$$

here we have defined a two component vector

$$\Psi_\sigma(\tau) \;=\; \left\{ \begin{array}{c} c_\sigma(\tau) \\ f_\sigma(\tau) \end{array} \right\}. \tag{6.4}$$

S_{loc} is the impurity action which includes the local electron-electron correlations of the Hubbard interaction $U n_\uparrow^f n_\downarrow^f$ and the non-local temporal electron-electron phonon correlations $\int_0^\beta \mathrm{d}\tau D_0(\tau) \langle T n_c(\tau) n_c(0) \rangle$ produced by the Holstein coupling, and also includes the bath function $\Delta(i\omega_n)$ representing the hybridization of the local site with the bath. This step is calculated using Continuous Time Quantum Monte Carlo (CTQMC) which is outlined in section 6.2. After calculating the local propagator using CTQMC we can calculate a new self energy from Dyson's equation

$$\Sigma_\sigma(i\omega_n) \;=\; \mathcal{G}_\sigma^{-1}(i\omega_n) - G_\sigma^{-1}(i\omega_n) \tag{6.5}$$

where $\mathcal{G}_\sigma^{-1}(i\omega_n)$ is the bath function. The new value of Σ_σ is used for input into the local propagator (6.1) and the sequence of steps is repeated for another value of $\Sigma_\sigma(i\omega_n)$. Convergence is reached once $\Sigma_\sigma^{n-1}(i\omega_n) \approx \Sigma_\sigma^n(i\omega_n)$ for the n and $n-1$ interations.

6.2   Continuous Time Quantum Monte Carlo

The local propagator $G_\sigma(i\omega_n)$ at the impurity is calculated using Continuous Time Quantum Monte Carlo [96], [97]; I will follow the notation in reference [97]. CTQMC is a Monte Carlo procedure that samples an integral stochastically in accordance with Boltzmann statistics. The integral we would like to sample is the partition function Z which is a multi-dimensional integral in which the integrand depends on the form of the electron-electron interaction in (5.42),

$$\begin{aligned} \frac{Z}{Z_0} \;=\; & \Big\langle T \exp\Big[-\int_0^\beta \mathrm{d}\tau [U(n_\uparrow^f(\tau) - \alpha(s))(n_\downarrow^f(\tau) - \alpha(s)) \\ & + \int_0^\beta \mathrm{d}\tau' D_0(\tau - \tau')(n_c(\tau) - \alpha(s))(n_c(\tau') - \alpha(s))] \Big] \Big\rangle_0. \end{aligned} \tag{6.6}$$

Notice that within DMFT the exponent is independent of lattice site i. The Hubbard interaction is instantaneous in τ since the electron obeys the Pauli exclusion principle, so only two electrons with spin $\uparrow$ and $\downarrow$ can interact via the Hubbard term, however the phonon term is not instantaneous so two electrons can interact at different times τ and τ' with four

different combinations of electronic spin for the two interacting electrons $[\sigma, \sigma'] = [\uparrow, \uparrow]$, $[\uparrow, \downarrow]$, $[\downarrow, \uparrow]$, and $[\downarrow, \downarrow]$. $\alpha(s)$ is an Ising variable that reduces the fermion sign problem, notorious in fermionic QMC simulations, when summed over it leaves the partition function invariant. The sum of the two terms in the exponent in (6.6) can be written as one term,

$$\frac{Z}{Z_0} = \langle T \exp[-\int_0^\beta d\tau \int_0^\beta d\tau' \sum_{[\sigma,\sigma',s=\pm1],b=[0,1]} F_b(\tau - \tau')(n_{b,\sigma}(\tau) - \alpha(s))(n_{b,\sigma'}(\tau') - \alpha(s))]\rangle_0$$

(6.7)

for $b = 0$

$$F_0(\tau - \tau') = \frac{U}{2}\delta(\tau - \tau')\delta_{\sigma,-\sigma'}$$

(6.8)

and $b = 1$

$$F_1(\tau - \tau') = -D_0(\tau - \tau').$$

(6.9)

Expanding the exponential in 6.7 in a power series,

$$\frac{Z}{Z_0} = \sum_{n=0}^{\infty} \frac{(-1)^n}{n!} S^n(\beta, 0)$$

(6.10)

where

$$S^n(\beta, 0) = \int_0^\beta d\tau_1 d\tau_{1'} \sum_{[\sigma_1,\sigma_1',s_1=\pm1],b_1=[0,1]} \dots \int_0^\beta d\tau_n d\tau_{n'} \sum_{[\sigma_n,\sigma_n',s_n=\pm1],b_n=[0,1]}$$
$$\times \quad F(\tau_1 - \tau_{1'})...F(\tau_n - \tau_{n'})$$
$$\times \quad \langle T[(n_{b_1,\sigma_1}(\tau_1) - \alpha(s_1))...(n_{b_n,\sigma_n'}(\tau_n') - \alpha(s_n))]\rangle_0$$

(6.11)

we now define a configuration of order n

$$C_n = [[\sigma_1, \sigma_1', \tau_1, \tau_1', s_1, b_1]$$
$$\dots \quad [\sigma_n, \sigma_n', \tau_n, \tau_n', s_n, b_n]].$$

(6.12)

The sum over n in (6.10) can be replaced by a sum over the configurations C_n making the replacement,

$$
\begin{aligned}
\frac{Z}{Z_0} &= \sum_{n=0}^{\infty} \frac{(-1)^n}{n!} S^n(\beta, 0) \\
&= \sum_{C_n} \det M(C_n)
\end{aligned}
\tag{6.13}
$$

where in this equation we identify,

$$
\begin{aligned}
\sum_{C_n} &= \sum_{n=0}^{\infty} \frac{(-1)^n}{n!} \int_0^{\beta} \mathrm{d}\tau_1 \mathrm{d}\tau_{1'} \sum_{[\sigma_1, \sigma_1', s_1 = \pm 1], b_1 = [0,1]} ... \int_0^{\beta} \mathrm{d}\tau_n \mathrm{d}\tau_{n'} \sum_{[\sigma_n, \sigma_n', s_n = \pm 1], b_n = [0,1]} \\
&\times F(\tau_1 - \tau_{1'}) ... F(\tau_n - \tau_{n'})
\end{aligned}
\tag{6.14}
$$

and

$$
\det M(C_n) = \langle T[(n_{b_1, \sigma_1}(\tau_1) - \alpha(s_1)) ... (n_{b_n, \sigma_n'}(\tau_n') - \alpha(s_n))] \rangle_0.
\tag{6.15}
$$

We do not calculate (6.13) directly but we sample it using the Metropolis algorithm, after the system has equilibrated. Then we can measure the local propagator $G_\sigma(i\omega_n)$ required for the DMFT self-consistency. In order to equilibrate the sum in (6.13), we propose the addition or removal of one configuration $C_k = [\sigma_k, \sigma_k', \tau_k, \tau_k', s_k, b_k]$ from the total configuration C_n using the detailed balance criteria of the Metropolis algorithm. In this way we either promote the system to a configuration C_{n+1} or demote the system to a configuration C_{n-1}. The detailed balance equation is the central equation which allows us to establish the criteria which determines whether the proposed move from the configuration $C_n \rightarrow C_{n+1}$ or $C_n \rightarrow C_{n-1}$ is accepted or rejected. The detailed balance equation for $C_n \rightarrow C_{n+1}$ is

$$
P(C_n) A(C_n \rightarrow C_{n+1}) \det M(C_n) = P(C_{n+1}) A(C_{n+1} \rightarrow C_n) \det M(C_{n+1}).
\tag{6.16}
$$

$P(C_n) = \frac{1}{Z} \exp(-\beta E(C_n))$ is the equilibrium probability (Boltzmann weight) of configuration C_n with energy $E(C_n)$, $A(C_n \rightarrow C_{n+1})$ is the probability of proposing a move from configuration $C_n \rightarrow C_{n+1}$, and $\det M(C_n)$ is the weight of the configuration C_n. Rearranging this equation we can write it as

$$
\exp(-\beta(E(C_{n+1}) - E(C_n))) = \frac{A(C_{n+1} \rightarrow C_n) \det M(C_{n+1})}{A(C_n \rightarrow C_{n+1}) \det M(C_n)}.
\tag{6.17}
$$

78

Generally the Metropolis acceptance criteria is argued as a function of the energy of the new configuration $E(C_{n+1})$ and the energy of the old configuration $E(C_n)$. If $E(C_{n+1}) < E(C_n)$ then the probability of accepting the new configuration C_{n+1} is %100 since this state has a lower energy than the previous configuration C_n. In the case that $E(C_{n+1}) > E(C_n)$, the energy of the new configuration is larger than the old configuration the new state may be accepted as long as its energy is not too much larger than the energy of the old state; to establish this criterion, we pick a random number $R \in [0, 1]$ and the new configuration C_{n+1} is accepted when $\exp(-\beta(E(C_{n+1}) - E(C_n))) > R$ and rejected when $\exp(-\beta(E(C_{n+1}) - E(C_n))) < R$. Using this reasoning the probability of accepting the new configuration C_{n+1} is

$$
\begin{aligned}
P_{C_n \to C_{n+1}} &= \min(1, \exp(-\beta(E(C_{n+1}) - E(C_n)) \\
&= \min(1, \frac{A(C_{n+1} \to C_n)\det M(C_{n+1})}{A(C_n \to C_{n+1})\det M(C_n)}).
\end{aligned}
\tag{6.18}
$$

The probability of accepting the change $C_n \to C_{n-1}$ is

$$
\begin{aligned}
P_{C_n \to C_{n-1}} &= \min(1, \exp(-\beta(E(C_{n-1}) - E(C_n)) \\
&= \min(1, \frac{A(C_{n-1} \to C_n)\det M(C_{n-1})}{A(C_n \to C_{n-1})\det M(C_n)}).
\end{aligned}
\tag{6.19}
$$

After the system has reached equilibrium in the Monte Carlo process we perform our measurements of the correlation functions, in particular we can calculate the local propagator $G_\sigma(i\omega_n)$ essential for convergence of the DMFT cycle. We measure local propagator in imaginary time $G_\sigma(\tau)$ in the following way,

$$
\begin{aligned}
G_\sigma(\tau) &= \langle T c_\sigma^\dagger(\tau) c_\sigma(0) \rangle \\
&= \frac{\sum_{C_n} \det M(C_n) \langle\langle c_\sigma^\dagger(\tau) c_\sigma(0) \rangle\rangle_{C_n}}{\sum_{C_n} \det M(C_n)}.
\end{aligned}
\tag{6.20}
$$

In the last expression $\langle\langle c_\sigma^\dagger(\tau) c_\sigma(0) \rangle\rangle_{C_n}$ is the estimator used to construct the correlation function $G_\sigma(\tau)$. This quantity is calculated as follows,

$$
\langle\langle c_\sigma^\dagger(\tau) c_\sigma(0) \rangle\rangle_{C_n} = \frac{\langle T[(n_{b_1,\sigma_1}(\tau_1) - \alpha(s_1))...(n_{b_n,\sigma_n'}(\tau_n') - \alpha(s_n))]c_\sigma^\dagger(\tau) c_\sigma(0) \rangle_0.}{\langle T[(n_{b_1,\sigma_1}(\tau_1) - \alpha(s_1))...(n_{b_n,\sigma_n'}(\tau_n') - \alpha(s_n))] \rangle_0}
\tag{6.21}
$$

The estimation for the thermal average of the local propagator sampled within Monte Carlo is

$$G_\sigma(\tau) \ = \ \frac{1}{M} \sum_{l=1}^{M} \langle\langle c_\sigma^\dagger(\tau) c_\sigma(0) \rangle\rangle_{C_l}, \tag{6.22}$$

where the sum over l runs over the number of measurements made M, and C_l is the configuration of the system during the lth measurement. Performing the Fourier transform

$$G_\sigma(i\omega_n) = \int_0^\beta d\tau e^{-i\omega_n \tau} G_\sigma(\tau) \tag{6.23}$$

yields the local propagator required for the self-consistency of the DMFT.

6.3 Non-Interacting Green's Function for the PAM

Here we will briefly outline the important steps in calculating the Green's function $G(\mathbf{k}, \omega)$ of the non-interacting Periodic Anderson Model (PAM) starting from the spectral representation at temperature $T = 0$. The spectral representation for $G(\mathbf{k}, \omega)$ is given by

$$G(\mathbf{k}, \omega) \ = \ \int_0^\infty d\epsilon \Big\{ \frac{\rho^+(\mathbf{k}, \epsilon)}{\omega - \epsilon + i\eta} + \frac{\rho^-(\mathbf{k}, \epsilon)}{\omega + \epsilon - i\eta} \Big\}. \tag{6.24}$$

In order to use this equation to calculate $G(\mathbf{k}, \omega)$ requires that we have computed the spectral densities $\rho^+(\mathbf{k}, \epsilon)$ and $\rho^-(\mathbf{k}, \epsilon)$. From an analytic view point we will only focus on calculating ρ^+, since ρ^- is similarly calculated with a change in the the variable $\epsilon \to -\epsilon$. To calculate $\rho^+(\mathbf{k}, \omega)$ requires that we already know $G(\mathbf{k}, \omega)$, from which we can calculate $\rho^+(\mathbf{k}, \omega)$ in the following way since $G(\mathbf{k}, \omega)$ is a discontinuous function of ω,

$$\begin{aligned} \rho^+(\mathbf{k}, \omega) \ &= \ -\frac{1}{\pi} \text{Im}(G(\mathbf{k}, \omega)) \\ &= \ -\frac{1}{2\pi i}(G(\mathbf{k}, \omega) - G^\star(\mathbf{k}, \omega)). \end{aligned} \tag{6.25}$$

This equation for the density of particles $\rho^+(\mathbf{k}, \omega)$ with momentum $\mathbf{k}$ and frequency ω will be finite for $\omega > \mu$. For the non-interacting Anderson model all the elements in $G(\mathbf{k}, \omega)$

posses the same denominator and $G(\mathbf{k}, \omega)$ can be factored in the following way,

$$G(\mathbf{k}, \omega) = \frac{\Delta(\mathbf{k}, \omega + i\eta)}{(\omega - \omega_+ + i\eta)(\omega - \omega_- + i\eta)}. \tag{6.26}$$

The matrix elements of $\Delta(\mathbf{k}, \omega)$ are the following,

$$\Delta_{cc}(\mathbf{k}, \omega) = \omega - \epsilon_f + i\eta$$

$$\Delta_{ff}(\mathbf{k}, \omega) = \omega - \epsilon(\mathbf{k}) + i\eta$$

$$\Delta_{fc}(\mathbf{k}, \omega) = \Delta_{cf}(\mathbf{k}, \omega) = V, \tag{6.27}$$

additionally

$$\omega_{\pm} = \frac{-b \pm \sqrt{b^2 - 4c}}{2} \tag{6.28}$$

with $b = -(\epsilon(\mathbf{k}) + \epsilon_f)$ and $c = \epsilon(\mathbf{k})\epsilon_f - V^2$. Inserting (6.26) into (6.25) and removing the imaginary part in $\Delta(\mathbf{k}, \omega)$ (which is consistent with ρ having poles in the lower half complex plane, since the imaginary part is negligible) allows us to write,

$$\rho^+(\mathbf{k}, \omega) = -\frac{\Delta(\mathbf{k}, \omega)}{2\pi i} \left\{ \frac{1}{(\omega - \omega_+ + i\eta)(\omega - \omega_- + i\eta)} - \frac{1}{(\omega - \omega_+ - i\eta)(\omega - \omega_- - i\eta)} \right\} \tag{6.29}$$

Setting $\overline{\omega}_+ = \omega - \omega_+$ and $\overline{\omega}_- = \omega - \omega_-$ the denominators in 6.29 can be simplified

$$\begin{aligned}
(\omega - \omega_+ - i\eta)(\omega - \omega_- - i\eta) &= (\overline{\omega}_+ - i\eta)(\overline{\omega}_- - i\eta) \\
&= (\overline{\omega}_+ \overline{\omega}_- - \eta^2) - i(\overline{\omega}_+ + \overline{\omega}_-)\eta \\
&= \gamma(\frac{\alpha}{\gamma} - i\eta) \tag{6.30}
\end{aligned}$$

where in the last line we defined $\alpha = \overline{\omega}_+ \overline{\omega}_- - \eta^2$ and $\gamma = \overline{\omega}_+ + \overline{\omega}_-$. Simplifying (6.29) with the above notation and taking the limit as $\eta \to 0^+$ to ensure convergence in the lower half

81

plane gives the following form for $\rho^+(\mathbf{k}, \omega)$,

$$
\begin{aligned}
\rho^+(\mathbf{k}, \omega) &= \lim_{\eta \to 0^+} -\frac{\Delta(\mathbf{k}, \omega)}{2\pi i \gamma} \left\{ \frac{1}{\frac{\alpha}{\gamma} - i\eta} - \frac{1}{\frac{\alpha}{\gamma} + i\eta} \right\} \\
&= \lim_{\eta \to 0^+} -\frac{\Delta(\mathbf{k}, \omega)}{2\pi i \gamma} \left\{ \frac{-2i\eta}{(\frac{\alpha}{\gamma})^2 + \eta^2} \right\} \\
&= \frac{\Delta(\mathbf{k}, \omega)}{\gamma} \delta(\frac{\alpha}{\gamma}).
\end{aligned}
\tag{6.31}
$$

In the last step we invoked the limit $\eta \to 0^+$, therefore α and γ are independent of η. Next we have to evaluate the delta function in the last equation, the delta has the form $\delta(\frac{\alpha}{\gamma}) = \delta(f(\omega))$, which means that we have to find the zeros of $f(\omega)$ and calculate $f'(\omega)$. Clearly the zero's are found by setting $\frac{\alpha}{\gamma} = (\omega - \omega_+)(\omega - \omega_-) = 0$, therefore $\delta(\frac{\alpha}{\gamma})$ is given by

$$
\begin{aligned}
\delta(f(\omega)) &= \sum_i \frac{\delta(\omega - \omega_i)}{|f'(\omega_i)|} \\
&= \delta(\omega - \omega_+) + \delta(\omega - \omega_-)
\end{aligned}
\tag{6.32}
$$

where the sum goes over the roots of $f(\omega)$ and $f'(\omega_+) = f'(\omega_-) = 1$. Therefore the spectral function has the following form

$$
\rho^+(\mathbf{k}, \omega) = \frac{\Delta(\mathbf{k}, \omega)}{\gamma} \left\{ \delta(\omega - \omega_+) + \delta(\omega - \omega_-) \right\}
\tag{6.33}
$$

which corresponds to two spectral lines located at ω_+ and ω_-, as a result of two hybridized bands due to $V \neq 0$. Inserting (6.33) into (6.24) performing the integration yields equation (6.26) for $G(\mathbf{k}, \omega)$. More instructive is performing the integration over ω of (6.33)

$$
\begin{aligned}
G(\mathbf{k}, t) &= -i \int_0^\infty d\omega \rho^+(\mathbf{k}, \omega) e^{-i\omega t} e^{-\eta_+ t} \\
&= -i \int_0^\infty d\omega \frac{\Delta(\mathbf{k}, \omega)}{\gamma} \left\{ \delta(\omega - \omega_+) + \delta(\omega - \omega_-) \right\} e^{-i\omega t} e^{-\eta_+ t} \\
&= -i \left\{ \frac{\Delta(\mathbf{k}, \omega_+)}{\gamma} e^{-i\omega_+ t} + \frac{\Delta(\mathbf{k}, \omega_-)}{\gamma} e^{-i\omega_- t} \right\} e^{-\eta_+ t} \\
&= G(\mathbf{k}, t)_{\omega_+} + G(\mathbf{k}, t)_{\omega_-},
\end{aligned}
\tag{6.34}
$$

which yields $G(\mathbf{k}, t)$. Here we see that the propagation of an electron can occur two ways, either the electron can propagate on the upper branch with energy ω_+ and momentum $\mathbf{k}$ for a time t with a probability amplitude $G(\mathbf{k}, t)_{\omega_+}$, or it propagates on the lower branch

with energy ω_- and momentum $\mathbf{k}$ for a time t with a probability amplitude $G(\mathbf{k}, t)_{\omega_-}$. Here $\eta_+ \Rightarrow \eta_+ \to 0^+$ is used to aid in the convergence of the integral in (6.34).

6.4 Fermi-Liquid Green's Function for the PAM

In this section we will calculate the properties of the PAM with electron-phonon interaction in the conduction band, within the Fermi-liquid (FL) region [100, 101, 102, 103] . Originally the FL concept was developed to describe the low lying excitations in a metal and He^3, where the quasi-particles in both systems obeyed Fermi statistics. The FL concept was developed by L.D. Landau in a phenomenological way in close analogy with the non-interacting electron gas, in which the mass of the quasi-electron was renormalized to $m^\star$ and its life-time in an excited state was not infinity as in the case of a non-interacting electron gas but obeyed the relation $\tau^{-1} = B(\omega - \mu)^2$ due to quasi-particle interactions at very low temperatures, where the interaction between quasi-particles was very strong. Since the interactions between quasi-particle's at low temperatures resulted in quasi-particle excitations close to the Fermi-surface which effectively re-normalized the electron mass $m^\star$ and introduced a lifetime τ, Landau realized that all this information could be included in a theory that closely resembled a non-interacting Fermi-gas in which the Green's function was re-normalized by a factor Z

$$ G(\mathbf{k}, \omega) \;\; = \;\; \frac{Z}{I\omega - ZH_0 + i\Gamma(O(\omega^2))}. \tag{6.35} $$

In the case of the PAM this equation for $G(\mathbf{k}, \omega)$ is a matrix equation, where the re-normalized dispersion relation is ZH_0 and the quasi-particle decay is given by $\Gamma(O(\omega^2)) = B(\omega - \mu)^2$ here B is a 2×2 matrix. Calculating using equation (6.35) within the FL regime $\omega \to 0$ we can neglect the term $\Gamma(O(\omega^2))$ and reincorporate it at the end of the calculation since it is responsible for the quasi-particle life-time. Using (6.35) Landau calculated the spectral function and found it to be for $\omega > \mu$

$$ \rho^+(\mathbf{k}, \omega)_{FL} = Z\delta(I\omega - ZH_0). \tag{6.36} $$

Which states that the quasi-particle spectrum has a resonance at the re-normalized energy given by ZH_0. Later it was found by L.D. Landau, A. Abrikosov, L. Gor'kov, G. M. Eliashberg, L. P. Pitaevskii and J. M. Luttinger that a microscopic description of Landau's FL theory could be established using the diagrammatic techniques of perturbation theory.

For our purpose this equates to linking the phenomenological Green's function of equation (6.35) with the Green's function one would find from an analysis of Dyson's equation from perturbation theory

$$
\begin{aligned}
G(\mathbf{k}, \omega) &= \frac{Z}{I\omega - ZH_0} \\
&= \frac{1}{I\omega - H_0 - \Sigma(\omega)}.
\end{aligned}
\tag{6.37}
$$

Inverting this equation and performing a derivative with respect to ω allows us to calculate the renormalization factor Z from the microscopic self-energy $\Sigma(\omega)$ which is calculated within DMFT,

$$
\begin{aligned}
\frac{\partial G^{-1}}{\partial \omega}(\mathbf{k}, \omega)|_{\omega=0} &= \frac{1}{Z} \\
&= I - \frac{\partial \Sigma(\omega)}{\partial \omega}|_{\omega=0} \\
&= I - \frac{\partial \mathrm{Re}\Sigma(\omega)}{\partial \omega}|_{\omega=0}
\end{aligned}
\tag{6.38}
$$

In the last step we used the fact that in order to relate the microscopic self-energy $\Sigma(\omega)$ which has a real and imaginary part to the phenomenological form of the self-energy given by ZH_0 requires taking the real part of $\mathrm{Re}\Sigma(\omega)|_{\omega=0}$ and evaluating at $\omega = 0$ since ZH_0 is frequency independent. Using the spectral representation for the self energy it is possible to calculate the $\frac{\partial \mathrm{Re}\Sigma(\omega)}{\partial \omega}|_{\omega=0}$ in terms of the imaginary time or Matsubara self-energy $\Sigma_M(i\pi T)$ evaluated at the lowest fermionic Matsubara frequency $\omega_{n=0}$. We will demonstrate the equivalence starting from the spectral representation of $\Sigma(\omega)$ and $\Sigma_M(i\omega_n)$ in the limit that $T \to 0$

$$
\mathrm{Re}\Sigma(\omega) = \int_{-\infty}^{\infty} dx \frac{\frac{1}{\pi}\mathrm{Im}\Sigma(x)}{x - \omega}
\tag{6.39}
$$

and for $\Sigma_M(i\omega_n)$

$$
\Sigma_M(i\omega_n) = \int_{-\infty}^{\infty} dx \frac{\frac{1}{\pi}\mathrm{Im}\Sigma(x)}{x - i\omega_n}.
\tag{6.40}
$$

84

Performing the derivative $\frac{\partial \mathrm{Re}\Sigma(\omega)}{\partial \omega}|_{\omega=0}$ on equation (6.39) gives

$$\frac{\partial \mathrm{Re}\Sigma(\omega)}{\partial \omega}|_{\omega=0} \;=\; \int_{-\infty}^{\infty} dx \frac{\frac{1}{\pi}\mathrm{Im}\Sigma(x)}{x^2}, \tag{6.41}$$

complex conjugating equation (6.40) and taking $\lim_{n \to 0} \mathrm{Im}\Sigma_M(i\omega_n)$ gives

$$\mathrm{Im}\Sigma_M(i\pi T) \;=\; \pi T \int_{-\infty}^{\infty} dx \frac{\frac{1}{\pi}\mathrm{Im}\Sigma(x)}{x^2}. \tag{6.42}$$

Clearly equation (6.41) and (6.42) are equivalent up to a constant πT. Therefore $\frac{\partial \mathrm{Re}\Sigma(\omega)}{\partial \omega}|_{\omega=0}$ can be calculated with the use of the Matsubara self-energy through the relation

$$\frac{\partial \mathrm{Re}\Sigma(\omega)}{\partial \omega}|_{\omega=0} = \frac{\mathrm{Im}\Sigma_M(i\pi T)}{\pi T}. \tag{6.43}$$

Therefore the quasi-particle weight can be calculated from

$$Z \;=\; \left\{ I - \frac{\mathrm{Im}\Sigma_M(i\pi T)}{\pi T} \right\}^{-1}, \tag{6.44}$$

which will be a useful form for calculating Z since no analytic continuation of $\Sigma(\omega)$ is required since $\Sigma_M(i\omega_n)$ is calculated directly from quantum Monte Carlo data.

Starting from the phenomenological form of the Green's function in (6.37) we will show that the spectral function $\rho^+(\mathbf{k},\omega)_{FL}$, as a result of the interactions between quasi-particles, will have excitation energies $\overline{\omega}_\pm$ which are shifted from the non-interacting excitation energies $\omega_\pm$, and re-normalized by a factor Z. The Green's function for the PAM with electron-phonon coupling to the conduction electrons in the FL regime can be written

$$G(\mathbf{k},\omega)_{FL} \;=\; \frac{Z}{I\omega - ZH_0}. \tag{6.45}$$

ZH_0 has the following form,

$$ZH_0 \;=\; \left\{ \begin{array}{cc} Z_{cc} & Z_{cf} \\ Z_{fc} & Z_{ff} \end{array} \right\} \left\{ \begin{array}{cc} \epsilon(\mathbf{k}) & V \\ V & \epsilon_f \end{array} \right\}$$

$$= \left\{ \begin{array}{cc} Z_{cc}\epsilon(\mathbf{k}) + Z_{cf}V & Z_{cc}V + Z_{cf}\epsilon_f \\ Z_{fc}\epsilon(\mathbf{k}) + Z_{ff}V & Z_{ff}\epsilon_f + Z_{fc}V \end{array} \right\}$$

$$= \left\{ \begin{array}{cc} \bar{\epsilon}(\mathbf{k}) & \overline{V}_{cf} \\ \overline{V}_{fc} & \bar{\epsilon}_f \end{array} \right\}. \tag{6.46}$$

Constructing the denominator of (6.45) we find has the following form,

$$I\omega - ZH_0 = \left\{ \begin{array}{cc} \omega - \bar{\epsilon}(\mathbf{k}) & -\overline{V}_{cf} \\ -\overline{V}_{fc} & \omega - \bar{\epsilon}_f \end{array} \right\}. \tag{6.47}$$

Performing the inverse $(I\omega - ZH_0)^{-1}$ we find that the matrix of co-factors has the following form

$$\Delta(\mathbf{k}, \omega)_{FL} = \left\{ \begin{array}{cc} \omega - \bar{\epsilon}_f & \overline{V}_{cf} \\ \overline{V}_{fc} & \omega - \bar{\epsilon}(\mathbf{k}) \end{array} \right\}, \tag{6.48}$$

and $\mathrm{Det}(I\omega - ZH_0)$ can be factor as

$$\mathrm{Det}(I\omega - ZH_0) = (\omega - \bar{\omega}_+)(\omega - \bar{\omega}_-) \tag{6.49}$$

where the eigenfrequencies are given by

$$\bar{\omega}_\pm = \frac{-b \pm \sqrt{b^2 - 4c}}{2} \tag{6.50}$$

with $b = -(\bar{\epsilon}(\mathbf{k}) + \bar{\epsilon}_f)$ and $c = \bar{\epsilon}(\mathbf{k})\bar{\epsilon}_f - \overline{V}_{cf}\overline{V}_{fc}$. Therefore we find $G(\mathbf{k}, \omega)_{FL}$ has the following form after inverting (6.45)

$$G(\mathbf{k}, \omega)_{FL} = \frac{Z\Delta(\mathbf{k}, \omega)_{FL}}{(\omega - \bar{\omega}_+ + i\eta)(\omega - \bar{\omega}_- + i\eta)} \tag{6.51}$$

where we have included $i\eta$ into the denominator to ensure convergence in the lower half plane; in the FL theory this convergence factor is of order $(\omega - \mu)^2$ and gives the attenuation of the quasi-particle. Clearly the form of 6.51 for $G(\mathbf{k}, \omega)_{FL}$ is identical to the non-interacting form given in (6.26) for $G(\mathbf{k}, \omega)$ within the renormalization factor Z. Therefore we can write down the spectral density with this observation,

$$\begin{aligned} \rho^+(\mathbf{k}, \omega)_{FL} &= Z\delta(I\omega - ZH_0) \\ &= \frac{Z\Delta(\mathbf{k}, \omega)_{FL}}{\gamma(\omega)} \Big\{ \delta(\omega - \bar{\omega}_+) + \delta(\omega - \bar{\omega}_-) \Big\} \end{aligned} \tag{6.52}$$

where $\gamma(\omega) = \overline{\omega}_+ - \overline{\omega}_-$. Integrating $\rho^+(\mathbf{k},\omega)_{FL}$ with respect to ω we find,

$$
\begin{aligned}
G(\mathbf{k},t)_{FL} &= -i \int_0^\infty d\omega \rho^+(\mathbf{k},\omega)_{FL} e^{-i\omega t} e^{-\eta} \\
&= -i \int_0^\infty d\omega \frac{Z\Delta(\mathbf{k},\omega)_{FL}}{\gamma(\omega)} \Big\{ \delta(\omega - \overline{\omega}_+) + \delta(\omega - \overline{\omega}_-) \Big\} e^{-i\omega t} e^{-\eta t} \\
&= -iZ \Big\{ \frac{\Delta(\mathbf{k},\overline{\omega}_+)_{FL}}{\gamma(\overline{\omega}_+)} e^{-i\overline{\omega}_+ t} + \frac{\Delta(\mathbf{k},\overline{\omega}_-)_{FL}}{\gamma(\overline{\omega}_-)} e^{-i\overline{\omega}_- t} \Big\} e^{-\eta t} \\
&= G(\mathbf{k},t)_{\overline{\omega}_+} + G(\mathbf{k},t)_{\overline{\omega}_-},
\end{aligned}
\tag{6.53}
$$

which yields the probability amplitude $G(\mathbf{k},t)_{FL}$ in the FL regime. Here we see that the propagation of an electron can occur two ways just as in the non-interacting case, either the electron can propagate on the upper branch with re-normalized energy $\overline{\omega}_+$ and momentum $\mathbf{k}$ for a time t with a renormalized (Z) probability amplitude $G(\mathbf{k},t)_{\overline{\omega}_+}$, or it propagates on the lower branch with a re-normalized energy $\overline{\omega}_-$ and momentum $\mathbf{k}$ for a time t with a re-normalized (Z) probability amplitude $G(\mathbf{k},t)_{\overline{\omega}_-}$. Here $\eta \propto \tau^{-1} \sim (\omega - \mu)^2$ which results in the attenuation of the quasi-particle amplitude $G(\mathbf{k},t)_{FL}$ for times $t > \tau$, which is due to the interactions between quasi-particles in the Fermi-Liquid regime of the PAM with the inclusion of electron-phonon interactions in the conduction band, therefore the exponential decay of $G(\mathbf{k},t)_{FL} \sim e^{-\frac{t}{\tau}}$ for $t > \tau$.

6.5 The Fermi-Liquid Quasiparticle Fraction Z

In this section we extract the quasi-particle fraction Z from the Fermi Liquid Green's function,

$$
\begin{aligned}
G(\mathbf{k},\omega)_{FL} &= \frac{Z}{I\omega - ZH_0} \\
&= \frac{Z\Delta(\mathbf{k},\omega)_{FL}}{(\omega - \overline{\omega}_+(\mathbf{k}) + i\eta)(\omega - \overline{\omega}_-(\mathbf{k}) + i\eta)}
\end{aligned}
\tag{6.54}
$$

where

$$
Z\Delta(\mathbf{k},\omega)_{FL} = \left\{ \begin{matrix} Z_{cc} & Z_{cf} \\ Z_{fc} & Z_{ff} \end{matrix} \right\} \left\{ \begin{matrix} \omega - \overline{\epsilon}_f & \overline{V}_{cf} \\ \overline{V}_{fc} & \omega - \overline{\epsilon}(\mathbf{k}) \end{matrix} \right\},
\tag{6.55}
$$

with

$$\begin{aligned}
\bar{\epsilon}(\mathbf{k}) &= Z_{cc}(\epsilon(\mathbf{k}) - \mu + \Sigma_{cc}^H) + Z_{cf}V \\
\overline{V}_{cf} &= Z_{cc}V + Z_{cf}(\epsilon_f - \mu + \Sigma_{ff}^H) \\
\overline{V}_{fc} &= Z_{fc}(\epsilon(\mathbf{k}) - \mu + \Sigma_{cc}^H) + Z_{ff}V \\
\bar{\epsilon}_f &= Z_{ff}(\epsilon_f - \mu + \Sigma_{ff}^H) + Z_{fc}V.
\end{aligned} \tag{6.56}$$

Here $\Sigma_{cc}^H = -\frac{g^2}{k}n_c$ and $\Sigma_{ff}^H = \frac{U}{2}n_f$ are the constant Hartree terms which change the position of the conduction and impurity levels respectively (see appendix A.3). The renormalization factors Z_{cc}, Z_{ff}, Z_{cf} and Z_{fc} are calculated from the Matsubara self-energies $\Sigma_{cc}(i\pi T), \Sigma_{ff}(i\pi T), \Sigma_{cf}(i\pi T)$ and $\Sigma_{fc}(i\pi T)$ using the Fermi liquid relations,

$$\begin{aligned}
Z^{-1} &= I - \frac{\partial \mathrm{Re}\Sigma(\omega)}{\partial \omega}\Big|_{\omega=0} \\
&= I - \frac{\mathrm{Im}\Sigma(i\pi T)}{\pi T}.
\end{aligned} \tag{6.57}$$

The diagonalized bands have the following form

$$\overline{\omega}_{\pm}(\mathbf{k}) = \frac{1}{2}\Big\{\bar{\epsilon}(\mathbf{k}) + \bar{\epsilon}_f \pm \sqrt{(\bar{\epsilon}(\mathbf{k}) + \bar{\epsilon}_f)^2 - 4(\bar{\epsilon}(\mathbf{k})\bar{\epsilon}_f - \overline{V}_{cf}\overline{V}_{fc})}\Big\}. \tag{6.58}$$

In the following we calculate the quasi-particle renormalization fraction of the upper and lower bands Z_+ and Z_-. This is done by performing the trace of (6.54)

$$\begin{aligned}
\frac{N}{V} &= -\frac{1}{\pi}\mathrm{Im}\mathrm{Tr}(G) \\
&= \int d\mathbf{k}d\omega\{-\frac{1}{\pi}\mathrm{Im}G_{cc}(\mathbf{k},\omega) - \frac{1}{\pi}\mathrm{Im}G_{ff}(\mathbf{k},\omega)\} \\
&= \int d\mathbf{k}\{Z_+(\overline{\omega}_+(\mathbf{k})) + Z_-(\overline{\omega}_-(\mathbf{k}))\} \\
&= \int d\mathbf{k}\rho(\mathbf{k}).
\end{aligned} \tag{6.59}$$

We find that $\mathrm{Im}G_{cc}(\mathbf{k},\omega)$ and $\mathrm{Im}G_{ff}(\mathbf{k},\omega)$ have the following form

$$\mathrm{Im}G_{cc}(\mathbf{k},\omega) = \frac{(Z_{cc}(\omega - \bar{\epsilon}_f) + Z_{cf}\overline{V}_{fc})}{\overline{\omega}_+(\mathbf{k}) - \overline{\omega}_-(\mathbf{k})}[-\pi\delta(\omega - \overline{\omega}_+(\mathbf{k})) + \pi\delta(\omega - \overline{\omega}_-(\mathbf{k}))] \tag{6.60}$$

and

$$\mathrm{Im}G_{ff}(\mathrm{k},\omega) = \frac{(Z_{ff}(\omega - \overline{\epsilon}(\mathbf{k})) + Z_{fc}\overline{V}_{cf})}{\overline{\omega}_+(\mathbf{k}) - \overline{\omega}_-(\mathbf{k})}[-\pi\delta(\omega - \overline{\omega}_+(\mathbf{k})) + \pi\delta(\omega - \overline{\omega}_-(\mathbf{k}))] \quad (6.61)$$

Therefore the sum is given by

$$\mathrm{Im}G_{cc}(\mathrm{k},\omega) + \mathrm{Im}G_{ff}(\mathrm{k},\omega) = \frac{(Z_{cc}(\omega - \overline{\epsilon}_f) + Z_{cf}\overline{V}_{fc} + Z_{ff}(\omega - \overline{\epsilon}(\mathbf{k})) + Z_{fc}\overline{V}_{cf})}{\overline{\omega}_+(\mathbf{k}) - \overline{\omega}_-(\mathbf{k})}$$
$$\times \quad [-\pi\delta(\omega - \overline{\omega}_+(\mathbf{k})) + \pi\delta(\omega - \overline{\omega}_-(\mathbf{k}))] \quad (6.62)$$

from which we can identify $Z_+(\overline{\omega}_+(\mathbf{k}))$ and $Z_-(\overline{\omega}_-(\mathbf{k}))$ in (6.59) as

$$Z_+(\overline{\omega}_+(\mathbf{k})) = -\frac{1}{\pi}\int \mathrm{d}\omega Z_+(\mathbf{k},\omega)\pi\delta(\omega - \overline{\omega}_+(\mathbf{k})) \quad (6.63)$$

and

$$Z_-(\overline{\omega}_-(\mathbf{k})) = -\frac{1}{\pi}\int \mathrm{d}\omega Z_-(\mathbf{k},\omega)\pi\delta(\omega - \overline{\omega}_-(\mathbf{k})) \quad (6.64)$$

where

$$Z_\pm(\overline{\omega}_\pm(\mathbf{k})) = \pm\mathrm{Tr}\Big[\frac{Z\Delta(\mathbf{k},\omega_\pm(\mathbf{k}))_{FL}}{\overline{\omega}_+(\mathbf{k}) - \overline{\omega}_-(\mathbf{k})}\Big]$$
$$= \pm\frac{Z_{cc}(\overline{\omega}_\pm(\mathbf{k}) - \overline{\epsilon}_f) + Z_{cf}\overline{V}_{fc} + Z_{ff}(\overline{\omega}_\pm(\mathbf{k}) - \overline{\epsilon}(\mathbf{k})) + Z_{fc}\overline{V}_{cf}}{\overline{\omega}_+(\mathbf{k}) - \overline{\omega}_-(\mathbf{k})}. \quad (6.65)$$

We evaluate the quasi-particle fraction $Z_-(E_F)$ at the Fermi Energy E_F and in the lower band since our filling is fixed to $n_c + n_f = 1.8$. To determine E_F it follows that the excitation energy of a quasi particle lower band is zero $\overline{\omega}_-(E_F) = 0$. This provides us with a condition which allows us to extract E_F from equation (6.58) which we find has the following form

$$E_F = \frac{\alpha(\mu)Z_{ff}V - Z_{cf}V}{Z_{cc} - \alpha(\mu)Z_{fc}} + \mu - \Sigma_{cc}^H \quad (6.66)$$

where

$$\alpha(\mu) = \frac{Z_{cc}V + Z_{cf}(\epsilon_f - \mu + \Sigma_{ff}^H)}{Z_{ff}(\epsilon_f - \mu + \Sigma_{ff}^H) + Z_{fc}V}. \quad (6.67)$$

89

Chapter 7

Kondo to Local Moment Transition

7.1 Overview of the Kondo to Local Moment Transition

Cerium is a prototype for the strongly correlated f electrons materials. One of the most spectacular properties of Cerium is the pressure induced isostructural volume transition between the large volume local moment phase (γ phase), and the small volume paramagnetic phase (α phase). It has been studied for over six decades, however, even with extensive efforts [104, 105, 106, 107, 108, 64, 66], there is still no consensus on the mechanism of this transition.

There are three main theories which may explain the volume collapse transition. The first theory is based on the promotional model [109, 110]. In this model, the $4f$ electrons are pushed into the conduction band of the $5d$ or $6s$ orbital. As the $4f$ orbital has a larger radius, the $4f$ electrons promoted to the conduction band must be less screened by the nucleus, thus the $5d$ and $6s$ orbitals will be less screened and their volume collapses. This model requires the Fermi energy to stay close to that of the energy of the $4f$ electrons. However, photoemission experiments suggest that there is a substantial difference between them. The second theory is based on the Mott transition [64]. The bandwidth of the $4f$ electrons is enhanced as the pressure is increased. This effectively increases the overlap among the $4f$ orbital and thus allows the $4f$ electrons to be delocalized. The Hubbard bands formed from the $4f$ merge with the conduction band to form the α phase with no local moment.

A different explanation from the above two theories is given by Allen and Martin which focuses on the hybridization between the localized $4f$ moment and the conduction band [111, 66, 112, 113]. The localized moment hybridizes with the valence band to form a Kondo resonance. In the small volume α-phase, the J is enhanced due to the pressure, and the Kondo singlet is formed below the Kondo temperature. As the pressure decreases, the Kondo temperature goes down, and the entropy from the free localized moment contributes to the free energy. Allen and Martin described the system in terms of the Kondo lattice model;

they found that using the result of the single Kondo impurity model and general arguments from thermodynamics, they could reproduc the first order transition in their calculation. Specifically, they calculated the Gibbs free energy given by $G = F + P\Omega = U - TS + P\Omega$, where F, U, S, and Ω are the free energy, internal energy, entropy, and volume per Cerium atom respectively. With the input of the free energy from the single impurity Kondo model, they showed that the P, Ω, T relation for low enough temperature always has points with $dP/dV = 0$ which indicates the first order transition. As it has been pointed out in the original paper [66], the detailed form of the contribution from Kondo effects is not critical; what is important is the non-linear relation between the Kondo coupling and its contribution in the free energy. The Kondo volume collapse theory seems to be able to describe many different experiments [111]. Importantly, it can describe the Abrikosov-Suhl resonance as observed in the experiment [111]. Based on initial inelastic neutron scattering experiment the contribution to the entropy from the phonon was suggested to be negligible. However recent high resolution neutron and x-ray diffraction experiments suggest that the lattice degree of freedom may play a role in the $\alpha - \gamma$ transition. In particular, it has been suggested that the phonons contribute almost half of the entropy across the transition [69, 63, 19].

In light of these recent experimental results, we propose a minimal model based on the Kondo Volume collapse model to explain the effects of the electron-phonon coupling. We begin from the standard periodic Anderson model and incorporate the electron-phonon coupling by replacing the metallic band with the local electron-phonon coupling to the Einstein phonon, that is the Holstein model. Within the Kondo volume collapse model, the $\alpha \leftrightarrow \gamma$ transition can be explained by the Kondo lattice model, in the α phase the small volume provides large effective Kondo coupling, J. A Kondo singlet is formed below the Kondo temperature. Along this line of thought, there are two possible scenarios with the introduction of electron-phonon coupling in the conduction band: 1. Long range ordering (charged density wave or pairing) formed in the conduction band opens a gap at the Fermi level, effectively destroying the Kondo effect and thus the α-phase. 2. No long range ordering is formed in the conduction band; the correlated band only affects the Kondo temperature. In the case where the conduction electrons are described by the Hubbard Hamiltonian, the repulsive and attractive Hubbard interaction will enhance and reduce the Kondo temperature respectively. Therefore, at least in the anti-adiabatic limit and not too strong electron-phonon coupling or not too low temperature (where long range ordering is avoided), even though no long range ordering is formed in the conduction band, the α-phase is likely to be pushed to lower temperature or larger pressure.
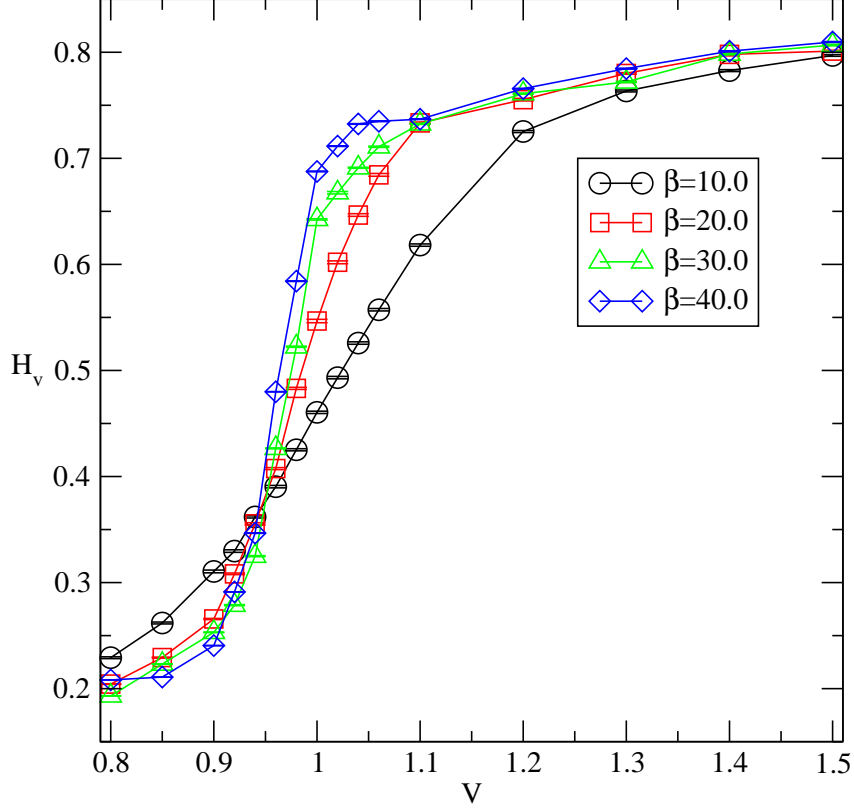
Figure 7.1: H_V vs. V is plotted for fixed Hamiltonian parameters $U = 4.0$, $\frac{g^2}{2k} = 1.0$, and $\omega_0 = 0.01$, where the hybridization was varied from $V = [0.8, 1.5]$ for four values of inverse temperature $\beta = 10, 20, 30$ and 40. When $V \approx \frac{g^2}{2k} = 1.0$ a sudden increase in the H_V occurs for $V \sim 1.0$ indicating that Kondo screening of the impurity has occurred. As the temperature is lowered the discontinuity in H_V at $V = 1.0$ is more apparent indicating a sudden transition in the dominant correlations. Consequently for $V > 1.0$ (large pressure) the system is in the α phase where the Kondo correlations are enhanced. For $V < 1.0$ (small pressure) the system moves to the γ phase where Kondo correlations are reduced.

Here we will illustrate our DMFT results of the PAM [104, 105, 106, 107, 108] with the inclusion of electron-phonon coupling in the conduction band, in an attempt to better understand the effects of phonon correlations in the $\alpha \leftrightarrow \gamma$ transition of the Cerium volume collapse[109, 110, 64, 66, 112, 113]. All the simulations were performed with the fixed Hamiltonian parameters and $t^\star = 1$. The Hubbard interaction U between impurity electrons was fixed to $U = 4.0$ to place the simulation in the Kondo regime and the phonon frequency was set to the adiabatic limit of $\omega_0 = 0.01$ which reflects that the Debye temperature relative to the Fermi Energy in Cerium is small [69]. The electron-phonon $\frac{g^2}{2k}$ interaction, inverse temperature $\beta = \frac{1}{k_B T}$ and hybridization V were varied. The hybridization was varied to

reflect changes in pressure in the $\alpha \leftrightarrow \gamma$ transition of Cerium. For a finite range of electron-phonon coupling as the hybridization was varied from small (small pressure) to large (large pressure) an abrupt transition occurred from dominant phononic correlations at small values of hybridization to dominant Kondo correlations at larger values of hybridization. This transition suggests that the phononic correlations are more active for small values of pressure and not as significant at larger values of pressure where Kondo screening of the inner f electron occurs. The transition between phononic and Kondo phase in our simulations occurred when the phononic and Kondo energies were of the same order $\frac{g^2}{2k} \approx V$. Interestingly we found that increasing $\frac{g^2}{2k}$ was similar to decreasing the temperature T in our simulations. At low T or large $\frac{g^2}{2k}$ it was found that a hysteretic solution resulted from the competition between the phononic and Kondo correlations resulting in two distinct minima of the thermodynamic potential Ω. In the following sections we will cover the correlation functions that have allowed us to come to these conclusions. As stated above all the simulations were done with $U = 4.0$ (indicative of the Kondo regime of cerium) and $\omega_0 = 0.01$ (adiabatic phonons applicable to cerium) where the hybridization was varied from $V = [0.8, 1.5]$ in an effort to simulate changes in pressure across the collapse. All the results of the simulations were performed for inverse temperatures $\beta = 10, 20, 30, 40$ and 60.

7.2   Kondo Correlation Function

The Kondo order parameter was calculated by differentiating the free energy with respect to hybridization

$$H_V = -\frac{1}{N\beta}\frac{\partial F}{\partial V} = \langle c^\dagger f + f^\dagger c \rangle. \tag{7.1}$$

Here $\langle c^\dagger f \rangle$ is the amplitude that an electron propagates from the impurity band (f), hybridizes via V and propagates in the conduction band $(c^\dagger)$, and $\langle f^\dagger c \rangle$ is just the inverse process. As shown in Fig. 7.1 H_V was plotted as a function of V for $\frac{g^2}{2k} = 1.0$ and inverse temperatures $\beta = 10, 20, 30$ and 40. The most salient feature of the Kondo order parameter is the abrupt increase in H_V around $V = 1.0$, which becomes sharper as the temperature is lowered resulting in a step function appearance. For $V > 1.0$ the system is in the Kondo phase since H_V is enhanced, which corresponds to the large pressure α phase of cerium, hence large Kondo screening. For small values of pressure when $V < 1.0$ the Kondo correlations are reduced significantly; this phase is indicative to the γ phase of cerium.
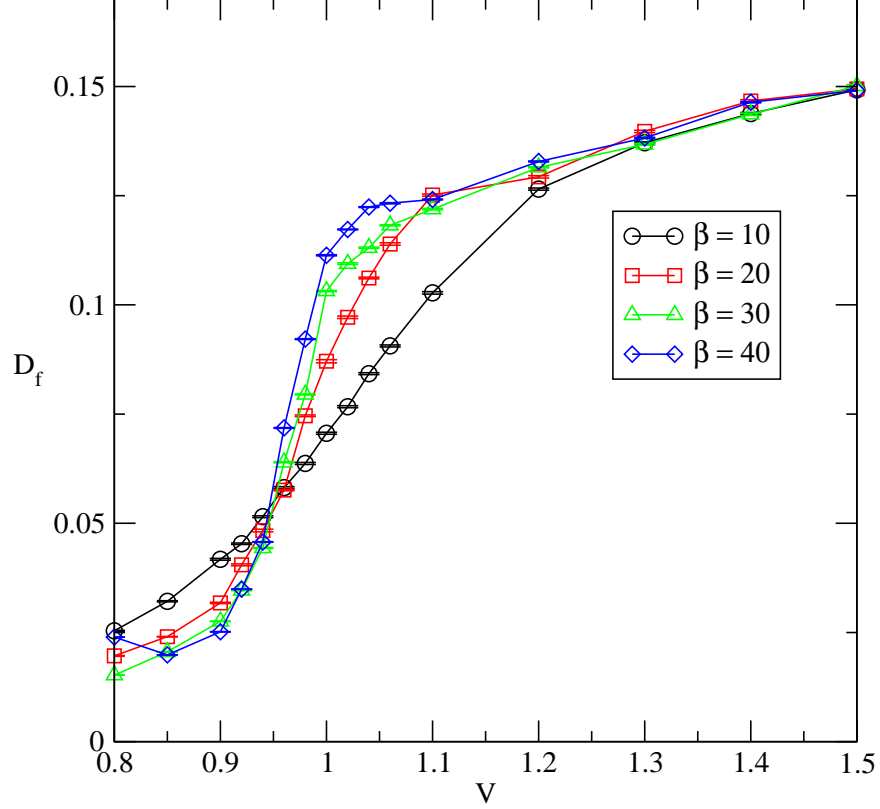
Figure 7.2: D_f vs. V is plotted for fixed Hamiltonian parameters $U = 4.0$, $\frac{g^2}{2k} = 1.0$, and $\omega_0 = 0.01$, where the hybridization was varied from $V = [0.8, 1.5]$ for four values of inverse temperature $\beta = 10, 20, 30$ and 40. A sudden increase in D_f occurs around $V \sim 1.0$ which becomes more discontinuous as the temperature is lowered. D_f is larger in the α phase $V > 1.0$ because Kondo screening is enhanced. For $V < 1.0$ D_f is significantly reduced in the γ phase since Kondo screening is absent.

7.3 Double Occupancy

Double occupation of the impurity site was calculated by performing a functional derivative of the free energy with respect to U

$$D_f = -\frac{1}{\beta}\frac{\partial F}{\partial U} = \langle n_f^\uparrow n_f^\downarrow \rangle. \tag{7.2}$$

In this equation $n_f^\uparrow$ and $n_f^\downarrow$ are the density of spin-up and spin-down impurity electrons, therefore $\langle n_f^\uparrow n_f^\downarrow \rangle$ is a measure of the double occupation of the impurity site by spin-up and spin-down electrons at the same time. D_F is displayed in Fig. 7.2 as a function of V. One
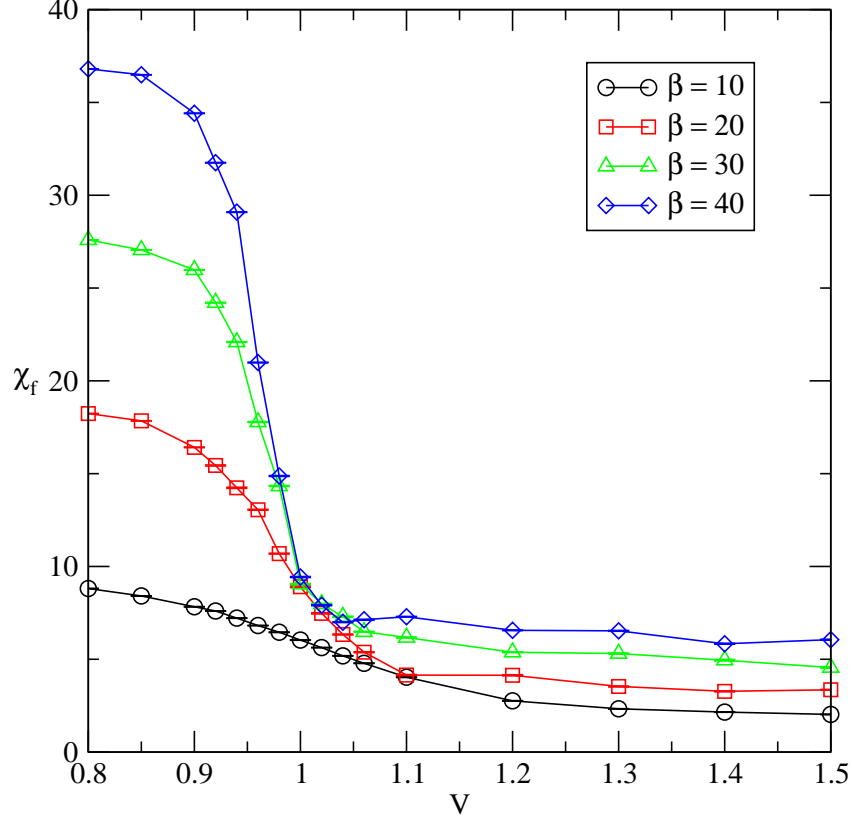
Figure 7.3: χ_f vs. V is plotted for fixed Hamiltonian parameters $U = 4.0$, $\frac{g^2}{2k} = 1.0$, and $\omega_0 = 0.01$, where the hybridization was varied from $V = [0.8, 1.5]$ for four values of inverse temperature $\beta = 10, 20, 30$ and 40. For $V > 1.0$ χ_f is significantly reduced indicating that the impurity spin is Kondo screened. For $V < 1.0$ in the γ phase χ_f is significantly enhanced as a result of the absence of the Kondo screening which implies that the impurity site is singly occupied.

will notice that a sharp increase occurs in D_F around $V = 1.0$ which also has the appearance of a step function as the temperature is reduced. For $V \sim 1.0$ the transition from the γ to the α phase occurs. The double occupation has it largest value in the α phase $V > 1.0$ since Kondo screening is largest (Fig. 7.1) in this phase and therefore two electrons of opposite spin can occupy the impurity site in accordance with the Pauli exclusion principle. For $V < 1.0$ D_f is reduced in the γ phase since Kondo screening of the impurity electrons is suppressed see (Fig. 7.1) and double occupation of the impurity site is reduced.
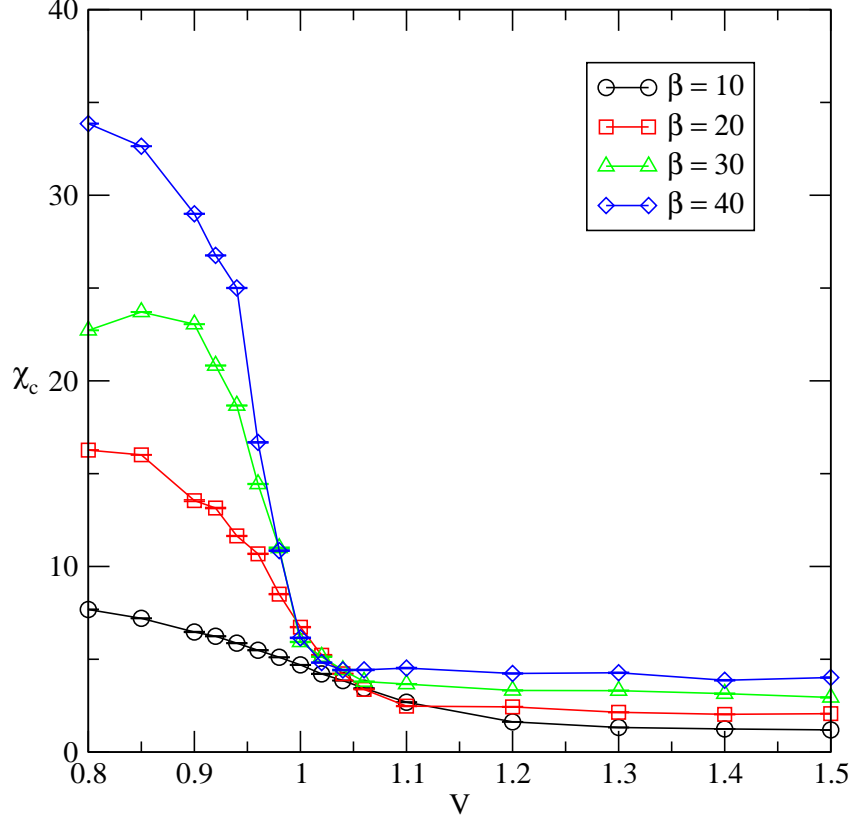
Figure 7.4: χ_c vs. V is plotted for fixed Hamiltonian parameters $U = 4.0$, $\frac{g^2}{2k} = 1.0$, and $\omega_0 = 0.01$, where the hybridization was varied from $V = [0.8, 1.5]$ for four values of inverse temperature $\beta = 10, 20, 30$ and 40. For $V > 1.0$ χ_c in the conduction band is significantly reduced since Kondo screening is present. However when $V < 1.0$ χ_c is significantly enhanced in the γ phase since the Kondo correlations are reduced.

7.4   Impurity Spin Correlations

The z component of the local impurity susceptibility χ_f was calculated from

$$\chi_f = \int_0^\beta d\tau (\langle TS_f^z(\tau)S_f^z\rangle - \langle S_f^z(\tau)\rangle\langle S_f^z\rangle) \tag{7.3}$$

In this equation $S_f^z = n_f^\uparrow - n_f^\downarrow$ is the z-component of the spin of the f electron, which is zero when $n_f^\uparrow = n_f^\downarrow$. In Fig. 7.3 χ_f increased for $V < 1.0$ indicating that the local electron is not correlated with an additional electron bound in a Kondo singlet state. For $V < 1.0$ the state of the system is in the local moment regime γ. When $V > 1.0$ χ_f is significantly reduced as a consequence of the binding of two impurity electrons, this indicates the formation of

96

the Kondo singlet state, which is indicative of the small volume α phase in cerium. As the temperature is reduced in the γ phase χ_f increases indicating single occupancy of the impurity site.
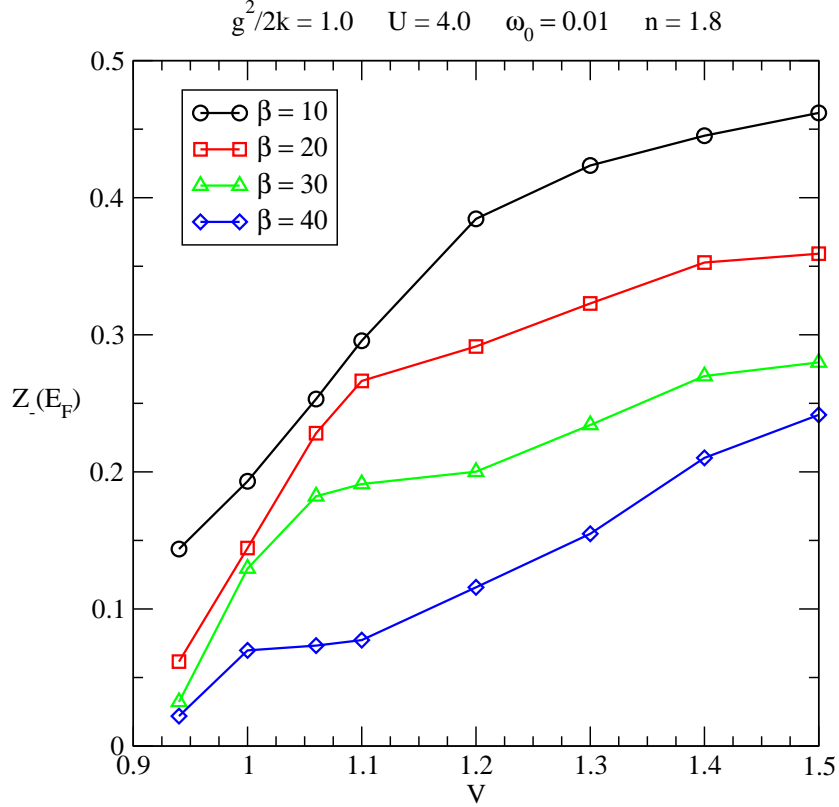

Figure 7.5: $Z_-(E_F)$ vs. V is plotted for the Hamiltonian parameters $U = 4.0$, $\frac{g^2}{2k} = 1.0$, and $\omega_0 = 0.01$, where the hybridization was varied from $V = [0.94, 1.5]$ the temperature was varied from $\beta = 10, 20, 30$ and 40 and the total filling was fixed to $n = 1.8$. Observe when $V > 1$ the quasi-particle fraction is reduced from its Fermi-liquid value as the temperature is decreased; which is the result of an increase in polaronic correlations in the conduction band. Similarly for $V < 1.0$ the quasi-particle fraction is significantly reduced from its Fermi-liquid value, since the polaronic correlations are enhanced for $V < \frac{g^2}{2k} = 1.0$. This plot indicates that decreasing the temperature enhances the effective electron phonon coupling $\frac{g^2}{2k}$, which increases electron mass $m^\star$ resulting in polaron formation, thus reducing the Fermi-liquid quasi-particle fraction $Z = \frac{m}{m^\star}$.

7.5 Phononic Correlations

The conduction band susceptibility χ_c was calculated using the formula

$$\chi_c = \int_0^\beta d\tau(\langle Tn_c(\tau)n_c\rangle - \langle n_c(\tau)\rangle\langle n_c\rangle). \tag{7.4}$$

In this equation $n_c = n_c^\uparrow + n_c^\downarrow$ is the total conduction band density. As the correlations in time build up the correlation function is enhanced $\langle n_c(\tau)n_c\rangle$. In (Fig. 7.4) for $V < 1.0$ the electronic correlations in the conduction band are enhanced as a result of the strong electron-phonon interaction between electrons where $\frac{g^2}{2k} = 1.0$. This correlation function suggests that for $V < 1.0$ the electron phonon correlations in the conduction band are responsible for the reduction of the Kondo correlations for $V < 1.0$ see (Fig. 7.1). This suggests in the large volume phase γ there will be an enhancement in the polaronic correlations in the conduction band of cerium. In the small volume α phase the Abrikosov Suhl resonance at the Fermi level will reemerge indicative of large Kondo spin flip correlations between the conduction and localized electrons.

7.6 Quasi-Particle Renormalization Fraction

The renormalization of the quasi-particles at the Fermi energy E_F in the lower band with filling $n_f + n_c = 1.8$ was calculated using the phenomenological Fermi Liquid approximation applied to the α phase in our model for $V > 1.0$, since this phase is known to possess all the properties of a Fermi liquid[100]. In particular we were interested in how the mass of the quasi-particles changed as the temperature was reduced and as a function of hybridization V; the results are displayed in (Fig. 7.5). The formula used to calculate the quasi-particle fraction of the lower band $Z_-(E_F)$ has the following form

$$
\begin{aligned}
Z_-(\overline{\omega}_-(\mathbf{k}_F)) &= -\mathrm{Tr}\Big[\frac{Z\Delta(\mathbf{k},\omega_-(\mathbf{k}))_{FL}}{\overline{\omega}_+(\mathbf{k}) - \overline{\omega}_-(\mathbf{k})}\Big]\Big|_{\mathbf{k}=\mathbf{k}_F} \\
&= -\frac{Z_{cc}(\overline{\omega}_-(\mathbf{k}_F) - \overline{\epsilon}_f) + Z_{cf}\overline{V}_{fc} + Z_{ff}(\overline{\omega}_-(\mathbf{k}_F) - \overline{\epsilon}(\mathbf{k}_F)) + Z_{fc}\overline{V}_{cf}}{\overline{\omega}_+(\mathbf{k}_F) - \overline{\omega}_-(\mathbf{k}_F)}. \tag{7.5}
\end{aligned}
$$

Here $\mathbf{k}_F$ is the Fermi momentum. As shown in (Fig. 7.5) we observe as the temperature is reduced for $V > 1.0$ in the α phase that $Z_-(E_F)$ decreases; this indicates that the effective mass of the electrons $m^\star$ increases. This is consistent with the increase in the density-
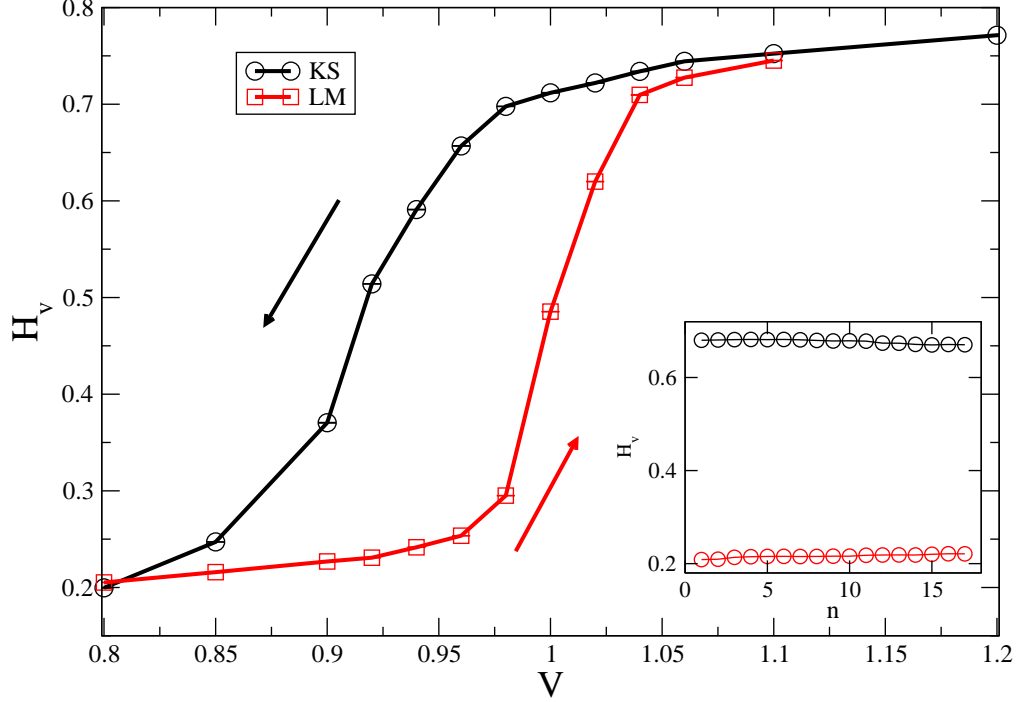
Figure 7.6: H_V vs. V is plotted in the hysteretic region for inverse temperature $\beta = 60$ for the fixed Hamiltonian parameters $U = 4.0$, $\frac{g^2}{2k} = 1.0$, and $\omega_0 = 0.01$, where the hybridization was varied from $V = [0.8, 1.5]$. The historetic region exists in the interval $V \epsilon [0.85, 1.1]$. The upper branch possesses dominant Kondo correlations while the lower branch has dominant phononic correlations. The inset shows the stability of upper and lower branches as a function of DMFT iterations.

density correlations χ_c in the conduction band for $V > 1.0$ see (Fig. 7.4); which shows that the polaronic correlation increases as the temperature decreases, hence the electron phonon correlations become more active at lower temperatures. The increase in the density-density correlations in the conduction band will reduce the $T_{\mathbf{K}}$ since $Z_-(E_F)$ decreases. Therefore we postulate that the Kondo temperature is reduced as the electron phonon coupling increases in the following way: $T_K \sim \exp(-\frac{g^2/2k}{V})$. Physically T_K approximated in this way indicates that increasing the electron-phonon interactions prevents conduction electrons from hybridizing and screening the impurity electron thus reducing $T_{\mathbf{K}}$.

7.7   First Order Phase Transition: Hysteresis

As the temperature is reduced to $\beta = 60$ the phononic correlations continue to increase in the conduction band which reduces the Kondo temperature $T_{\mathbf{K}}$. At this temperature the

99

energy of the phononic correlations in the conduction band are comparable to the energy of the Kondo correlations, which creates two possible states that minimize the thermodynamic potential Ω. For temperatures $T < T_c$ if the system is prepared initially in the γ phase and pressure is exerted on the system in the hysteretic region the system will be stable in the local minimum of Ω with dominant phononic correlations in the conduction band. On the other hand, if the system is initially prepared in the α phase at large pressure, as the pressure is gradually reduced and the system enters the hysteretic region it will be in a state of stable equilibrium of Ω with dominant Kondo correlations. This situation is illustrated in (Fig. 7.6). The inset of this figure corresponds to the stability of the upper and lower branches of the hysteresis as a function of DMFT interactions. The historetic region exists for $V \epsilon [0.85, 1.1]$, where the critical value of hybridization is given by $V_c \approx 0.975$ at this temperature. Clearly the first order terminus or the critical point where the hysteresis initially opens exists at a higher temperature, but not higher than $\beta = 40$ since no hysteresis was found at this temperature.

The first order terminus for the PAM + Holstein model can be characterized by the triplet $(V_c, T_c, \frac{g^2}{2k}c)$ in a three dimensional space. Increasing $\frac{g^2}{2k}$ increases the critical point in the three dimensional space thus the opening of the hysteresis will occur for larger values of V_c and T_c. The reasoning here is that increasing the electron phonon coupling increases the density density correlations between conduction electrons which requires a larger value of hybridization to initiate the Kondo effect. As a consequence we predict that there is an energy scale such as $T_K \sim \exp(-\frac{g^2/2k}{V})$ which determines the Kondo temperature for an attractive interaction in the conduction band based on the behavior of H_v, D_f, χ_f, χ_c and $Z_-(E_F)$ depicted in Figures 7.1 through 7.6.

Chapter 8

Conclusion

In this thesis we predicted that other bimetallic oxalates would exhibit magnetic compensation, in which the direction of the magnetization flipped at a temperature below the initial ferrimagnetic transition temperature. In addition we predicted that bimetallic oxalates that exhibited magnetic compensation would also possess a measurable spin-wave gap of the order of 8.0 meV, which could be detected in neutron diffraction experiments of these materials.

With regards to the cerium volume collapse, we showed that the inclusion of electron-phonon coupling in the conduction band in our model Hamiltonian, would result in a phase with dominant phononic correlations in the γ phase which existed for small values of V (small pressure). In the limit of the α phase (large pressure) which occurred in our model at large values of hybridization V between the conduction and impurity electrons, we observed an increase in Kondo correlation and subsequent reduction in phononic correlation. In particular we were able to show that the $\alpha \leftrightarrow \gamma$ transition of our model simulations using DMFT resulted in a first order phase transition, in which a hysteresis loop developed for temperatures below the Kondo $T_{\mathbf{K}}$ and phononic transition $T_{\mathbf{FC}}$ temperatures.

Appendix A

A.1 Model Hamiltonian in Spinor Notation

To simplify our calculations of the periodic Anderson model with Holstein phonons coupled to the conduction electrons we compress the impurity Hamiltonian

$$
\begin{aligned}
H &= \sum_{\mathbf{k},\sigma} \epsilon_{\mathbf{k}} c^{\dagger}_{\mathbf{k},\sigma} c_{\mathbf{k},\sigma} + \epsilon_f \sum_{i,\sigma} f^{\dagger}_{i,\sigma} f_{i,\sigma} + \sum_{\mathbf{k},i,\sigma} V_{\mathbf{k}} (c^{\dagger}_{\mathbf{k},\sigma} f_{i,\sigma} + f^{\dagger}_{i,\sigma} c_{\mathbf{k},\sigma}) \\
&+ U n_{f,\uparrow} n_{f,\downarrow} - \int_0^\beta \mathrm{d}\tau D_0(\tau) n_c(\tau) n_c \\
&+ \omega_0 (a^{\dagger} a + \frac{1}{2})
\end{aligned}
\tag{A.1}
$$

using the spinor representation

$$
\underline{\Psi}_{\mathbf{k},i} = \left\{ \begin{array}{c} c_{\mathbf{k}} \\ f_i \end{array} \right\}
\tag{A.2}
$$

into a form more reminiscent of a one band model. Where the first term has the form of the one band kinetic energy model, the second term has the form of a single band potential energy model and the last term corresponds to the kinetic energy of a non-interacting phonon located at the impurity,

$$
\begin{aligned}
H &= \sum_{\mathbf{k},i,\sigma} \underline{\Psi}^{\dagger}_{\mathbf{k},i,\sigma} \underline{\epsilon}(\mathbf{k},i) \underline{\Psi}_{\mathbf{k},i,\sigma} \\
&+ \sum_{\mathbf{k},i,\sigma,\sigma',j=1,2} \int_0^\beta \mathrm{d}\tau \mathrm{d}\tau' V_{\sigma,\sigma'}(\mathbf{k},i,j,\tau-\tau') (\underline{\Psi}^{\dagger}_{\mathbf{k},i,\sigma'}(\tau) \underline{\alpha}_j \underline{\Psi}_{\mathbf{k},i,\sigma'}(\tau)) (\underline{\Psi}^{\dagger}_{\mathbf{k},i,\sigma}(\tau') \underline{\alpha}_j \underline{\Psi}_{\mathbf{k},i,\sigma}(\tau')) \\
&+ \omega_0 (a^{\dagger} a + \frac{1}{2}).
\end{aligned}
\tag{A.3}
$$

The kinetic energy matrix is given by

$$\underline{\epsilon}(\mathbf{k}, i) = \left\{ \begin{array}{cc} \epsilon(\mathbf{k})\delta_{i,0} & V(\mathbf{k}) \\ V(\mathbf{k}) & \epsilon_f \delta_{\mathbf{k},0} \end{array} \right\}. \tag{A.4}$$

The potential energy reproduces the impurity Hubbard and impurity electron-phonon interactions when $j = 1$ and $j = 2$ respectively. The Hubbard interaction has the following form at the impurity,

$$V_{\sigma,\sigma'}(\mathbf{k}, i, j = 1, \tau) = \frac{U}{2\beta}\delta_{\sigma',-\sigma}\delta_{\mathbf{k},0}\delta_{i,0}\delta(\tau) \tag{A.5}$$

where

$$\underline{\alpha_1} = \left\{ \begin{array}{cc} 0 & 0 \\ 0 & 1 \end{array} \right\}. \tag{A.6}$$

We find that the electron-phonon interaction has the following form at the impurity

$$V_{\sigma,\sigma'}(\mathbf{k}, i, j = 2, \tau - \tau') = -\frac{1}{\beta}D_0(\tau - \tau')\delta_{\mathbf{k},0}\delta_{i,0} \tag{A.7}$$

with

$$\underline{\alpha_2} = \left\{ \begin{array}{cc} g & 0 \\ 0 & 0 \end{array} \right\}. \tag{A.8}$$

Having cast our two band model into a single band model with the use of a spinor Ψ allows us to calculate ANY quantity we wish within Feynman-Dyson perturbation theory as if our model were a single band model. This is possible just by rewriting the Hamiltonian in a spinor form! In the next couple of sections we will illustrate the usefulness of doing this.

A.2 Internal Energy $E = \langle H \rangle$

In this section we will demonstrate how to calculate the internal energy E of our model Hamiltonian in A.3. The most straightforward way to do this would be to perform the thermal expectation value of equation A.3

$$E = \langle H \rangle, \tag{A.9}$$

where $\langle\cdots\rangle = \mathrm{Tr}\,e^{-\beta H}\cdots$. However there is another way to do this which we will overview the details of the calculation, it will be Green's function based. We will use the equation of motion technique to arrive at an equivalent expression as in A.9. First we compute the imaginary time derivative of $\underline{\Psi}_{\mathbf{p},z,\alpha}(\tau)$

$$
\begin{aligned}
\frac{\partial \underline{\Psi}_{\mathbf{p},z,\alpha}(\tau)}{\partial \tau} &= -[\underline{\Psi}_{\mathbf{p},z,\alpha}(\tau), H] \\
&= -[\underline{\Psi}_{\mathbf{p},z,\alpha}(\tau), H_0] - [\underline{\Psi}_{\mathbf{p},z,\alpha}(\tau), H_{int}] \\
&= -\underline{\epsilon}(pz)\underline{\Psi}_{\mathbf{p},z,\alpha}(\tau) \\
&\quad - \sum_{\sigma,j=1,2}\int_0^\beta \mathrm{d}\tau' V_{\sigma,\alpha}(p,z,j,\tau-\tau')\beta\underline{\alpha}_j\underline{\Psi}_{\mathbf{p},z,\alpha}(\tau)(\underline{\Psi}^\dagger_{\mathbf{p},z,\sigma}(\tau')\underline{\alpha}_j\underline{\Psi}_{\mathbf{p},z,\sigma}(\tau'))
\end{aligned}
\tag{A.10}
$$

In the last equation perform $-\frac{1}{2}\sum_{\mathbf{p},z,\alpha}\frac{1}{\beta}\int_0^\beta \mathrm{d}\tau\langle\underline{\Psi}^\dagger_{\mathbf{p},z,\alpha}(\tau)\otimes\cdots\rangle$ on both sides of the equation to arrive at an expression for the potential energy of the system,

$$
\begin{aligned}
\text{P.E.} &= \langle H_{\mathrm{int}}\rangle \\
&= \sum_{\mathbf{p},z,\alpha,\sigma,j=1,2}\frac{1}{2}\int_0^\beta\int_0^\beta \mathrm{d}\tau\mathrm{d}\tau' V_{\sigma,\alpha}(p,z,j,\tau-\tau')\langle(\underline{\Psi}^\dagger_{\mathbf{p},z,\alpha}(\tau)\underline{\alpha}_j\underline{\Psi}_{\mathbf{p},z,\alpha}(\tau))(\underline{\Psi}^\dagger_{\mathbf{p},z,\sigma}(\tau')\underline{\alpha}_j\underline{\Psi}_{\mathbf{p},z,\sigma}(\tau'))\rangle \\
&= -\frac{1}{2}\sum_{\mathbf{p},z,\alpha}\Big[\underline{I}\frac{\partial}{\partial\tau}+\underline{\epsilon}(\mathbf{p},z)\Big]G_{\mathbf{p},z,\alpha}(-\eta).
\end{aligned}
\tag{A.11}
$$

In the last step the trace Tr is implied since the Green's function

$$
G_{\mathbf{p},z,\alpha}(-\eta) = \langle\underline{\Psi}^\dagger_{\mathbf{p},z,\alpha}(0)\otimes\underline{\Psi}_{\mathbf{p},z,\alpha}(-\eta)\rangle
\tag{A.12}
$$

is evaluated in the limit that $\eta\to 0$. With this understanding A.11 can be written as

$$
\begin{aligned}
\text{P.E.} &= -\frac{1}{2}\sum_{\mathbf{p},z,\alpha}\Big[\underline{I}\frac{\partial}{\partial\tau}+\underline{\epsilon}(\mathbf{p},z)\Big]G_{\mathbf{p},z,\alpha}(-\eta) \\
&= -\frac{1}{2}\sum_{\mathbf{p},z,\alpha}\int_0^\beta \mathrm{d}\tau\,\delta(\tau+\eta)\Big[\underline{I}\frac{\partial}{\partial\tau}+\underline{\epsilon}(\mathbf{p},z)\Big]G_{\mathbf{p},z,\alpha}(\tau) \\
&= -\frac{1}{2}\sum_{\mathbf{p},z,\alpha}\int_0^\beta \mathrm{d}\tau\,\frac{1}{\beta}\sum_{\omega_n=-\infty}^\infty e^{i\omega_n(\tau+\eta)}\Big[\underline{I}\frac{\partial}{\partial\tau}+\underline{\epsilon}(\mathbf{p},z)\Big]G_{\mathbf{p},z,\alpha}(\tau).
\end{aligned}
\tag{A.13}
$$

The integration by parts with respect to τ is done so the derivative term can be evaluated,

$$\int_0^\beta \mathrm{d}\tau \mathrm{e}^{i\omega_n\tau}\underline{I}\frac{\partial}{\partial\tau}G_{\mathbf{p},z,\alpha}(\tau) = -\int_0^\beta \mathrm{d}\tau \underline{I}i\omega_n\mathrm{e}^{i\omega_n\tau}G_{\mathbf{p},z,\alpha}(\tau)+\text{const.}. \qquad (A.14)$$

Inserting this back into the equation for P.E. we find

$$\begin{aligned}\text{P.E.} &= \frac{1}{2\beta}\sum_{\mathbf{p},z,\alpha,\omega_n}\mathrm{e}^{i\omega_n\eta}\Big[\underline{I}i\omega_n-\underline{\epsilon}(\mathbf{p},z)\Big]\int_0^\beta \mathrm{d}\tau\mathrm{e}^{i\omega_n\tau}G_{\mathbf{p},z,\alpha}(\tau)\\ &= \frac{1}{2\beta}\sum_{\mathbf{p},z,\alpha,\omega_n}\Big[\underline{I}i\omega_n-\underline{\epsilon}(\mathbf{p},z)\Big]G_{\mathbf{p},z,\alpha}(i\omega_n)\mathrm{e}^{i\omega_n\eta}\\ &= \frac{1}{2\beta}\sum_{\mathbf{p},z,\alpha,\omega_n}G^{o,-1}_{\mathbf{p},z,\alpha}(i\omega_n)G_{\mathbf{p},z,\alpha}\mathrm{e}^{i\omega_n\eta}. \end{aligned} \qquad (A.15)$$

In the last equation we replace $G^{o,-1}_{\mathbf{p},z,\alpha}(i\omega_n)$ using the Dyson's equation where the self-energy Σ is momentum independent within DMFT,

$$G^{o,-1}_{\mathbf{p},z,\alpha}(i\omega_n)=G^{-1}_{\mathbf{p},z,\alpha}(i\omega_n)+\delta_{\mathbf{p}z,0}\Sigma_{\mathbf{p},z,\alpha}(i\omega_n). \qquad (A.16)$$

Then the equation for P.E. has the following form

$$\text{P.E.} = \frac{1}{2\beta}\sum_{\mathbf{p},z,\alpha,\omega_n}\delta_{\mathbf{p}z,0}\text{Tr}[\Sigma_{\mathbf{p},z,\alpha}(i\omega_n)G_{\mathbf{p},z,\alpha}(i\omega_n)]\mathrm{e}^{i\omega_n\eta}. \qquad (A.17)$$

This expression for P.E. expresses that the potential energy within DMFT is an impurity quantity. The kinetic energy (K.E.) can be calculated in the following manner

$$\begin{aligned}\text{K.E.} &= \sum_{\mathbf{p},z,\alpha}\langle\underline{\Psi}^\dagger_{\mathbf{p},z,\alpha}\underline{\epsilon}(\mathbf{p},z)\underline{\Psi}_{\mathbf{p},z,\alpha}\rangle\\ &= \sum_{\mathbf{p},z,\alpha}\text{Tr}[\underline{\epsilon}(\mathbf{p},z)G_{\mathbf{p},z,\alpha}(-\eta)]\\ &= \frac{1}{\beta}\sum_{\mathbf{p},z,\alpha,\omega_n}\text{Tr}[\underline{\epsilon}(\mathbf{p},z)G_{\mathbf{p},z,\alpha}(i\omega_n)]\mathrm{e}^{i\omega_n\eta}. \end{aligned} \qquad (A.18)$$

The K.E. is a lattice quantity. Summing the kinetic and potential energies and adding back the energy from the non-interacting phonon, the internal energy of the PAM with Holstein phonons coupled to the conduction electrons is

$$\text{E} = \text{K.E.}+\text{P.E.}+\omega_0(\langle a^\dagger a\rangle+\frac{1}{2})$$

$$
\begin{aligned}
= \quad & \frac{1}{\beta} \sum_{\mathbf{p},z,\alpha,\omega_n} \mathrm{Tr}[\underline{\epsilon}(\mathbf{p},z)G_{\mathbf{p},z,\alpha}(i\omega_n)]\mathrm{e}^{i\omega_n\eta} \\
+ \quad & \frac{1}{2\beta} \sum_{\mathbf{p},z,\alpha,\omega_n} \delta_{\mathbf{p}z,0} \mathrm{Tr}[\Sigma_{\mathbf{p},z,\alpha}(i\omega_n)G_{\mathbf{p},z,\alpha}(i\omega_n)]\mathrm{e}^{i\omega_n\eta} \\
+ \quad & \omega_0(\langle a^\dagger a \rangle + \frac{1}{2}).
\end{aligned} \tag{A.19}
$$

The internal energy is depicted in (Fig. A.1) in terms of Feynman diagrams. The Kinetic energy of the system corresponds to the closed fermion loop times ϵ. The second term represents the many-body two particle potential energy located at the impurity site, which diagrammatically represents $\frac{1}{2}\mathrm{Tr}\Sigma G$, where in the figure we have depicted Σ using the Schwinger-Dyson equation which includes the vertex function F. The last term represents a non-interacting phonon which oscillates with frequency ω and is located at the impurity site.

Closing this section we show that our derivation of E in equation (A.9) is consistent with an action S based determination of E up to an indeterminate additive constant C. Moreover in this way we were able to deduce the Hamiltonian of equation (A.1). To show the equivalence we consider two equivalent representations of the partition function Z subject to the variation $\beta + \delta\beta$

$$
\begin{aligned}
Z(\beta + \delta\beta) \quad &= \quad \mathrm{Tr}e^{-(\beta+\delta\beta)H} \\
&= \quad \int \mathrm{D}\overline{\Psi}\mathrm{D}\Psi e^{-(S(\beta)+\frac{\delta S}{\delta\beta}\delta\beta)}.
\end{aligned} \tag{A.20}
$$

Taylor expanding both representations of Z with respect to $\delta\beta$ yields two equivalent changes in the partition function $\frac{\delta Z}{\delta\beta}\delta\beta$, which results in the important relationship

$$
\langle H \rangle \quad = \quad \Big\langle \frac{\delta S}{\delta\beta} \Big\rangle. \tag{A.21}
$$

This expression allows one to calculate the internal energy E from an action S based formulation. Next we justify the validity of this equation. To do this we perform $\frac{\delta S}{\delta\beta}$ starting from the fact that S is the imaginary time integral of the Lagrangian density

$$
S \quad = \quad \int_0^\beta \mathcal{L}(\Psi(\tau), \dot{\Psi}(\tau), \overline{\Psi}(\tau), \dot{\overline{\Psi}}(\tau))\mathrm{d}\tau. \tag{A.22}
$$

106

Performing the variation of S with respect to β we find

$$
\begin{aligned}
\left\langle \frac{\delta S}{\delta \beta} \right\rangle &= \left\langle \frac{\delta}{\delta \beta} \int_0^\beta \mathcal{L}(\Psi(\tau), \dot{\Psi}(\tau), \overline{\Psi}(\tau), \dot{\overline{\Psi}}(\tau)) \right\rangle \\
&= \left\langle \mathcal{L}(\Psi(\beta), \dot{\Psi}(\beta), \overline{\Psi}(\beta), \dot{\overline{\Psi}}(\beta)) \right\rangle \\
&= \left\langle \mathcal{L}(\Psi(0), \dot{\Psi}(0), \overline{\Psi}(0), \dot{\overline{\Psi}}(0)) \right\rangle \\
&= \left\langle \overline{\Psi}(0)\dot{\Psi}(0) \right\rangle + \left\langle H(\overline{\Psi}(0), \Psi(0)) \right\rangle \\
&= C + \left\langle H(\overline{\Psi}(0), \Psi(0)) \right\rangle.
\end{aligned}
\tag{A.23}
$$

In the last line we observed that the Hamiltonian is normal ordered in accordance with the Grassmann algebra (fermionic coherent states), which differs from the fermionic ordering in the Hamiltonian of equation (A.1) which is not normal ordered. Therefore the value of E calculated via $\left\langle \frac{\delta S}{\delta \beta} \right\rangle$ using (A.23) and E calculated from (A.9) using the Hamiltonian in (A.1) differ by an indeterminate additive constant C which appears in the definition of the internal energy E, and is well known to be an essential feature of the concept of the internal energy.
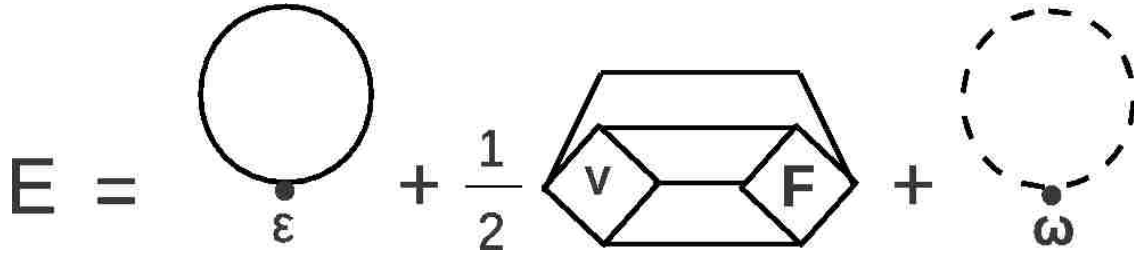

Figure A.1: Feynman Diagram representation of the internal energy of the PAM with Holstein phonons coupled to the conduction electrons. The first term corresponds to the electronic kinetic energy, where the second term represents the two particle interaction in the impurity and conduction band, and the last term corresponds to the kinetic energy of the non-interacting phonon located at the impurity site.

A.3   High-Frequency Conditioning of $\Sigma(i\omega_n)$

Here we derive the high-frequency behavior of the self-energy $\Sigma(i\omega_n)$. This is most easily done by calculating the high-frequency behavior of the Hartree and Hartree-Fock terms in

perturbation theory which are found to be

$$
\begin{aligned}
\Sigma_{\mathbf{0},0,\alpha}(i\omega_n) &= \sum_{j,\sigma} \underline{\alpha}_j \int_0^\beta \mathrm{d}\tau V_{\sigma,\alpha}(\mathbf{0},0,j,\tau) \mathrm{Tr}(\underline{\alpha}_j G_{\mathbf{0},0,\sigma}(-\eta)) \\
&\quad - \frac{1}{\beta} \sum_{j,i\omega_m} \underline{V}_j(i\omega_m) \underline{\alpha}_j G_{\mathbf{0},0,\sigma}(i\omega_n - i\omega_m) \underline{\alpha}_j.
\end{aligned} \tag{A.24}
$$

In the limit that the Matsubara frequencies become large, $n \to \infty$ the Green's function scales as $\underline{I}\frac{1}{i\omega_n}$ then the Fock term simplifies to

$$
\begin{aligned}
\Sigma_{\mathbf{0},0,\alpha}(i\omega_n) &= \sum_{j,\sigma} \underline{\alpha}_j \int_0^\beta \mathrm{d}\tau V_{\sigma,\alpha}(\mathbf{0},0,j,\tau) \mathrm{Tr}(\underline{\alpha}_j G_{\mathbf{0},0,\sigma}(-\eta)) \\
&\quad - \frac{1}{\beta} \sum_{j,i\omega_m} \underline{V}_j(i\omega_m) \underline{\alpha}_j \underline{I} \frac{1}{i\omega_n} \underline{\alpha}_j \\
&= \sum_{j,\sigma} \underline{\alpha}_j \int_0^\beta \mathrm{d}\tau V_{\sigma,\alpha}(\mathbf{0},0,j,\tau) \mathrm{Tr}(\underline{\alpha}_j G_{\mathbf{0},0,\sigma}(-\eta)) \\
&\quad - \sum_{j} \underline{V}(\mathbf{0},0,j,0) \underline{\alpha}_j \underline{I} \frac{1}{i\omega_n} \underline{\alpha}_j.
\end{aligned} \tag{A.25}
$$

The Fock term contains the effective potential $\underline{V}_j(\mathbf{0},0,j,0)$ (Fig. A.2) which has the following form for the Hubbard and electron-phonon interactions

$$
\begin{aligned}
\underline{V}(\mathbf{0},0,j=1,0) &= \sum_{\mathbf{k},i,\sigma,\sigma'} \int_0^\beta \int_0^\beta \mathrm{d}\tau \mathrm{d}\tau' V_{\alpha,\sigma}(\mathbf{k},i,j=1,0-\tau) \\
&\times \Big\{ - \langle (\underline{\Psi}^\dagger_{\mathbf{k},i,\sigma}(\tau)\underline{\alpha}_1\underline{\Psi}_{\mathbf{k},i,\sigma}(\tau))(\underline{\Psi}^\dagger_{\mathbf{k},i,\sigma'}(\tau')\underline{\alpha}_1\underline{\Psi}_{\mathbf{k},i,\sigma'}(\tau')) \rangle \\
&\quad + \langle (\underline{\Psi}^\dagger_{\mathbf{k},i,\sigma}(\tau)\underline{\alpha}_1\underline{\Psi}_{\mathbf{k},i,\sigma}(\tau)) \rangle \langle (\underline{\Psi}^\dagger_{\mathbf{k},i,\sigma'}(\tau')\underline{\alpha}_1\underline{\Psi}_{\mathbf{k},i,\sigma'}(\tau')) \rangle \Big\} V_{\sigma',\alpha}(\mathbf{k},i,j=1,\tau'-0) \\
&= -U(\langle n^f_{-\alpha} n^f_{-\alpha} \rangle - \langle n^f_{-\alpha} \rangle \langle n^f_{-\alpha} \rangle)U \\
&= -U^2 \langle n^f_{-\alpha} \rangle (1 - \langle n^f_{-\alpha} \rangle) \\
&= \chi_U.
\end{aligned} \tag{A.26}
$$

The effective potential for the electron phonon interaction is

$$
\begin{aligned}
\underline{V}(\mathbf{0},0,j=2,0) &= \sum_{\mathbf{k},i,\sigma,\sigma'} \int_0^\beta \int_0^\beta \mathrm{d}\tau \mathrm{d}\tau' V_{\alpha,\sigma}(\mathbf{k},i,j=2,0-\tau) \\
&\times \Big\{ - \langle (\underline{\Psi}^\dagger_{\mathbf{k},i,\sigma}(\tau)\underline{\alpha}_2\underline{\Psi}_{\mathbf{k},i,\sigma}(\tau))(\underline{\Psi}^\dagger_{\mathbf{k},i,\sigma'}(\tau')\underline{\alpha}_2\underline{\Psi}_{\mathbf{k},i,\sigma'}(\tau')) \rangle \\
&\quad + \langle (\underline{\Psi}^\dagger_{\mathbf{k},i,\sigma}(\tau)\underline{\alpha}_2\underline{\Psi}_{\mathbf{k},i,\sigma}(\tau)) \rangle \langle (\underline{\Psi}^\dagger_{\mathbf{k},i,\sigma'}(\tau')\underline{\alpha}_2\underline{\Psi}_{\mathbf{k},i,\sigma'}(\tau')) \rangle \Big\} V_{\sigma',\alpha}(\mathbf{k},i,j=2,\tau'-0)
\end{aligned}
$$

$$- \quad V_{\alpha,\sigma}(\mathbf{k}, i, j = 2, 0)$$

$$= \quad -\int_0^\beta \int_0^\beta d\tau d\tau' \frac{g^2}{2m\omega_0} D_0(0 - \tau)(\langle n_c(\tau) n_c(\tau') \rangle$$

$$- \quad \langle n_c(\tau) \rangle \langle n_c(\tau') \rangle) \frac{g^2}{2m\omega_0} D_0(\tau' - 0)$$

$$- \quad \frac{g^2}{2m\omega_0} D_0(\tau = 0)$$

$$= \quad \chi_D. \tag{A.27}$$

The high-frequency behavior of the self-energy $\Sigma(i\omega_n)$ as $n \to \infty$ to order $\frac{c}{i\omega_n}$ has the following matrix structure

$$\Sigma_{\mathbf{0},0,\alpha}(i\omega_n) \quad = \quad \left\{ \begin{array}{cc} -\frac{g^2}{k}(n_c - 1) + \frac{\chi_D}{i\omega_n} & 0 \\ 0 & U(n_{-\alpha} - \frac{1}{2}) + \frac{\chi_U}{i\omega_n} \end{array} \right\} \tag{A.28}$$

in which the constants added to the Hartree terms reflect the case of a particle-hole symmetric Hamiltonian. If the Hamiltonian is not written in particle-hole symmetric form then the constant terms added to the Hartree term are absent.
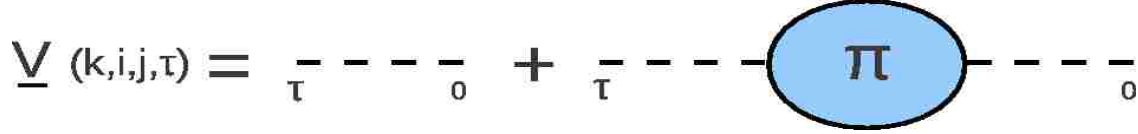

Figure A.2: Feynman Diagram representing the effective potential $\underline{V}(\mathbf{k}, i, j, \tau)$ used to calculate the numerator of $\mathrm{Im}\Sigma_{\mathbf{0},0,\alpha}(i\omega_n)$.

References

[1] J. G. Bednorz and K. A. Müller, Z. Phys. B **64**, (1986).

[2] M. K. Wu, *et al.*, Phys. Rev Lett. **58**, 908 (1987).

[3] L. Gao, *et al.*, Phys. Rev. B **50**, 4260 (1994).

[4] C. Varma, *et al.*, Science, **468**, 184 (2010).

[5] P.W. Anderson, Science, **235**, 1196 (1994).

[6] J. Kondo, Prog. Theo. Phys. **32**, 37 (1964).

[7] KY Wang, *et al.*, *Arxiv preprint cond-mat/0411475* (2004).

[8] P. Henelius and R.S. Fishman, Phys. Rev. B **78**, 214405 (2008).

[9] E. Coronado, J.R. Galán-Mascarós, and C. Martí-Fastaldo *J. Mater. Chem.* **16**, 2685 (2006).

[10] P. Misra *Heavy-Fermion Systems*, Elsevier Science (2008).

[11] A.C. Hewson *The Kondo Problem to Heavy Fermions*, Cambridge University Press (1997).

[12] H. Suhl, *et al.*, Phys. Rev. **138**, A515 (1965).

[13] A.A. Abrikosov, Phys. **2**, 5 (1965).

[14] M.A. Ruderman and C. Kittel, Phys. Rev. **96**, 1 (1954).

[15] T. Kasuya , Prog. Theo. Phys. **16**, 45 (1956).

[16] K. Yosida, Phys. Rev. **106**, 893 (1957).

[17] S. Doniach, Physica B+ C **91**, 231 (1977).

[18] J. W. Allen and R.M. Martin, Phys. Rev. Lett. **49**, 1106 (1982).

[19] M.J. Lipp, *et al.*, Phys. Rev. Lett. **101**, 165703 (2008).

[20] A. Georges, *et al.*, Rev. Mod. Phys. **68**, 13 (1996).

[21] S. M. A. Rombouts, *et al.*, Phys. Rev. Lett. **82**, 4155 (1999).

[22] A.N. Rubtsov, *et al.*, Phys. Rev. B **72**, 035122 (2005).

[23] R. M. Bozorth, H. J. Williams, and D. E. Walsh, Phys. Rev. **103**, 572 (1956).

[24] A. Nakajima and K. Kaya: J. Phys. Chem. A **104**, 176 (2000).

[25] J. M. Manriquez, *et al.*, Science **252**, 1415 (1991).

[26] K. I. Pokhodnya, A. J. Epstein, and J. S. Miller: Adv. Mater. **12**, 420 (2000).

[27] J. S. Miller: Polyhedron **28**m 1956 (2009).

[28] O.Sato, *et al.*, Science **272**, 704 (1996).

[29] O.Sato, *et al.*, J. Electrochem. Soc. **144**, L11 (1997).

[30] H. Tamaki, *et al.*, J. Am. Chem. Soc., **114**, 6974 (1992).

[31] C. Kittel, *Introduction to Solid State Physics*, (Wiley,i 1995).

[32] N. W. Ashcroft and N. D. Mermin, *Solid State Physics*, (Brooks Cole, 1976).

[33] R. S. Fishman, S. Okamoto, and F. A. Reboredo, Polyhedron **28**, 1740 (2009).

[34] T. Holstein and H. Primakoff, Phys. Rev. **58**, 1098 (1940).

[35] H. Tamaki, *et al.*, J. Am. Chem. Soc. **114**, 6974 (1992).

[36] See the review R. Clément, S. Decurtins, M. Gruselle, and C. Train, Mon. für Chem. **134**, 117 (2003) and references therein.

[37] C. Mathonière, *et al.*, J. Chem. Soc., Chem. Commun. 1551 (1994).

[38] C. Mathonière, *et al.*, Inorg. Chem. **35**, 1201 (1996).

[39] C.J. Nuttall and P. Day, Chem. Mater. **10**, 3050 (1998).

[40] E. Coronado, *et al.*, Adv. Mat. **11**, 558 (1999).

[41] G. Tang, *et al.*, Physica B **392**, 337 (2007).

[42] R.S. Fishman and F.A. Reboredo Phys. Rev. Let. **99**, 217203 (2007).

[43] K.S. Min, A.L. Rhinegold, and J.S. Miller Inorg. Chem. **44**, 8433, (2005).

[44] J. Larionova, *et al.*, Inorg. Chem. **37**, 679 (1998).

[45] E. Coronado, *et al.*, Nature **408**, 447 (2000).

[46] M. Clemente-León, *et al.*, Chem. Commun. 1727 (1997).

[47] In most 3d and 4d bimetallic oxalates, the orbital-correlation energy is weak, so the total orbital angular momentum L_t of the electrons is not a good quantum number and Hund's second rule is not obeyed. Even if L_t is a good quantum number, however, the formalism developed in this paper can still be employed because the C_3-symmetric crystal-field potential will split the $L_t = 2$ ($3d^n$, $n = 1$, 4, 6, or 9) or $L_t = 3$ ($n = 2$, 3, 7, or 8) multiplets into a sequence of singlets and doublets.

[48] B. Bleaney and K.W.H. Stevens, Rep. Prog. Phys. **16**, 108 (1953).

[49] O. Kahn, *Molecular Magnetism* (VCH, New York, 1994).

[50] H. Tamaki,*et al.*, J. Am. Chem. Soc. **114**, 6974 (1992).

[51] Yu P. Bénard, *et al.*, J. Am. Chem. Soc. **122**, 9444 (2000).

[52] E. Coronado, *et al.*, Nature **408**, 447 (2000).

[53] C. Mathonière, *et al.*, Inorg. Chem. **35**, 1201 (1996).

[54] J. Larionova, *et al.*, Inorg. Chem. **37**, 679 (1998).

[55] K.S. Min, A.L. Rhinegold, and J.S. Miller Inorg. Chem. **44** 8433 (2006).

[56] E. Coronado, J.R. Galán-Mascarós and M. Martí-Fastaldo J. Mater. Chem. **11**, 2685 (2006).

[57] I.D. Watts, *et al.*, J. Phys. Chem. Sol. **66**, 243 (2005).

[58] R.S. Fishman and F. Reboredo, Phys. Rev. Lett. **99**, 217203 (2007).

[59] R.S. Fishman and F. Reboredo, Phys. Rev. B **77**, 144421 (2008).

[60] P. Reis, *et al.*, Phys. Rev. B **77**, 174433 (2008).

[61] P. Henelius and R.S. Fishman (*unpublished*)

[62] I.-K. Jeong, *et al.*, Phys. Rev. Lett. **92**, 105702 (2004).

[63] D.G. Koskimaki and K.A. Gschneidner, Jr., in *Handbook on the Physics and Chemistry of Rare Earths*, (North-Holland, Amsterdam, 1978).

[64] B. Johansson, Philos. Mag. **30**, 469 (1974).

[65] E. Wuilloud, H.R. Moser, W.-D. Schneider, and Y. Baer, Phys. Rev. B **28**, 7354 (1983).

[66] J.W. Allen and R.M. Martin, Phys. Rev. Lett. **49**, 1106,(1982).

[67] P. Fulde, *Electron Correlations in Molecules and Solids* (Springer, Germany, Heidelberg, 1995).

[68] A.-M. Daré, L. Raymond, and G. Albinet, Phys. Rev. B. **76**, 064402 (2007).

[69] M. Krisch *et al.*, *Phonons of the anomalous element cerium* PNAS (2011).

[70] W. Metzner and D. Vollhart, Phy. Rev. Lett. **62**, 324 (1989).

[71] B. B. Beard and U.-J. Wiese. Phys. Rev. Lett. **77**, 5130 (1996).

[72] A. Georges, G. Kotliar, W. Krauth, and M.J. Rozen, Rev. Mod. Phys. **68,** 13, (1996).

[73] A.N. Rubtsov, V.V. Savkin, and A.I. Lichtenstein, Phys. Rev. B **72,** 035122, (2005).

[74] E. Wuilloud, *et al.*, Phys. Rev. B **28**, 7354 (1983).

[75] F. U. Hillebrecht, *et al.*, Phys. Rev. B **30**, 1777 (1984).

[76] L. Z. Liu, *et al.*, Phys. Rev. B **45**, 8934 (1992).

[77] J. Kondo, Prog. Theor. Phys. **32**, 37 (1964).

[78] P.W. Anderson, Phys. Rev. **124**, 41 (1961).

[79] J. R. Schrieffer and P. A. Wolff, Phys. Rev. **149**, 491 (1966).

[80] A.M. Clogston, *et al.*, Phys. Rev. **125**, 541, (1962).

[81] S.Doniach, Physica B **91**, 231 (1977).

[82] M.A. Ruderman and C. Kittel, Phys. Rev. **96**, 99 (1954).

[83] T. Kasuya, Prog. Theor. Phys. **16**, 45 (1956).

[84] K. Yosida, Phys. Rev. **106**, 893 (1957).

[85] T. M. Rice, K. Ueda, Phys. Rev. Lett. **55**, 995 (1985).

[86] M. Jarrell, Phys. Rev. B **51**, 7429 (1995).

[87] T. Holstein, Ann. Phys. **8**, 325 (1959).

[88] T. Holstein, Ann. Phys. **8**, 343 (1959).

[89] R. Peierls, *Quantum Theory of Solids* (Oxford: Pergamon,1955).

[90] J. E. Hirsch and E. Fradkin, Phys. Rev. B **27**, 4302 (1983).

[91] L. D. Landau, Phys. Z. Sowjetunion **3**, 644 (1933).

[92] F.F. Assaad and T.C. Lang, Phys. Rev. B **76,** 035116 (2007).

[93] R. Nourafkan and Nasser Nafari Phys. Rev. B **79,** 075122 (2009).

[94] P. C. Martin and J. Schwinger Phys. Rev. **115,** (1959).

[95] A. Georges, *et al.*, Rev. Mod. Phys. **68,** 13, (1996).

[96] A.N. Rubtsov, V.V. Savkin, and A.I. Lichtenstein, Phys. Rev. B **72,** 035122, (2005).

[97] F.F. Assaad and T.C. Lang, Phys. Rev. B **76,** 035116 (2007).

[98] R. Nourafkan and Nasser Nafari Phys. Rev. B **79,** 075122 (2009).

[99] P. C. Martin and J. Schwinger Phys. Rev. **115,** (1959).

[100] L. Landau, JETP, **3**, 920 (1957).

[101] L. Landau, JETP, **8**, 70 (1959).

[102] A. A. Abrikosov, L. P. Gorkov, and I. E. Dzyaloshinski, . *Methods of Quantum Field Theory in Statistical Mechanics* (Dover Publications, Inc., New York, 1963).

[103] V. Galitskii and A. Migdal, JETP **7**, 96 (1958).

[104] K. Held, A. K. McMahan, and R. T. Scalettar, Phys. Rev. Lett. **87**, 276404 (2001).

[105] A. K. McMahan, K. Held, R. T. Scalettar, Phys. Rev. B, **67**, 075108 (2003).

[106] L. de' Medici, Phys. Rev. Lett. **95**, 064402 (2005).

[107] B. Amadon, *et al.*, Phys. Rev Lett. **96**, 066402 (2006).

[108] M. Lüders, *et al.*, Phys. Rev. B **71**, 205109 (2005).

[109] W. H. Zachariasen, Phys. Rev. **76**, 301 (1949).

[110] A. F. Schuch, J. H. Sturdivant, J. Chem. Phys. **18**, 145 (1950).

[111] L. Z. Liu, *et al.*, Phys. Rev. B **45**, 8934 (1992).

[112] M. Lavagna, C. Lacroix, and M. Cyrot, Phys. Lett. **90A**, 210 (1982).

[113] M. Lavagna, C. Lacroix, and M. Cyrot, J. Phys. F **13**, 1008 (1983).

Vita

Peter Leo Reis was born on January 15, 1979, in Storm Lake Iowa. He finished his undergraduate study in Physics in 2005 at the University of North Dakota. He started his graduate study in physics toward a Ph.D. at the University of North Dakota in August 2005 to September 2008, at which time he transferred to Louisiana State University to continue his Ph.D. tranining in physics. He is currently a candidate for the degree of Doctor of Philosophy in physics at Louisiana State University, which he will be awarded in the Fall semester of 2012.